

Variational studies of dressed quasiparticles' properties and their interactions with external potentials

by

S. Hadi Ebrahimnejad Rahbari

B.Sc., Tabriz University, 2004

M.Sc., Sharif University of Technology, 2007

M.Sc., The University of British Columbia, 2009

A THESIS SUBMITTED IN PARTIAL FULFILLMENT OF
THE REQUIREMENTS FOR THE DEGREE OF
DOCTOR OF PHILOSOPHY

in

The Faculty of Graduate and Postdoctoral Studies

(Physics)

THE UNIVERSITY OF BRITISH COLUMBIA

(Vancouver)

December 2014

© S. Hadi Ebrahimnejad Rahbari 2014

Abstract

In this thesis, we investigated the spectral properties of polaronic quasiparticles resulting from the coupling of a charge carrier to the bosonic excitations of ordered environments. Holstein polarons, describing an electron locally coupled to dispersionless phonons, and spin polarons in hole-doped antiferromagnets are considered. The Green's function of the Holstein polaron in a lattice with various kinds of impurities is calculated using the momentum average approximation. The main finding is that the scenario where the mere effect of the coupling to phonons is to enhance the electron's effective mass is incomplete as the phonons are found to also renormalize the impurity potential the polaron interacts with. This formalism is applied first to the case of a single impurity and the range of parameters where the polaron's ground state is localized is identified. The lifetime of the polaron due to scattering from weak but extended disorder is then studied and it is shown that the renormalization of the disorder potential leads to deviation of the strong coupling results from Fermi's golden rule's predictions.

Motivated by the hole-doped cuprate superconductors, the motion of a hole in a two-dimensional Ising antiferromagnet and its binding to an attractive impurity is studied next, based on a variational scheme that allows for configurations with a certain maximum number of spin flips. The role of the magnetic sublattices in determining the symmetry of the resulting bound states is discussed. Next, a more realistic model describing a hole in a CuO_2 layer which retains the O explicitly, is considered. By neglecting the fluctuations of the Cu spins and using a variational principle similar to that of the previous chapter, a semi-analytic solution for the Green's function of the hole in an infinite 2D lattice is constructed. The resulting quasiparticle dispersion shows the proper ground state and other features observed in experiments. The lack of importance of the background spin fluctuations is justified based on the hole's ability to move on the O sublattice without disturbing the Cu spins. Finally, the model is generalized to gauge the importance of other relevant O orbitals.

Preface

- A version of the work discussed in chapter 2 is published as “*H. Ebrahimnejad and M. Berciu, Physical Review B* **85**, 165117 (2012)”. It is a development of a previous work by Prof. M. Berciu which was published in Ref. [1].
- The work discussed in chapter 3 is published as “*H. Ebrahimnejad and M. Berciu, Physical Review B* **86**, 205109 (2012)”.
- The work discussed in chapter 4 is published as “*H. Ebrahimnejad and M. Berciu, Physical Review B* **88**, 104410 (2013)”. The variational method used here was suggested before by M. Berciu in Ref. [2].
- The work discussed in chapter 5 is published as “*H. Ebrahimnejad, G. A. Sawatzky and M. Berciu, Nature Physics* **10**, 951-955 (2014)”. A more detailed manuscript is under review for publication in another journal. The model we used here was introduced in Ref. [3].

I carried out analytical and numerical work for all four projects and wrote the first draft of the manuscript for the first three, which were then revised by M. Berciu before submission. The preparation of the draft for the paper published in Nature Physics as well as calculations for the three-magnon case are done by M. Berciu.

Table of Contents

Abstract	ii
Preface	iii
Table of Contents	iv
List of Figures	vii
Acknowledgements	xv
1 Introduction	1
1.1 Hamiltonian for lattice polarons	3
1.1.1 Polarons in systems with other forms of electron-boson coupling	6
1.2 Studying spectral properties using Green's function formalism	7
1.3 Green's function of the Holstein model and its variational calculation	8
1.4 Overview of thesis and further reading	9
2 Trapping of three-dimensional Holstein polarons by various impurities	12
2.1 Introduction	12
2.2 Momentum average approximation for inhomogeneous sys- tems	13
2.3 Polaron near a single impurity	21
2.3.1 Impurity changing the on-site energy	22
2.3.2 Impurity changing the electron-phonon coupling	29
2.3.3 Isotope impurity	31
2.4 Summary and conclusions	35

Table of Contents

3	A perturbational study of the lifetime of a Holstein polaron in the presence of weak disorder	38
3.1	Introduction	38
3.2	The model and its solution	39
3.3	Results	42
3.3.1	Weak electron-phonon coupling	45
3.3.2	Strong electron-phonon coupling	47
3.4	Summary and conclusions	52
4	Binding carriers to a non-magnetic impurity in a two-dimensional square Ising anti-ferromagnet	55
4.1	Introduction	55
4.2	The Model	57
4.3	Propagation of the hole in the clean system	59
4.4	The effect of the impurity	66
4.4.1	Quasiparticle and impurity on the same sublattice	67
4.4.2	Quasiparticle and impurity on different sublattices	71
4.5	Summary and conclusions	76
5	Accurate variational solution for a hole doped in a CuO₂ layer	79
5.1	Introduction	79
5.2	Three-band model for a cuprate layer and its t - J analogue	80
5.2.1	Doping the CuO ₂ layer with a hole	84
5.3	Green's functions	87
5.3.1	One-magnon approximation	88
5.3.2	Two-magnon approximation	93
5.4	Results	94
5.4.1	Dispersion relations	94
5.4.2	Effect of various terms in the Hamiltonian	97
5.5	Quasiparticle weight	99
5.5.1	Comparison with ARPES	99
5.6	Spin polaron vs the Zhang-Rice singlet	102
5.7	From three-band to five-band model: effect of other in-plane $2p$ orbitals	105
5.8	Conclusion	109
6	Summary and development	110
6.1	Summary of this work	110
6.2	Outlook and further developments	112

Table of Contents

Bibliography	114
 Appendices	
A MA⁰ solution for the clean system	121
B IMA¹	123
C MA⁰ solution for $F_{\mathbf{k},s_i}^{(n)}(\omega)$ and $W^{nm}(\omega)$	126
D Disorder self-energy in Average T-matrix approximation	128
E The equations of motion for $G_{0,\mathbf{R}}(\omega)$	129
F Derivation of ARPES intensity	131
G Solving for $G_{\alpha,\beta}(\mathbf{k},\omega)$ in the five-band model	135

List of Figures

2.1	Diagrammatic expansion for (a) the disorder GF $G_{ij}^d(\omega)$ (bold red line); (b) the polaron GF in a clean system $G_{ij}^0(\tilde{\omega})$ (double thin line), and (c) the “instantaneous” approximation for the polaron GF in a disordered system, $G_{ij}^d(\tilde{\omega})$ (double bold red line). The thin black lines depict free electron propagators, the wiggly lines correspond to phonons, and scattering on the disorder potential is depicted the dashed lines ending with circles. See text for more details.	16
2.2	(color online) (a) Diagrammatic expansion for the full MA solution $G_{ij}(\omega)$ (thick dashed blue line) in terms of the clean polaron Green’s function (double thin line) and scattering on the renormalized disorder potential $\epsilon_l^*(\omega)$, depicted by dashed lines ended with squares. (b) Diagrammatic expansion of $\epsilon_l^*(\omega)$. For more details, see text.	19
2.3	LDOS at the impurity site $\rho(0, \omega)$ in units of $1/t$, vs. the energy ω/t , for (a) MA ⁰ with $l_c = 0$ for $U = 1.8, 1.9, 1.95$ and 2.0 . The dashed line shows the DOS for the clean system, times 100; (b) Bound polaron peak in MA ⁰ at $U/t = 2$, and cutoffs in the renormalized potential $l_c = 0, 1, 2$. Panels (c) and (d) are the same as (a) and (b), respectively, but using MA ¹ . Panel (e) shows the DMC results from Ref. [4], for the same parameters as (a) and (b). Other parameters are $\Omega = 2t, \lambda = 0.8, \eta/t = 10^{-3}$	24
2.4	Phase diagram separating the regime where the polaron is mobile (below the line) and trapped (above the line). The effective coupling is $\lambda = g^2/(6t\Omega)$, and the threshold trapping potential U_c is shown for several values of Ω/t . The MA results (filled symbols) compare well with the DMC results of Ref. [4] (empty symbols).	25

List of Figures

2.5	(color online) Effective value of the impurity attraction U^*/U , extracted from the scaling $E_B^*/t^* = f(U^*/t^*)$, for $\lambda = 0.5, 1.5$ and $\Omega = 3t$. In order to have the best fit to the data, we plot each curve starting from slightly larger U/t than the corresponding U_c/t given in Fig. (2.4). For more details, see text.	26
2.6	(color online) Real part of the additional on-site MA^0 disorder potential $v_0(0, \omega)$ over a wide energy range, for $U = 2t, \Omega = 2t, \lambda = 0.8$ and two values of η	28
2.7	(color online) Phase diagram separating the regime where the polaron is delocalized (below the line) and trapped (above the line), as a function of the difference between the impurity and the bulk electron-phonon coupling, $g_d - g$. Symbols show MA^0 results, while the dashed lines correspond to the instantaneous approximation.	30
2.8	For large λ , in the clean system (dashed red line) the first polaron band is separated by an energy gap from the next features in the spectrum (here, the band associated with the second bound state). For $g_d < g$, an “anti-bound” impurity state is pushed inside this gap (black full line). Parameters are $\Omega = t = 1, \lambda = 1.2$ and $\eta = 10^{-3}$	32
2.9	(color online) Critical effective coupling λ^* above which an impurity state may appear for a sufficiently light isotope. Below this line, polarons cannot be bound near isotopes. Symbols shows MA^0 results. The dashed line is the analytic low-bound for λ^* discussed in the text.	33
2.10	Phase diagram separating the regime where the polaron is delocalized (below the line) and trapped (above the line), as a function of the difference between the $\Omega_d - \Omega$, on a logarithmic scale. Symbols show MA^0 results for $\Omega = 4t, 8t$. As $\Omega_d \rightarrow \infty$, these critical lines converge towards their corresponding λ^* (dashed lines), below which polaron states are always delocalized.	35
2.11	LDOS at the impurity site near an isotope with $\Omega_d = \Omega + 7t$ (full line). Two discrete states, one above and one below the bulk polaron band, are seen. For comparison, the DOS in the clean system (multiplied by 10) is shown as a dashed line. Parameters are $\Omega = 4t, \lambda = 2.5$ and $\eta = 10^{-2}$	36

List of Figures

3.1	(a) Inverse polaron lifetime $1/\tau_{\mathbf{k}}$ vs its peak energy $E_{\mathbf{k}}$, and (b) average density of states $\bar{\rho}(\omega)$, for a weak electron-phonon coupling and two values of the disorder Δ . The solid and dashed lines are the corresponding Fermi golden rule (FGR) and ATA results, respectively (see text for more details). Other parameters are $\Omega = t, \eta/t = 10^{-2}$ in (a) and $\eta/t = 5 \times 10^{-3}$ in (b).	44
3.2	Inverse lifetime of the polaron of momentum $\mathbf{k} = (\pi/8, 0, 0)$ and $\lambda = 0.5$ vs the strength of disorder, Δ/t (full squares). The inverse lifetime for a free electron with the same momentum is shown by triangles. Empty squares show $1/(t^*\tau_{\mathbf{k}})$ vs Δ/t^* for the polaron (for this λ , $t^* = 0.881t$). Other parameters are $\Omega = t, \eta/t = 10^{-2}$	46
3.3	(Color online). Top panels: $1/(t\tau_{\mathbf{k}})$ vs $E_{\mathbf{k}}/t$ for three levels of disorder: $\Delta/t = 0.05, 0.1$ and 0.15 . The symbols shows the MA result for a strong coupling $\lambda = 1.2$, while the full and dashed lines show Fermi's golden rule and the ATA predictions, respectively. Bottom panels: The average DOS $\bar{\rho}(\omega)$ for that Δ (full line) and the DOS in the clean system, $\rho_{\text{H}}(\omega)$ (dashed line) vs ω . Parameters are $\Omega = t, \eta = 10^{-3}t$	47
3.4	(Color online) The same average DOS vs ω displayed in the lower panels of Fig. 3.3, but now shown for the entire polaron band.	49
3.5	(i) FGR approximation for the disorder-averaged Green's function of a carrier (double thin line), in terms of that of the free carrier (thin line) and uncorrelated disorder (dashed line) in the absence of electron-phonon coupling; (ii) FGR approximation for the disorder-averaged GF of a polaron (double thick line), in terms of that of the clean polaron (thick line); (iii) clean polaron GF in terms of free carrier (thin lines) and phonon (curly lines) propagators; (iv) the first few terms in the MA approximation for the disorder averaged GF of a polaron.	50
3.6	(Color online) (a) Inverse lifetime vs disorder, and (b) inverse lifetime vs energy $E_{\mathbf{k}}$, as disorder is turned on, for two momenta $\mathbf{k}_1 = (2\pi/9, 0, 0)$ and $\mathbf{k}_2 = (\pi/6, 0, 0)$, for a polaron with $\lambda = 1.2, \Omega = t, \eta = 10^{-3}t$. The asterisk in panel (b) marks the clean polaron GS energy in the clean system, E_{GS} , for these parameters. See text for more details.	52

List of Figures

3.7	(color online) Same data as shown in Fig. 3.6(a) but with rescaled axes; $1/(t^*\tau_{\mathbf{k}})$ vs Δ/t^* for momentum $\mathbf{k}_2 = (2\pi/9, 0, 0)$ (empty squares) is compared with the free electron lifetime (triangles) at the same momentum, for $\lambda = 1.2$ where $t^* = 0.148t$. Other parameters are $\Omega = t$ and $\eta/t = 10^{-3}$	53
4.1	Square lattice of Néel-ordered Ising spins. Removing one of the spin-up particles creates a hole and results in a configuration with $s_z = -\frac{1}{2}$	59
4.2	Effective first- and second-nearest-neighbor hoppings of the hole (the blue circle) achieved with loops involving only up to three magnons. The latter is realized when the hole starts a second loop before removing the last magnon it created during the first loop. The magnons are shown by red circles. The properly oriented spins are not shown.	61
4.3	The choice of coordinate systems for the lattice with impurity. The impurity, shown as purple square, is at the origin of the xy axes that span the original lattice with unit vectors \mathbf{x}, \mathbf{y} . The XY axes are rotated by 45° and span the sublattice (black dots) on which the quasiparticle propagates via the elementary vectors $\mathbf{y} \pm \mathbf{x}$	63
4.4	The total density of states (top panels), effective hoppings $t_1(\omega), t_2(\omega)$ (middle panels) and on-site energy $\varepsilon(\omega)$ (bottom panels) in the clean system for two different values of t/\bar{J} . The effective parameters are relatively constant within the energy band, explaining why the DOS has the generic form expected for a bare particle with nearest-neighbor hopping on a square lattice. Here $\bar{J} = 1$, $\eta = 10^{-3}$ and $t = 3$ (left panels) and $t = 6$ (right panels), respectively.	66
4.5	(Top): the energy dispersion and the quasiparticle weight for the lowest polaron band. The ground state is at $\mathbf{k} = (0, 0)$, while $\mathbf{k} = (\frac{\pi}{2}, \frac{\pi}{2})$ is a saddle point. The top-right quadrant of the full Brillouin zone (BZ) and that of the corresponding magnetic BZ (dashed green) is shown at the inset. The band folding due to AFM order leads to symmetric dispersion along $(0, 0) - (\pi, \pi)$. The quasiparticle weight has only minor variations which can be related to the fact that the polaron bandwidth (≈ 0.3) is considerably smaller than the energy of a typical spin defect (few \bar{J}) in the magnon cloud. $t = 3\bar{J} = 3$ and $\eta = 10^{-3}$	67

List of Figures

4.6	(Top) LDOS at the impurity site for various values of U . The dashed line is the DOS in the clean system, times 4. At finite U , a single bound state splits from the continuum and its binding energy increases with U . Curves are shifted vertically to help visibility. (bottom) The effective on-site energy at the impurity site is essentially equal to U . Parameters are $t = 6$, $\bar{J} = 1$ and $\eta = 10^{-3}$	68
4.7	Relative amplitude of the wave functions corresponding to three of the bound states shown in Fig. 4.6, at various distances from the impurity site. Lines are exponential fits. States with bigger binding energies have shorter decay lengths.	70
4.8	(Top) LDOS $\rho(\mathbf{r} = \mathbf{x}; \omega)$ with curves shifted vertically to help visibility; (Bottom) $U_{\text{eff}}(\mathbf{r} = \mathbf{x}; \omega)$ at the quasiparticle's sublattice site located nearest to the impurity. Up to three bound states split from the continuum upon increasing U . The presence of the impurity at $\mathbf{r} = \mathbf{0}$ induces a finite effective on-site attraction at $\mathbf{r} = \mathbf{x}$, whose value is significantly smaller than U (Bottom). Parameters are $t = 6$, $\bar{J} = 1$, and $\eta = 10^{-3}$	71
4.9	Relative amplitude of the upper and lower bound states for $U = -2\bar{J}$, at various distances from the impurity site. Lines are exponential fits.	72
4.10	Binding energy of the s -wave bound state at $U = -\bar{J}$ vs. t/\bar{J} , when the quasiparticle and the impurity are on the same sublattice (top panel) and different sublattices (bottom panel). The smaller binding energy at strong hopping is due to the reduction in the quasiparticle's effective mass, which makes it harder to trap. When the quasiparticle and the impurity are on different sublattices, the enhancement of U_{eff} at small t dominates over the effective mass decrease, explaining the growth of the binding energy here.	74
4.11	The gap between the p_x and either of the s or d states, for a fixed U . Its enhancement as a function of t/\bar{J} reflects the rotational kinetic energy gain of the quasiparticle as it becomes lighter with increasing t	75

List of Figures

5.1	(a): Cu, shown in red, is surrounded by six O ligands in octahedral geometry. The static electric field of these ligands partially removes the degeneracy of Cu $3d$ orbitals into e_g and t_{2g} manifolds. This degenerate configuration distorts to remove the remaining degeneracies and ends up having $3d_{x^2-y^2}$ as its highest partially-occupied orbital, (b). The values of splittings for La_2CuO_4 are given. In the case of $\text{Sr}_2\text{CuO}_2\text{Cl}_2$, splitting within e_g is such strong that $3d_{3z^2-r^2}$ orbital is pushed below the entire t_{2g} manifold.	81
5.2	(a) The ground state of charge-transfer insulator (left) and its lowest excitation (right) Δ_{pd} higher in energy. \uparrow and \downarrow represent electrons and \circ stands for a hole (electron representation). (b) In a Mott insulator, however, charge excitation with the lowest energy corresponds to an electron moving from one Cu to another at an energy cost of U_{dd}	82
5.3	One set of processes giving rise to the superexchange coupling, J_{dd} , between two neighbouring Cu holes. Arrows represent the holes and empty O levels corresponds to them being doubly-occupied with electrons (hole notation). The energies of intermediate configurations are given.	83
5.4	Energy diagram of the undoped CuO_2 layer, illustrating a charge-transfer insulator. The filled bands are shaded, above them lies the Fermi energy in the gap. Since $\Delta_{pd} < U_{dd}$, removing electrons created holes on O's rather than on Cu's and this moves the Fermi energy into the O $2p$ -band.	84
5.5	(a): The CuO_2 layer with the spin-up hole occupying one of the O $2p$ orbitals. nn (δ) and next nn hops (ϵ) between O's that are considered in our model are shown. For the hole, nn hopping is negative along $y = x$ direction where $2p$ orbitals have their lobes with similar phases pointing towards each other and positive along $y = -x$. (b): Cu and O ions that make the unit cell are shown in green. (c): Processes that give rise to nn (c1) and next nn (c2) spin-swap. (d): The full Brillouin zone of the CuO_2 lattice (the outer square) which encloses the magnetic Brillouin zone (shaded). We study the quasiparticles with momenta lying along the dashed red line, starting from $(0, \pi)$ and ending at $(\pi, 0)$	86

List of Figures

5.6	Numbering various one-magnon Green's function V_i^M at $M = 1, 3$: the one with the hole lying to the far left is $i = 0$ and the index i increases in the counterclockwise direction. The current configuration corresponds to V_1^2	89
5.7	Numbering various two-magnon GFs at $M = 1, 3$. The configuration shown corresponds to W_3^2	92
5.8	The spectral weight at $n_m = 2$ approximation, $A_{p_{x_1}}(\mathbf{k}, \omega)$ in color scale as a function of momentum and energy (in units of $J_{dd} \approx 0.1 - 0.15$ eV), showing several coherent bands. For the rest of this chapter, only the lowest energy band will be studied.	96
5.9	(a): Energy dispersion (in units of $J_{dd} \approx 0.1 - 0.15$ eV) of the hole without allowing for the creation of magnons, $n_m = 0$. The ground state is still at $\mathbf{k} = (\frac{\pi}{2}, \frac{\pi}{2})$. (b): Comparison between one- and two-magnon approximation results for the hole's energy dispersion along various cuts in the full BZ. The dots are relevant exact-diagonalization calculations for a finite size sample of the same model, shifted in energy in order to ease the comparison.	97
5.10	The lowest quasiparticle dispersion ($n_m = 2$ and in units of $J_{dd} \approx 0.1 - 0.15$ eV) when various terms in the Hamiltonian (5.3) are on and off. J_{pd} has almost no effect on the dispersion (a), whereas without t_s (c) the model fails to properly predict the expected ground state $\mathbf{k} = (\frac{\pi}{2}, \frac{\pi}{2})$. For comparable values of t_s and t_{pp} , the correct shape of energy dispersion re-appears (d).	98
5.11	top: quasiparticle weights extracted from the sublattice GF $A_{p_{x_1}}(\mathbf{k}, \omega)$ in one- and two-magnon approximation. The corresponding energy dispersion (for the two-magnon approximation, in units of $J_{dd} \approx 0.1 - 0.15$ eV) is presented in the lower panel.	100
5.12	The quasiparticle weights in $n_m = 2$ approximation extracted from spectral weights that correspond to projections onto orbitals with different polarizations, $2p_x$ and $2p_y$	101
5.13	Comparison between one- and two-magnon approximation results for ARPES quasiparticle weight. This shows disagreement with experiments for momenta along $(0, 0) - (\pi, \pi)$. See text for further discussions.	102

List of Figures

5.14	Inside the dashed circle are the copper and oxygens involved in Zhang-Rice singlet. Labelling of one-magnon GFs are such that once the copper and hole's spin are flipped, the current configuration becomes V_1^2 . The sign of each singlet contribution to ZRS is given.	103
5.15	top: overlap between the states in the lowest polaron band $ \phi\rangle$ whose energy dispersion (in units of $J_{dd} \approx 0.1 - 0.15$ eV) is shown at the lower panel, and the corresponding Zhang-Rice singlet states.	104
5.16	The CuO_2 layer with two in-plane $2p$ orbitals per O. The nn hopping between new (blue) and original (green) orbitals, \tilde{t}_{pp} , and the next nn hopping between the new orbitals, \tilde{t}'_{pp} , are shown.	106
5.17	Energy dispersion (in units of $J_{dd} \approx 0.1 - 0.15$ eV) and ARPES quasiparticle weight of the five-band model that includes two $2p$ orbitals per O. Whereas the energy dispersions are qualitatively similar to those given by the three-band model, the quasiparticle weight is now less sensitive to the structure of magnon cloud.	107
5.18	Constant-energy map of ARPES spectral weight for the five-band model. It clearly shows the asymmetry of the quasiparticle weight between the inside and outside of the magnetic BZ, which is a robust feature for the generic values of parameters.	108
F.1	The effect of finite K/λ (lowest order correction) on the ARPES quasiparticle weight of the five-band model. The difference between the quasiparticle dispersions is invisible on the same energy scale.	133

Acknowledgements

I would like to use this opportunity to thank my adviser, Prof. Mona Berciu, for all her efforts in guiding me through my PhD years, a task that she did with patience, enthusiasm and good manners. It was through working with her that I learned how asking the right questions is an important trait for any serious researcher, a quality she is also quite good at it. She gave me the right problems which eventually resulted in successful projects that made parts of my thesis. I am grateful for her always making herself available by all means, making it possible for me to better focus my attention and efforts towards accomplishing my research goals in a timely manner.

I would also like to acknowledge the members of my PhD committee for attending scheduled meetings, reading the thesis and their suggestions for its improvement. Special thanks goes to Prof. George Sawatzky for his collaboration and insightful remarks which turned the project discussed in chapter five into a more impactful piece of work.

Last but not least, I thank my parents and my brother Habib, who was my inspiration to pursue physics, for their support in all stages of my life. Finally, I gratefully thank my wife, Parisa, for all her support, caring and love which has been a real source of encouragement to me and will certainly be so for years to come.

Chapter 1

Introduction

Understanding various macroscopic physical properties exhibited by solid state materials generally requires studying their microscopic structure, the dynamics of their constituent electrons and their interaction with the rest of the solid. The simplest description of electrons inside a solid (apart from the particle in a box model) is given by the band theory in which mobile electrons are thought of as interacting with a perfectly periodic lattice of immobile ions¹. In this approximation, the $\varepsilon(\mathbf{k}) \sim k^2$ energy dispersion of an electron in free space is replaced by a series of energy bands, $\varepsilon_n(\mathbf{k})$, that show the periodicity of the corresponding reciprocal lattice [5]. If one can ignore electron-electron correlations, the many-electron states are then constructed by populating these single-particle energy bands according to Fermi statistics which forbids multiple occupancy of any quantum state. The band theory successfully explains why some solids are metallic whereas others are electrical insulators: insulators are those that have their highest occupied energy band completely filled, as electrons in completely filled bands do not carry a net electrical current and exciting them to empty bands costs a finite amount energy. Materials with partially filled valence bands are metallic, since a net current results when electrons are excited into empty states of the same band with an infinitesimal energy cost.

With many electrons to fill the energy bands, one has to account for the Coulomb repulsion between them beyond mean-field approximations. At low temperatures and for weak electron-electron interactions, it results in scattering of electrons into low-lying unoccupied states near the Fermi level. The Fermi liquid theory predicts a one-to-one correspondence between the \mathbf{k} -states of the interacting system and those of the non-interacting system [6]. This analogy introduces the notion of Landau quasiparticles as the elementary excitations in systems of interacting fermions. These quasiparticles have a different effective mass $m^* \neq m_{\text{el}}$ and, due to phase space restrictions, they are much more weakly interacting than the original electrons the closer they get to the Fermi surface where they become long-lived and accord-

¹The potential includes a mean-field (Hartree-Fock) contribution from the other electrons in the solid.

ingly well-defined. This gives a single particle description of the interacting system where the quasiparticles replace the bare electrons.

In the strongly correlated systems, however, the motion of individual electrons depends on the state of the other electrons. This is generally the case for systems where the interaction between electrons is strong compared to their kinetic energy that enable electrons to avoid each other. The suppression of kinetic energy in such systems gives rise to a variety of fascinating ordered states such as those observed in magnetic materials, fractional quantum Hall and other interacting low-dimensional systems and various unconventional superconductors. The quasiparticles in these systems have either exotic properties or their mere existence is still debated.

Coming back to the single electron limit, the assumption that the ions are at rest violates the Heisenberg uncertainty principle by neglecting their zero-point motion. Furthermore, even though ions are much heavier than electrons, the attractive interaction among the two causes the lattice to distort. The excess density of positive charges in the distorted part of the lattice acts like a local potential well for the electron. It was even proposed that in a strongly distorted lattice an electron traps itself into the potential well it creates [7]. In a clean lattice, however, translational invariance prevents the electron from being localized at any particular site. Therefore, it remains mobile but its effective mass becomes larger due to the lattice distortions it drags behind.

In quantum mechanical terms, where the lattice distortions are described as phonons, a many-body picture emerges where the electron plus the accompanying lattice distortion is viewed as a quasiparticle comprised of the electron surrounded by a fluctuating cloud of phonons. This is known as a lattice polaron. They are a useful way of thinking about charge carriers (electrons or holes) in ionic crystals and organic semiconductors [8].

In many-electron systems, the lattice distortion created by an electron can attract another electron and result in an effective attraction between the two electrons which, in suitable conditions, can bind them together into a bipolaron state. If the electrons are much faster than the lattice ions, however, the distortion created by the first electron persists even after it moves away. When the second electron arrives in this region, the first one is already gone. Therefore, there will not be a strong repulsive force between them and the effective attraction prevails even if it is rather weak. This may result in bound states in the momentum space, well-known for their role in establishing conventional (BCS) superconductivity [9].

1.1 Hamiltonian for lattice polarons

The generic Hamiltonian for a system of an electron in a lattice is

$$\mathcal{H} = -\frac{\hbar^2}{2m}\nabla_{\mathbf{r}}^2 + \sum_j V_{\text{el-a}}(\mathbf{r} - \mathbf{R}_j) + \mathcal{H}_{\text{lat}}, \quad (1.1)$$

where \mathbf{r} is the position of the electron, \mathbf{R}_j are those of the lattice sites and \mathcal{H}_{lat} is the lattice Hamiltonian which, for harmonic lattice deformations, can be cast into the usual phonon Hamiltonian (see below). $V_{\text{el-a}}(\mathbf{r} - \mathbf{R}_j)$ is the interaction between the electron (with the bare mass m) and the lattice ion at \mathbf{R}_j . For small lattice deformations, $\mathbf{u}_j = \mathbf{R}_j - \mathbf{R}_j^0 \ll a$, where a is the lattice constant and \mathbf{R}_j^0 are the equilibrium position of lattice sites, the second term can be approximated to its first-order expansion in \mathbf{u}_j

$$\mathcal{H} = \underbrace{-\frac{\hbar^2}{2m}\nabla_{\mathbf{r}}^2 + \sum_j V_{\text{el-a}}(\mathbf{r} - \mathbf{R}_j^0)}_{\mathcal{H}_b} - \sum_j \mathbf{u}_j \cdot \nabla_{\mathbf{r}} V_{\text{el-a}}(\mathbf{r} - \mathbf{R}_j^0) + \mathcal{H}_{\text{lat}}. \quad (1.2)$$

This linear approximation is sufficient for most situations. However, it is expected to fail when the coupling strength between the electron and the lattice is too strong [10] or the physical system has some kind of symmetry that forbids the linear dependence of energy on lattice distortions [11]. The first two terms which describe the electron in a periodic potential are the only ones considered in the band theory: $\mathcal{H}_b\psi_{\mathbf{k}}(\mathbf{r}) = \varepsilon(\mathbf{k})\psi_{\mathbf{k}}(\mathbf{r})$, where the eigenstates are Bloch waves. The spin is irrelevant for a single electron (polaron) and its index is therefore dropped. In the tight-binding approximation and using the language of second quantization, \mathcal{H}_b is given as $\sum_{\mathbf{k}} \varepsilon(\mathbf{k})c_{\mathbf{k}}^\dagger c_{\mathbf{k}}$, where for a simple cubic lattice in d dimensions, $\varepsilon(\mathbf{k}) = \varepsilon_0 - 2t \sum_{i=1}^d \cos(k_i)$. t is the hopping amplitude and it describes the possibility of tunnelling between overlapping atomic states and ε_0 is the on-site energy. \mathbf{k} is known as the crystal momentum and it is unique only inside the first Brillouin zone (BZ), $-\pi/a < k_i \leq \pi/a$.

The next term describes the coupling to lattice distortions and its second quantized form depends on the specific form of the potential $V_{\text{el-a}}$. However, it can be written as

$$V_{\text{el-ph}} = \sum_{i,j} g(|\mathbf{R}_i^0 - \mathbf{R}_j^0|)c_i^\dagger c_i(b_j^\dagger + b_j) \quad (1.3)$$

since it couples the lattice distortion at \mathbf{R}_j^0 , $\mathbf{u}_j \propto (b_j^\dagger + b_j)$, to the electron density at $\mathbf{r} = \mathbf{R}_i^0$ and is a function of $\mathbf{r} - \mathbf{R}_j^0$. In momentum space, the

1.1. Hamiltonian for lattice polarons

corresponding electron-phonon couplings strength depends on the phonon momentum \mathbf{q} only

$$\mathcal{H} = \sum_{\mathbf{k}} \varepsilon(\mathbf{k}) c_{\mathbf{k}}^{\dagger} c_{\mathbf{k}} + \frac{1}{\sqrt{N}} \sum_{\mathbf{k}, \mathbf{q}} g(\mathbf{q}) c_{\mathbf{k}+\mathbf{q}}^{\dagger} c_{\mathbf{k}} (b_{-\mathbf{q}}^{\dagger} + b_{\mathbf{q}}) + \sum_{\mathbf{q}} \omega(\mathbf{q}) b_{\mathbf{q}}^{\dagger} b_{\mathbf{q}}, \quad (1.4)$$

where $N \rightarrow \infty$ is the number of lattice sites and the total momentum is assumed to be conserved. $b_{\mathbf{q}}$ is the phonon annihilation operator. It is assumed that there is only a single branch of phonons with energy dispersion $\omega(\mathbf{q})$, but generalizations to include multiple phonon modes is straightforward [12]. In this thesis we only focus on dispersionless optical phonons, $\omega(\mathbf{q}) = \Omega$, which in the long wavelength limit, correspond to out of phase motion of the neighbouring lattice sites. They are the relevant vibrational modes of ionic crystals, and are called optical because they can be excited by light and result in oscillating dipole moments. With further assumption of constant electron-phonon coupling, $g(\mathbf{q}) = g$, and nearest-neighbour hopping only, this reduces to the Holstein model [13] and in real space it corresponds to coupling of an electron to lattice distortions at the same site

$$\mathcal{H}_{\text{H}} = -t \sum_{\langle i, j \rangle} (c_i^{\dagger} c_j + \text{H.c.}) + g \sum_i c_i^{\dagger} c_i (b_i^{\dagger} + b_i) + \Omega \sum_i b_i^{\dagger} b_i. \quad (1.5)$$

This model was initially proposed to study molecular crystals with transverse vibrational degrees of freedom. Although it looks quite simple, there is no exact solution valid for the whole range of parameters. It has been studied using a variety of numerical and approximate analytical methods, including the Momentum-Average approximation (MA) [14] which we will use in this thesis. It shows the generic features associated with the polaron physics, such as the dependence of polaron properties on the structure of accompanying boson cloud and the crossover from a large to small polaron as the strength of electron-phonon coupling increases. When the coupling is large, the electron strongly distorts the lattice at the same site and the polaron becomes very heavy. This is a small polaron, whose phonon cloud is limited to the close vicinity of the electron. Weak electron-lattice coupling, on the other hand, only causes slight lattice distortions that are extended over several lattice sites. The polaron is accordingly much lighter in this case.

Note that the previous derivation, although typical of that found in textbooks, ignores a second important type of el-ph coupling: phonons can also couple to the kinetic energy of the electron by modifying its hopping amplitude. The latter depends exponentially on the distance between sites, which

varies as a result of lattice vibrations: $a \rightarrow a + u_{i+1} - u_i$ (one dimension). Such effects give rise to new coupling functions and will be encountered in a different context within this work (see chapter 4).

The Holstein model has exact solutions for the asymptotic limits of infinitely weak or strong coupling. For $g = 0$, there are no phonons and the Green's function is that of the free electron in the lattice,

$$G(\mathbf{k}, \omega) = \frac{1}{\omega - \varepsilon(\mathbf{k}) + i\eta} \quad (1.6)$$

where $\varepsilon(\mathbf{k})$ is the tight-binding energy dispersion. The other limit is the so called impurity limit, $t = 0$, where the solution is given by the Lang-Firsov formula [15],

$$G(\omega) = e^{-g^2/\Omega^2} \sum_{n=0}^{\infty} \frac{1}{n!} \left(\frac{g}{\Omega}\right)^{2n} \frac{1}{\omega - n\Omega + g^2/\Omega + i\eta}. \quad (1.7)$$

With $t = 0$ the polaron is localized at one site and has infinite mass; the Green's function is therefore independent of the momentum. The phonon number obeys a Poisson distribution, $|\psi(n)|^2 = e^{-g^2/\Omega^2} \frac{1}{n!} \left(\frac{g}{\Omega}\right)^{2n}$, and therefore the structure of phonon cloud is that of a coherent state, $b|\psi\rangle = \frac{g}{\Omega}|\psi\rangle$.

The spectrum is quite different for these two limits, going from a continuous band of energies $\varepsilon(\mathbf{k})$ into a set of discrete states $\varepsilon(n) = n\Omega - g^2/\Omega$, and it is of great interest to understand how the ground state and other excited states evolve as both g and t become finite. Perturbation theory can be used to extend the applicability range of the asymptotic results, but it fails for the intermediate parameter regimes. Various numerical schemes, such as the exact diagonalization (ED) [16–18] and quantum Monte Carlo (QMC) method [19–21], have been used to study Holstein polarons in this case. The MA approximation, which we will use in this thesis, is a semi-analytic approach that works reasonably well for the entire parameter range. It has a variational interpretation and its accuracy can be systematically improved.

Other examples of couplings include the Fröhlich [22], $g(\mathbf{q}) \propto 1/q$, the deformation coupling, $g(\mathbf{q}) \propto q$ and the breathing mode Hamiltonian for which $g(\mathbf{q}) \propto \sin(q/2)$ in one dimension [23, 24].

All this discussion assumes that the typical size of the polaron cloud is comparable with the lattice constant a . A different limit that has received much attention is that of the large polaron [25], whose cloud extends over a length scale exceeding a by orders of magnitude, so that the electron's dynamics can be treated in the continuous approximation where its kinetic

energy has again quadratic dependence on the momentum (but with a renormalized mass). While this is an interesting topic on its own, here we only consider lattice models and small polarons.

1.1.1 Polarons in systems with other forms of electron-boson coupling

In terms of the bare electron parameters, the electron-phonon coupling considered in Eq. (1.3) can be interpreted as the one modifying the on-site energy of electron since it is proportional to $c_i^\dagger c_i$. This causes the wavefunction of atomic orbitals occupied by the electron to change accordingly. As a result, the hopping amplitudes which are related to the overlap between these orbitals are also modified due to coupling to phonons. In the linear approximation, this gives rise to an additional electron-phonon coupling of the following form

$$\mathcal{H}'_{\text{el-ph}} = \sum_{\langle i,j \rangle, l} t_{ij,l} c_i^\dagger c_j (b_l^\dagger + b_l) + \text{H.c.} . \quad (1.8)$$

When expressed in the momentum representation, it corresponds to a coupling strength that depends on the momenta of both electron and phonon, $g(\mathbf{k}, \mathbf{q})$. Therefore, the coupling to phonons in this case modifies the kinetic energy of the electron. This type of coupling is encountered, for example, in the SSH model of conducting polymers [26, 27].

Although we introduced polarons in the context of electron-phonon coupling, one has to note that polaron physics is more general than this and is relevant to any situation where a charge carrier interacts with the collective excitations of an ordered environment. In cuprate superconductors, for example, doping holes move in the CuO_2 layer in which Cu spins are anti-ferromagnetically ordered. This motion disturbs the order of Cu spins and creates (*bosonic*) magnetic excitations, known as magnons, that dress the hole in the same way as phonons did with an electron in a distorted lattice. This is known as a spin or magnetic polaron and, based on different models and variational methods inspired by MA (see below), we will study them in chapters 4 and 5 of this thesis. We will see that this is a case of boson-modulated hopping.

1.2 Studying spectral properties using Green's function formalism

Green's functions are convenient mathematical tools for studying various static or dynamical properties of quantum systems, such as energy eigensystems and response functions. They are particularly useful for many-body problems where there are generally no exact solutions and perturbation or some other approximation is needed. There are different types of Green's functions, but the one we exclusively use in this thesis is the one-particle retarded Green's function defined as follows

$$\begin{aligned} G(\mathbf{k}, \tau) &= -i\langle 0|T[c_{\mathbf{k}}(\tau)c_{\mathbf{k}}^\dagger(0)]|0\rangle \\ &= -i\Theta(\tau)\langle 0|c_{\mathbf{k}}(\tau)c_{\mathbf{k}}^\dagger(0)|0\rangle \end{aligned} \quad (1.9)$$

where $c_{\mathbf{k}}(\tau) = e^{i\mathcal{H}\tau}c_{\mathbf{k}}e^{-i\mathcal{H}\tau}$ is the fermion annihilation operator in Heisenberg picture and $|0\rangle$ is the vacuum state. T is the time-ordering operator and $\Theta(\tau)$ is the Heaviside function, reflecting the fact that $c_{\mathbf{k}}|0\rangle = 0$. The usefulness of this quantity becomes apparent in its Lehmann representation,

$$G(\mathbf{k}, \omega) = \int_{-\infty}^{\infty} d\tau e^{i\omega\tau} G(\mathbf{k}, \tau) = \lim_{\eta \rightarrow 0^+} \sum_{\alpha} \frac{|\langle \psi_{\alpha} | c_{\mathbf{k}}^\dagger | 0 \rangle|^2}{\omega - E_{\alpha} + i\eta}, \quad (1.10)$$

where α are quantum numbers that identify a complete set of one-particle eigenstates $\{|\psi_{\alpha}\rangle\}$ of \mathcal{H} with energies $\{E_{\alpha}\}$: $\mathcal{H}|\psi_{\alpha}\rangle = E_{\alpha}|\psi_{\alpha}\rangle$. In a closed system where the total momentum is conserved, $[\mathcal{H}, \mathbf{P}] = 0$ and $|\psi_{\alpha}\rangle$ is therefore a momentum eigenstate with the same \mathbf{k} , otherwise $\langle \psi_{\alpha} | c_{\mathbf{k}}^\dagger | 0 \rangle = 0$.

Eq. (1.10) shows that the poles of the Green's function give the energy spectrum of the Hamiltonian and the associated residues contain information about the energy eigenfunctions. In many-body problems, the latter is also known as the quasiparticle weight, $Z_{\mathbf{k},\alpha} = |\langle \psi_{\alpha} | c_{\mathbf{k}}^\dagger | 0 \rangle|^2$, and it corresponds to the overlap between eigenstates of \mathcal{H} and those of the non-interacting problem. It hence contains information about the degree of renormalization of states of the system due to many-body interactions. It can also be used to extract various information about the quasiparticles such as their effective mass and the structure of the accompanying boson cloud [14]. In addition, the imaginary part of the Green's function is the spectral function

$$A(\mathbf{k}, \omega) = -\frac{1}{\pi} \text{Im}G(\mathbf{k}, \omega) = \sum_{\alpha} Z_{\mathbf{k},\alpha} \delta(\omega - E_{\alpha}) \quad (1.11)$$

and, in angle-resolved photo-emission experiments, it is related to the current of outgoing photo-electrons with momentum \mathbf{k} [28]. The total density

1.3. Green's function of the Holstein model and its variational calculation

of states is given by integrating $A(\mathbf{k}, \omega)$ over entire momenta in the first BZ

$$\rho(\omega) = \int_{\text{BZ}} d\mathbf{k} A(\mathbf{k}, \omega). \quad (1.12)$$

When there is disorder in the lattice, the crystal momentum \mathbf{k} is not conserved and one has to work in the real-space basis,

$$G_{ij}(\omega) = \langle 0 | c_i \hat{G}(\omega) c_j^\dagger | 0 \rangle \quad (1.13)$$

where $\hat{G}(\omega) = 1/(\omega - \mathcal{H} + i\eta)$ is the resolvent of Hamiltonian, \mathcal{H} . It gives the local density of state (LDOS)

$$\rho(\mathbf{R}_i, \omega) = -\frac{1}{\pi} \text{Im} G_{ii}(\omega) = \sum_{\alpha} |\psi_{\alpha}(\mathbf{R}_i)|^2 \delta(\omega - E_{\alpha}), \quad (1.14)$$

which can be studied to find the spatial profile of eigenstates $\psi_{\alpha}(\mathbf{R}_i)$. We will use this quantity in order to identify localized states of polarons near various types of impurities.

1.3 Green's function of the Holstein model and its variational calculation

Variational methods will be extensively used throughout this thesis as a way of doing nonperturbative calculations. The general idea is to exclude states that are unlikely to be realized by the system, due to energetic reasons for example, and only keep a particular subspace of the Hilbert space that involves the more relevant states. This is generally accomplished by separating the Hamiltonian into an easy part which can be trivially diagonalized, and the rest of the Hamiltonian which usually involves many-body interactions, $\mathcal{H} = \mathcal{H}_0 + \mathcal{H}_1$, and then using the Dyson's identity:

$$\hat{G}(\omega) = \hat{G}_0(\omega) + \hat{G}(\omega) \mathcal{H}_1 \hat{G}_0(\omega), \quad (1.15)$$

where $\hat{G}_0(\omega) = 1/(\omega - \mathcal{H}_0 + i\eta)$ is the resolvent associated with the easy part, \mathcal{H}_0 . Acting by \mathcal{H}_1 upon any state that is within the subspace of interest will eventually link to states that lie outside it. Discarding such states results in a simplified set of equations between various Green's function, which can be solved efficiently to find the desired Green's functions. One advantage of this variational approach is its controlled accuracy: one can always enlarge the variational space until an acceptable level of accuracy is achieved.

The Green's function of the Holstein model has been evaluated using a variational scheme based on this general approach, known as the momentum-average approximation (MA) [14], where the spatial extent of the phonon cloud can be varied to improve the accuracy. MA has been successful in accurately calculating various properties of the Holstein polaron in clean systems. In the next two chapters, we will extend it to systems with various kinds of disorder.

1.4 Overview of thesis and further reading

So far, we have assumed that the lattice in which the electron moves is clean of any sort of disorder and its only deviation from complete periodicity is due to lattice distortions. In reality, however, disorder is introduced into lattice structures during sample growth and preparation and it hinders the motion of electrons even in the absence of lattice distortions. When disorder is weak compared to kinetic energy of electrons, the main effect of disorder is to scatter electrons between different Bloch states and this limits the lifetime of these states. For strong disorder, however, it was proposed in seminal work by Anderson [29] that, in three spatial dimensions, electrons with certain energies become exponentially localized in finite regions of the lattice as a result of destructive interference between multiply scattered electron waves from various impurity sites. As such localized electrons lack itinerant properties, the solid turns into an electrical insulator when localization happens for states near Fermi energy [30]. While it takes a finite amount of disorder to localize all electronic states in three dimensions, this is achieved for any amount of disorder in one and two dimensions². Once again, this picture applies to bare electrons which move freely in the lattice in the absence of disorder. In systems of strongly interacting electrons, there are other insulating states which arise even in the absence of any disorder. They are known as Mott insulators in which the electrons are confined into atomic-like states due to strong repulsion with other electrons. Therefore, the charge fluctuations become strongly suppressed and magnetic order develops at low energies.

Compared to bare electrons, polarons are expected to be more susceptible to external disorder because of their enhanced effective mass. In other words, the same amount of disorder is effectively stronger when measured against the polaron's reduced kinetic energy. Although this is in principle true, it implicitly assumes that the heavier polaron interacts with the same

²In two dimensions, states are only logarithmically localized when disorder is weak [31].

disorder potential as the bare electron does.

In chapter 2, based on the extension of the momentum-average approximation to inhomogeneous systems, we will challenge this picture by closely examining the interplay between disorder and coupling to phonons for the case of Holstein polaron [32]. As the electron-phonon coupling becomes stronger, the simple picture where the effect of coupling to phonons can be cast into the enhancement of the effective mass starts to fail and modifications in the form of renormalization of the disorder potential by phonons become important. These modifications reflect the fact that, due to the binding between the electron and its phonon cloud, the electron's ability to interact with existing disorder is affected in a way that depends on the structure of the cloud surrounding it. This reveals previously unexplored aspects of interaction of polaronic quasiparticles with external potentials and makes predictions that defy naive expectations [33]. This formalism will be applied to study bound states of a three-dimensional Holstein polaron near various kinds of single impurities. The accuracy of MA approximation is confirmed by comparing our results to that of exact numerical treatments, when available. For a detailed review of the historical development of lattice polarons and various techniques developed for studying them, including the MA approximation, the reader may refer to Ref. [34] and [35].

We continue on this track in chapter 3, where the effect of weak but extended disorder on the lifetime of Holstein polarons is studied. Different behaviours are recovered in the weak and strong coupling regimes and the role of disorder renormalization and the validity of results at strong-coupling limit will be discussed.

Next, we study the spin polaron description of holes doped into antiferromagnetic insulators. The motivation is to study the spectral properties of a single charge carrier in hole-doped copper-oxide superconductors. This is an intrinsically multi-band problem where there are several Cu and O orbitals involved, but in chapter 4 we use an effective one-band description (based on the Zhang-Rice singlet picture [36]) in order to study the trapping of polarons of this model near an attractive impurity. Renormalization of impurity potential due to coupling to magnons is shown to be relevant to this problem as well and the role of magnetic sublattices in this regard will be discussed.

In the last chapter, a more realistic model for a hole in the CuO_2 layer is considered. It has been originally proposed and solved using exact diagonalization techniques in Ref. [3]. Here, we propose a semi-analytic solution which is based on a variational principle similar to that used to generate the MA approximation for lattice polarons. Our approach will prove to be very

1.4. Overview of thesis and further reading

fast and efficient numerically and, unlike the ED method, it does not suffer from finite-size effects. We recover the hole's energy dispersion in agreement with ARPES measurements of the parent compound and determine the role of various terms in the Hamiltonian in giving rise to its generic features. The efficiency of our method enables us to include orbitals that are usually neglected in other studies of cuprates and gauge their effects on the quasiparticle's spectral properties.

Chapter 2

Trapping of three-dimensional Holstein polarons by various impurities

2.1 Introduction

The challenge to understand the effects of disorder on the behavior of particles strongly coupled to bosons from their environment is commonly encountered in correlated electron systems. For example, high- T_c cuprates are doped anti-ferromagnetic insulators in which, beside strong coupling to magnons, ARPES measurements have also provided evidence for strong electron-phonon coupling [37]. At the same time, charge carriers moving in the CuO_2 layers are subject to random disorder potentials from the adjacent dopant layers. Substituting only a few percent of the Cu atoms with impurities suppresses superconductivity by localizing the low energy electronic states [38]. Inhomogeneities in the superconducting gap measured in high resolution tunnelling experiments have been attributed to atomic scale disorder in the phonon energy and the electron-phonon coupling strength in these materials [39].

The result of the interplay between disorder and coupling to such phonons depends on their relative strengths. Disorder that is considered weak for free electrons can be strong enough to localize a polaron, that is the dressed quasiparticle which consists of the electron together with its cloud of phonons, because of its heavy effective mass. On the other hand, whereas in the weak disorder regime electron-phonon coupling hinders the motion of electrons, such coupling actually facilitates the electron mobility in the strongly disordered regime where the Anderson localization prevails [40].

Certain aspects of this problem have been studied with various approximations, most of which rely on sophisticated non-perturbative methods [41]

such as the statistical dynamic mean field theory (DMFT) [42, 43], or dynamical coherent potential approximation (DCPA) [44, 45].

In this chapter we focus on Holstein polarons which are quasiparticles comprising a charge carrier plus a cloud of Einstein phonons describing the lattice distortions in the vicinity of the charge carrier [13]. We consider the simplest case of a single impurity and study the formation of polaronic bound states near that impurity. This problem has been studied using various numerical techniques, such as diagrammatic Monte Carlo (DMC) [4] and continuous time quantum Monte Carlo techniques [46]. Here, we use a generalization of the Momentum Average (MA) approximation to inhomogeneous systems [1] in order to study this problem. The method can, in principle, be used to study all possible types of disorder for various kinds of electron-phonon coupling. Here, we stick to the Holstein-type coupling, but consider different types of disorder due to single impurities, namely a variation in the on-site energy, in the electron-phonon coupling and/or in the phonon energy, whereas the previous studies only considered impurities of the first type. The accuracy of our method for this case is demonstrated by comparison with DMC results.

The chapter is organized as follows: In Sec. 2.2 we describe our method and discuss its meaning (full details are provided in the Appendix A and B.). Sec. 2.3 presents our results for the three types of impurities, and Sec. 2.4 contains the summary.

2.2 Momentum average approximation for inhomogeneous systems

We start with deriving the MA approximation for a lattice that has disorder in the form of random on-site energies, inhomogeneities in the strength of electron-phonon coupling and phonon frequencies. A simpler case (with only on-site disorder) has been briefly discussed in Ref. [1]. The Holstein Hamiltonian for such a lattice is

$$\mathcal{H} = \mathcal{H}_d + \hat{V}_{\text{el-ph}} = \mathcal{H}_0 + \hat{V}_d + \hat{V}_{\text{el-ph}}, \quad (2.1)$$

where \mathcal{H}_d describes the non-interacting part of the Hamiltonian, including

$$\mathcal{H}_0 = -t \sum_{\langle i,j \rangle} (c_i^\dagger c_j + \text{H.c.}) + \sum_i \Omega_i b_i^\dagger b_i$$

2.2. Momentum average approximation for inhomogeneous systems

which contains the kinetic energy of the particle and energy of the boson modes ($\hbar = 1$), and

$$\hat{V}_d = \sum_i \epsilon_i c_i^\dagger c_i$$

describing the on-site disorder. The interaction part

$$\hat{V}_{\text{el-ph}} = \sum_i g_i c_i^\dagger c_i (b_i^\dagger + b_i)$$

describes the inhomogeneous Holstein-like coupling [13] between the particle and the bosons. Here, i indexes sites of a lattice which can be in any dimension, and of finite or infinite extent. The operators c_i and b_i describe, respectively, particle and boson annihilation from the corresponding state associated with lattice site i . The spin of the particle is ignored because it is irrelevant in this case, but generalizations are straightforward [47]. For simplicity, we assume nearest-neighbour hopping; this approximation can also be trivially relaxed. Depending on the model of interest, the on-site energies ϵ_i , electron-phonon couplings g_i and phonon frequencies Ω_i can be assumed to be random variables.

Our goal is to calculate the zero temperature single particle retarded Green's function (GF) in real space

$$G_{ij}(\omega) = \langle 0 | c_i \hat{G}(\omega) c_j^\dagger | 0 \rangle = \sum_\alpha \frac{\langle 0 | c_i | \alpha \rangle \langle \alpha | c_j^\dagger | 0 \rangle}{\omega - E_\alpha + i\eta}, \quad (2.2)$$

where $|0\rangle$ is the vacuum state where there are no phonons or charge carrier in the lattice, $\hat{G}(\omega) = (\omega - \mathcal{H} + i\eta)^{-1}$ is the resolvent of \mathcal{H} with $\eta \rightarrow 0^+$, and E_α , $|\alpha\rangle$ are single polaron eigenenergies and eigenstates of the Hamiltonian, $\mathcal{H}|\alpha\rangle = E_\alpha|\alpha\rangle$. Note that α refers to a set of quantum numbers that together uniquely label the eigenstates of \mathcal{H} . Knowledge of this GF allows us to find the spectrum from the poles, and the local density of states (LDOS) which is measured in scanning tunnelling microscopy (STM) experiments, $\rho(i, \omega) = -\frac{1}{\pi} \text{Im} G_{ii}(\omega)$.

To calculate this quantity, we repeatedly use Dyson's identity: $\hat{G}(\omega) = \hat{G}^d(\omega) + \hat{G}(\omega) \hat{V}_{\text{el-ph}} \hat{G}^d(\omega)$, where $\hat{G}^d(\omega) = (\omega - \mathcal{H}_d + i\eta)^{-1}$. The first equation of motion generated this way reads as

$$G_{ij}(\omega) = G_{ij}^d(\omega) + \sum_l g_l F_{il}^{(1)}(\omega) G_{lj}^d(\omega), \quad (2.3)$$

where

$$G_{ij}^d(\omega) = \langle 0 | c_i \hat{G}_d(\omega) c_j^\dagger | 0 \rangle \quad (2.4)$$

2.2. Momentum average approximation for inhomogeneous systems

are, in principle, known quantities and we have introduced the generalized GFs

$$F_{ij}^{(n)}(\omega) = \langle 0 | c_i \hat{G}(\omega) c_j^\dagger b_j^{\dagger n} | 0 \rangle.$$

Note that $F_{ij}^{(0)}(\omega) = G_{ij}(\omega)$. Next, we generate equations of motion for these generalized GFs. Using the Dyson identity, for any $n \geq 1$, results in

$$\begin{aligned} F_{ij}^{(n)}(\omega) &= \sum_{l \neq j} g_l G_{lj}^d(\omega - n\Omega_j) \langle 0 | c_i \hat{G}(\omega) c_l^\dagger b_l^\dagger b_j^{\dagger n} | 0 \rangle \\ &+ g_j G_{jj}^d(\omega - n\Omega_j) \left[F_{ij}^{(n+1)}(\omega) + n F_{ij}^{(n-1)}(\omega) \right]. \end{aligned} \quad (2.5)$$

This equation relates $F^{(n)}$ not only to other GFs of a similar type, but also introduces new propagators with phonons at two different sites. Equations of motions can be written for these new GFs, linking them to yet more general GFs, and so on and so forth. The resulting hierarchy of coupled equations describes the problem exactly, but is unmanageable. Approximations are needed to simplify it and find a closed-form solution.

The main idea behind the MA approximations is to simplify this set of equations by dropping exponentially small contributions in each equation of motion. At the simplest level – the so-called MA⁰ approximation – we ignore the first term in Eq. (2.5) for any $n \geq 1$. This is reasonable at low energies, $\omega \sim E_{GS}$, where $\omega - n\Omega_j$ is well below the energy spectrum of \mathcal{H}_d and, therefore, $G_{lj}^d(\omega - n\Omega_j)$ is guaranteed to decrease exponentially with increasing distance $|l - j|$. Therefore, we keep only the largest propagator corresponding to $l = j$, and ignore exponentially smaller $l \neq j$ contributions. Although this is the simplest possible such approximation, it is already accurate at low energies, as shown in the results section. It can also be systematically improved, as discussed below. First, however, we complete this MA⁰-level solution.

The simplified equation of motion now reads as

$$F_{ij}^{(n)}(\omega) = g_j G_{jj}^d(\omega - n\Omega_j) \left[F_{ij}^{(n+1)}(\omega) + n F_{ij}^{(n-1)}(\omega) \right]. \quad (2.6)$$

On physical grounds, we expect that $F_{ij}^{(n)}(\omega)$ must vanish for sufficiently large n , because its Fourier transform corresponds to the probability amplitude that a particle injected in the system will generate n phonons at a later time (or annihilate all n phonons that were initially present), and this becomes unlikely as n increases. Therefore, this recursive relation admits a solution as

$$F_{ij}^{(n)}(\omega) = A_n(j, \omega) F_{ij}^{(n-1)}(\omega), \quad (2.7)$$

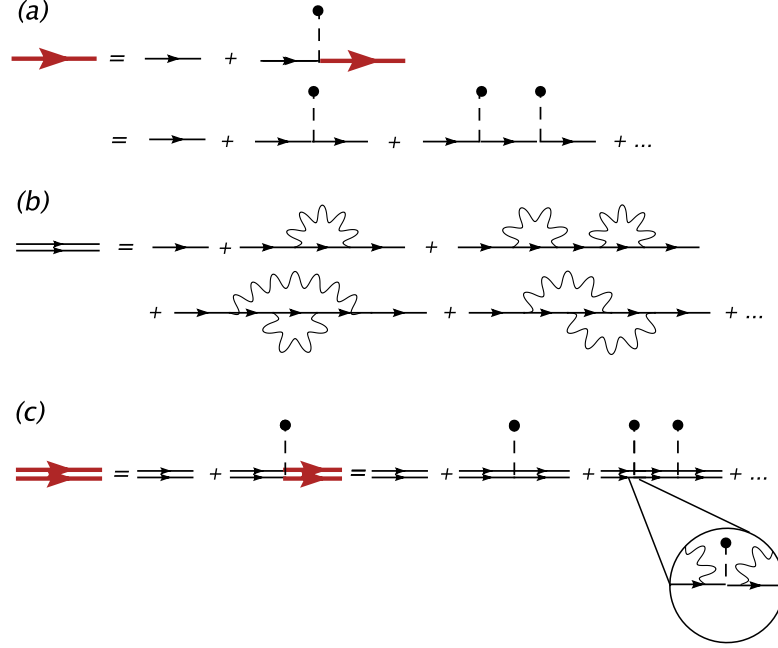


Figure 2.1: Diagrammatic expansion for (a) the disorder GF $G_{ij}^d(\omega)$ (bold red line); (b) the polaron GF in a clean system $G_{ij}^0(\tilde{\omega})$ (double thin line), and (c) the “instantaneous” approximation for the polaron GF in a disordered system, $G_{ij}^d(\tilde{\omega})$ (double bold red line). The thin black lines depict free electron propagators, the wiggly lines correspond to phonons, and scattering on the disorder potential is depicted the dashed lines ending with circles. See text for more details.

where using Eq. (2.7) in (2.6) gives $A_n(j, \omega)$ as the following continued fraction

$$A_n(j, \omega) = \frac{ng_j G_{jj}^d(\omega - n\Omega_j)}{1 - g_j G_{jj}^d(\omega - n\Omega_j) A_{n+1}(j, \omega)}. \quad (2.8)$$

This can be efficiently evaluated starting from a sufficiently large cutoff N_c such that $A_{N_c+1}(j, \omega) = 0$. Generally speaking, N_c must be much larger than the average number of phonons expected at site j ; in practice, the cutoff is increased until convergence is reached to within the desired accuracy. Substituting $F_{ij}^{(1)}(\omega) = A_1(j, \omega)G_{ij}(\omega)$ in Eq. (2.3) leads to a closed system

2.2. Momentum average approximation for inhomogeneous systems

of linear equations for the original GF:

$$G_{ij}(\omega) = G_{ij}^d(\omega) + \sum_l G_{il}(\omega) g_l A_1(l, \omega) G_{lj}^d(\omega). \quad (2.9)$$

This equation has a similar structure to the equation linking the disorder GF, $G_{ij}^d(\omega)$, to that of the free particle $G_{ij}^0(\omega) = \langle 0 | c_i(\omega - \mathcal{H}_0 + i\eta)^{-1} c_j^\dagger | 0 \rangle$ (in the absence of coupling to phonons), which is depicted diagrammatically in Fig. 2.1(a), and which reads as

$$G_{ij}^d(\omega) = G_{ij}^0(\omega) + \sum_k G_{ik}^d(\omega) \epsilon_k G_{kj}^0(\omega). \quad (2.10)$$

This analogy shows that coupling to phonons renormalizes the on-site disorder as $\epsilon_l \rightarrow \epsilon_l + g_l A_1(l, \omega)$. Note that $A_1(l, \omega)$ depends not only on the local phonon frequency Ω_l , coupling g_l and ϵ_l , but also on *all* bare on-site energies $\{\epsilon_k\}$ through the disorder GF G_{ll}^d . This is the simplest example of the emergence of a renormalized potential for this problem, that is made very transparent within the MA approximation.

While Eq. (2.9) can be solved directly for a finite-size system, we can improve its efficiency and reveal a different physical interpretation by explicitly removing the ‘‘average’’ contribution due to the electron-phonon interactions. Let g and Ω be the average values of the electron-phonon coupling and phonon energies. We assume that the on-site energy average is zero, $\bar{\epsilon}_i = 0$, (a finite value results in a trivial shift of all energies). Then, let

$$A_n(\omega) = \frac{ngg_0(\omega - n\Omega)}{1 - gg_0(\omega - n\Omega)A_{n+1}(\omega)} \quad (2.11)$$

be the continued fractions corresponding to these average parameters, where we use the short-hand notation

$$g_0(\omega) = G_{ii}^0(\omega) = \frac{1}{N} \sum_{\mathbf{k}} \frac{1}{\omega - \varepsilon(\mathbf{k}) + i\eta}$$

for diagonal elements of the free propagator in the absence of disorder. It is given by the momentum average of the free propagator over the Brillouin zone, where $\varepsilon(\mathbf{k})$ is the free particle energy dispersion: $\varepsilon(\mathbf{k}) = -2t \sum_{i=1}^3 \cos k_i$. The ‘‘average’’ renormalization of the on-site energy is now recognized to represent the corresponding MA⁰ self-energy for a ‘‘clean’’ system, i.e. a homogeneous system with average coupling and phonon frequency,

$$\Sigma_{\text{MA}^0}(\omega) = gA_1(\omega),$$

2.2. Momentum average approximation for inhomogeneous systems

see, for instance, Eqs. (11) and (12) of Ref. [48].

Introducing the effective disorder potential

$$v_0(l, \omega) = g_l A_1(l, \omega) - \Sigma_{\text{MA}^0}(\omega), \quad (2.12)$$

Eq. (2.9) can be rewritten as

$$G_{ij}(\omega) = G_{ij}^d(\tilde{\omega}) + \sum_l G_{il}(\omega) v_0(l, \omega) G_{lj}^d(\tilde{\omega}), \quad (2.13)$$

where $\tilde{\omega} = \omega - \Sigma_{\text{MA}^0}(\omega)$. This energy renormalization, $\omega \rightarrow \tilde{\omega}$, reflects the fact that processes describing the formation of polaron in the “clean” system have been explicitly summed.

Note that solving Eq. (2.13) is numerically more efficient compared to Eq. (2.9), especially when disorder is confined to a finite region in the system, away from which $v_0(l, \omega)$ vanishes rapidly. As explained below, Eq. (2.12) reveals a different interpretation of the interplay between disorder and electron-phonon coupling.

Consider first the meaning of $G_{ij}^d(\tilde{\omega})$, which would be the solution if we could ignore $v_0(j, \omega)$. In the absence of on-site disorder this term equals $G_{ij}^0(\tilde{\omega})$, that is the expected solution for a polaron in the clean system, depicted diagrammatically in Fig. 2.1(b) (of course, here the exact self-energy is approximated to $\Sigma_{\text{MA}^0}(\omega)$). Comparing Figs. 2.1(a) and 2.1(b), it follows that $G_{ij}^d(\tilde{\omega})$ is the sum of the diagrams shown in Fig. 2.1(c).

At first sight, this seems to be the full answer for this problem, since these diagrams sum the contributions of all the processes in which the polaron scatters once, twice, etc., on the disorder potential. This is certainly the answer obtained in the limit of an “instantaneous” approximation valid when $\Omega \rightarrow \infty$, i.e. when the ions are very light and respond instantaneously to the motion of electrons. In this case, one can perform a Lang-Firsov transformation and after an additional averaging over phonons, one arrives at the following approximative effective Hamiltonian [46, 49]

$$\mathcal{H}_{\text{inst}} = -t^* \sum_{\langle i,j \rangle} (c_i^\dagger c_j + \text{H.c.}) + \sum_i \left(\epsilon_i - \frac{g^2}{\Omega} \right) c_i^\dagger c_i, \quad (2.14)$$

where $t^* = t \exp(-g^2/\Omega^2)$ is the renormalized polaron hopping, and $-g^2/\Omega$ is the polaron formation energy (for simplicity, here we assume that the phonon energies and electron-phonon coupling are homogeneous, $g_i \rightarrow g, \Omega_i \rightarrow \Omega$). The GF of this Hamiltonian is also given by Fig. 2.1(c), if the polaron

2.2. Momentum average approximation for inhomogeneous systems

propagator is approximated by

$$G_{ij}^0(\tilde{\omega}) \rightarrow \frac{1}{N} \sum_{\mathbf{k}} \frac{e^{i\mathbf{k}\cdot(\mathbf{R}_i - \mathbf{R}_j)}}{\omega - \varepsilon^*(\mathbf{k}) + \frac{g^2}{\Omega} + i\eta},$$

where $\varepsilon^*(\mathbf{k})$ uses the renormalized kinetic energy. Of course, using the full expression for $G_{ij}^0(\tilde{\omega})$ is preferable since the self-energy $\Sigma_{\text{MA}^0}(\omega)$ describes much more accurately the overall energy shift and effective mass renormalization than those asymptotic expressions, and it also includes the quasiparticle weight.

That $G_{ij}^d(\tilde{\omega})$ cannot be the full answer becomes obvious when we rewrite the clean polaron propagators in terms of free particle and phonon lines, i.e., we substitute the expansion corresponding to Fig. 2.1(b) in 2.1(c). Doing so reveals that, within this “instantaneous” approximation, scattering of the electron on the disorder potential is allowed only when no phonons are present, see zoom-in in Fig. 2.1(c). However, for moderate and large electron-phonon coupling, one expects the probability to find no phonons in the system to be exponentially small, therefore the processes summed in Fig. 2.1(c) have very low probabilities.

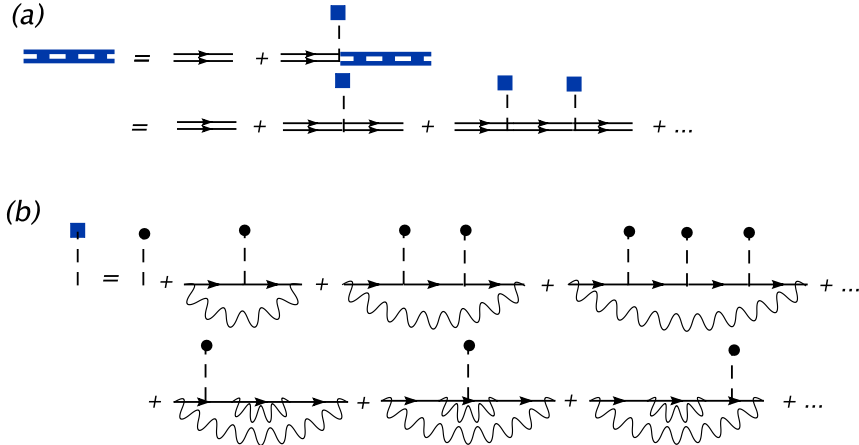


Figure 2.2: (color online) (a) Diagrammatic expansion for the full MA solution $G_{ij}(\omega)$ (thick dashed blue line) in terms of the clean polaron Green’s function (double thin line) and scattering on the renormalized disorder potential $\epsilon_i^*(\omega)$, depicted by dashed lines ended with squares. (b) Diagrammatic expansion of $\epsilon_i^*(\omega)$. For more details, see text.

What is missing in Fig. 2.1(c) are diagrams describing the scattering of the electron on the disorder potential in the presence of the phonons from

2.2. Momentum average approximation for inhomogeneous systems

the polaron cloud. Their contribution is included through the renormalized potential $v_0(l, \omega)$ in the second term of Eq. (2.13). Indeed, the full MA solution shows that the polaron scatters not on the bare disorder ϵ_l , but on the renormalized disorder potential

$$\epsilon_l^*(\omega) = \epsilon_l + v_0(l, \omega), \quad (2.15)$$

as depicted in Fig. 2.2(a). The diagrammatic expansion of the additional term $v_0(l, \omega)$, shown in Fig. 2.2(b), verifies that it indeed describes the effective scattering in the presence of various number of phonons.

Taken together, the diagrams summed in Fig. 2.2 represent all possible contributions to the polaron propagator in the disordered system. The MA^0 approximation consists of discarding exponentially small contributions from each of these diagram, as already discussed. MA^0 also has an exact variational meaning, namely of assuming that the polaron cloud can have phonons only on a single site, in direct analogy with the clean case [50, 51]. It is quite remarkable that all diagrams corresponding to this variational approximation can still be summed analytically in closed form, even in the presence of disorder.

As it is the case for the clean system, MA can be systematically improved by keeping more terms in Eq. (2.5). In particular, at the MA^1 level, we treat the equation for the $F^{(1)}$ functions exactly, and discard exponentially small off-diagonal propagators only for $n \geq 2$. The logic here is that the propagators appearing in $F^{(1)}$ have the highest energy, therefore the slowest exponential decay. The MA^1 equations can also be solved in closed form. The details are presented in the Appendix B. The final solution looks identical to Eq. (2.13), except the renormalized energy is now $\tilde{\omega} = \omega - \Sigma_{\text{MA}^1}(\omega)$ while the renormalized potential $v_0(l, \omega)$ is replaced by a more complicated, yet more accurate expression $v_1(l, \omega)$. The meaning of all these quantities, however, is the same.

To summarize, MA reveals that the role of electron-phonon coupling is two-fold. On one hand, it renormalizes the quasiparticle properties due to polaron formation, just like in the clean system (as revealed by the explicit appearance of the “clean” system self-energy). However, this coupling also renormalizes the disorder potential experienced by the particle, $\epsilon_l \rightarrow \epsilon_l^*(\omega)$. As we show later for various types of disorder, this renormalization is non-trivial in that it has strong retardation effects, and has significant consequences. “Instantaneous” approximations completely ignore this renormalization, and therefore miss essential physics. In contrast, MA gives a closed analytical expression for all quantities of interest, in a formulation whose

meaning is very transparent and whose accuracy can be systematically improved.

2.3 Polaron near a single impurity

We now apply the general formalism described above to the simplest type of “disorder”, namely an otherwise clean three-dimensional simple cubic lattice with a single impurity. Impurities which modulate the on-site energy, the strength of the electron-phonon coupling and/or the phonon frequency are separately considered. We investigate under what conditions such impurities can trap the polaron.

As a reference case, we first review briefly the solution in the absence of electron-phonon coupling. In this case, the impurity can only modulate the on-site potential, $\epsilon_i = -U\delta_{i0}$, and the Hamiltonian reduces to the Wolff-Clogston model [52, 53]:

$$\mathcal{H}_d = -t \sum_{\langle i,j \rangle} (c_i^\dagger c_j + \text{H.c.}) - U c_0^\dagger c_0 = \mathcal{H}_0 + \hat{V}_d. \quad (2.16)$$

For this form of \hat{V}_d , Eq. (2.10) reads as

$$G_{ij}^d(\omega) = G_{ij}^0(\omega) - U G_{i0}^d(\omega) G_{0j}^0(\omega), \quad (2.17)$$

which is trivially solved to give

$$G_{ij}^d(\omega) = G_{ij}^0(\omega) - U \frac{G_{i0}^0(\omega) G_{0j}^0(\omega)}{1 + U G_{00}^0(\omega)}. \quad (2.18)$$

Because of translational and time reversal symmetry, $G_{ij}^0(\omega) = G_{i-j,0}^0(\omega) = G_{j-i,0}^0(\omega)$, etc. The LDOS at the impurity site $i = 0$ is then found to be

$$\rho_d(0, \omega) = -\frac{1}{\pi} \text{Im} G_{00}^d(\omega) = \frac{\rho_0(0, \omega)}{|1 + U G_{00}^0(\omega)|^2}, \quad (2.19)$$

where $\rho_0(0, \omega) = -\frac{1}{\pi} \text{Im} G_{00}^0(\omega)$ is the LDOS in the clean system (same as total DOS, because of the translational invariance). As a result, a bound state below the continuum, signalled by a delta-function peak in $\rho(0, \omega)$, occurs if and only if the denominator of Eq. (2.19) vanishes. For a 3D simple cubic lattice with an attractive impurity, this means that an impurity bound state appears if there is an energy $E < -6t$ such that $\text{Re} G_{00}^0(E) = -1/U$ (below the continuum, the imaginary part of $G_{00}^0(E)$ vanishes). This

2.3. Polaron near a single impurity

equation can be solved graphically to find that a bound state appears for any $U \geq U_c = -\frac{1}{\text{Re}G_{00}^0(-6t)} \sim 3.96t$.

In the presence of electron-phonon coupling the equations are more complicated, but the idea is the same: we calculate the LDOS at the impurity site and compare it to the DOS of the clean system. If the former has a peak below the threshold of the latter, then a bound state exists at that energy. We then vary U to find the threshold value above which a bound state is guaranteed. More details about the impurity state, such as its localization length, statistics for the phonon cloud, etc., can be extracted from the LDOS at sites in the neighbourhood of the impurity. Here we focus on identifying when bound impurity states are stable.

2.3.1 Impurity changing the on-site energy

The Hamiltonian describing this case is

$$\mathcal{H} = \hat{T} + \Omega \sum_i b_i^\dagger b_i + g \sum_i c_i^\dagger c_i (b_i + b_i^\dagger) - U c_0^\dagger c_0, \quad (2.20)$$

where \hat{T} is the particle's tight-binding kinetic energy. We are interested in attractive impurities, $U > 0$, when an impurity state can be bound near the impurity site. To find the LDOS at the impurity site, we need to solve Eq. (2.13) to find $G_{00}(\omega)$. Note that now $G_{ij}^d(\omega)$ is known, being given by Eq. (2.18). The free-particle propagators $G_{ij}^0(\omega) = \frac{1}{N} \sum_{\mathbf{k}} \frac{e^{i\mathbf{k} \cdot (\mathbf{R}_i - \mathbf{R}_j)}}{\omega - \varepsilon(\mathbf{k}) + i\eta}$, where for the simple cubic lattice $\varepsilon(\mathbf{k}) = -2t \sum_{i=1}^3 \cos k_i$, can be calculated by doing the integrals over the Brillouin zone. A more efficient approach, which we use, is discussed in Ref. [54], and also in chapters 4 and 5.

Since the disorder GF approaches to the bulk GF away from the impurity, $G_{ll}^d(\omega) \rightarrow G_{ll}^0(\omega)$ when $|l| \rightarrow \infty$, the renormalized impurity potential decays fast at these sites as $A_1(l, \omega) \rightarrow A_1(\omega)$. Physically, this is because the impurity has less and less influence at sites far from where it is located. Mathematically, this follows from Eq. (2.18) and the fact that $G_{l0}^0(\omega - n\Omega)$ decreases exponentially with the distance between site l and the origin, at energies below the free particle continuum which are of interest here. As a result, in Eq. (2.13) we only need to sum over sites l close to the impurity, and this small system of equations can be solved very efficiently.

The appropriate value for this cutoff varies depending on the various parameters, but generically it decreases as the energies of interest become lower. Physically, this can be understood as follows. First, let us explain why is the renormalized disorder potential non-local, even though the bare

2.3. Polaron near a single impurity

impurity potential is local. The answer is provided by the diagrams which contribute to it, see Fig. 2.2(b). Consider, for simplicity, the MA⁰ approximation. In this case, all phonon lines appearing in these diagrams start and end at the site l for which $v_0(l, \omega)$ is being calculated – this is the site where the phonon cloud is located. However, the electron is found with various probabilities away from the polaron cloud, so it can scatter on the impurity if this is located within the “radius” of the polaron, where the electron is most likely to be found. In other words, the range of the renormalized potential is controlled by the polaron size. From medium to large couplings, as the polaron becomes smaller, the renormalized potential becomes more local. At small couplings, though, the distance between the electron and its phonon cloud can be appreciable, and the range of the effective disorder potential increases. All this is clearly manifest in the expansion of $v_0(l, \omega)$ to the lowest order in electron-phonon coupling g ,

$$v_0(l, \omega) \approx g^2 [G_{l0}^d(\omega - \Omega) - G_{l0}^0(\omega - \Omega)] = \frac{-Ug^2}{1 + Ug_0(\omega)} G_{l0}^0(\omega - \Omega) G_{0l}^0(\omega - \Omega),$$

which shows direct proportionality to the ability of particle to visit the impurity in the presence of a phonon, $G_{l0}^0(\omega - \Omega)$.

In Fig. 2.3(a) we plot $\rho(0, \omega)$ over a wider energy range, for several values of U , within MA⁰ approximation. The dashed line shows the DOS of the clean system, multiplied by 100 for visibility. For $U/t = 1.8, 1.9$, the impurity attraction is not sufficient to bind a state below the continuum, although the LDOS is pushed towards the lower band-edge. For $U = 1.95t$, there is a peak just below the continuum. Because of the finite value of η , the two features are not completely separated and the continuum onset looks like a “shoulder”, however lowering η allows us to clearly separate the two features. Finally, for $U = 2t$ the bound state peak is clearly below the continuum, so in this case threshold value of impurity attraction for a bound state to appear is $U_c \approx 1.95t$. This U_c value coincides with the DMC result, although our polaron energies are slightly higher than the exact DMC values shown in Fig. 2.3(e), as expected for a variational approximation. Increasing the variational space by going to MA¹ level significantly improves the agreement with the DMC since all features move toward lower energies, see Fig. 2.3(c). The critical value of $U_c \approx 1.95t$ for which an impurity state appears below the continuum is only slightly affected, in spite of the overall shift of the spectral weights.

The dependence of the bound state energy on the cutoff is shown in Figs. 2.3(b) and (d) for MA⁰ and MA¹, respectively, when $U = 2t$, $\Omega = 2t$ and the effective coupling $\lambda = \frac{g^2}{6t\Omega} = 0.8$. At these energies, keeping only the

2.3. Polaron near a single impurity

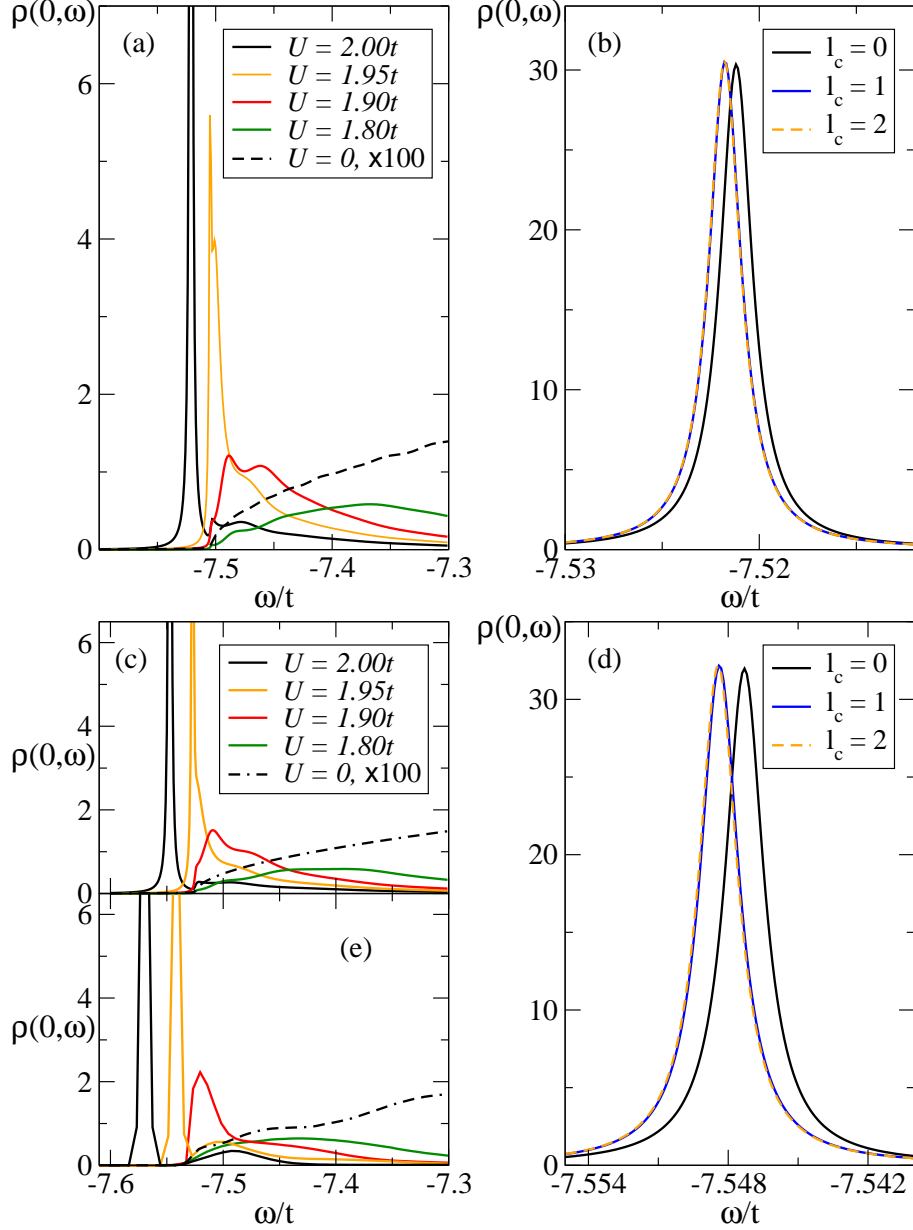


Figure 2.3: LDOS at the impurity site $\rho(0, \omega)$ in units of $1/t$, vs. the energy ω/t , for (a) MA^0 with $l_c = 0$ for $U = 1.8, 1.9, 1.95$ and 2.0 . The dashed line shows the DOS for the clean system, times 100; (b) Bound polaron peak in MA^0 at $U/t = 2$, and cutoffs in the renormalized potential $l_c = 0, 1, 2$. Panels (c) and (d) are the same as (a) and (b), respectively, but using MA^1 . Panel (e) shows the DMC results from Ref. [4], for the same parameters as (a) and (b). Other parameters are $\Omega = 2t, \lambda = 0.8, \eta/t = 10^{-3}$. 24

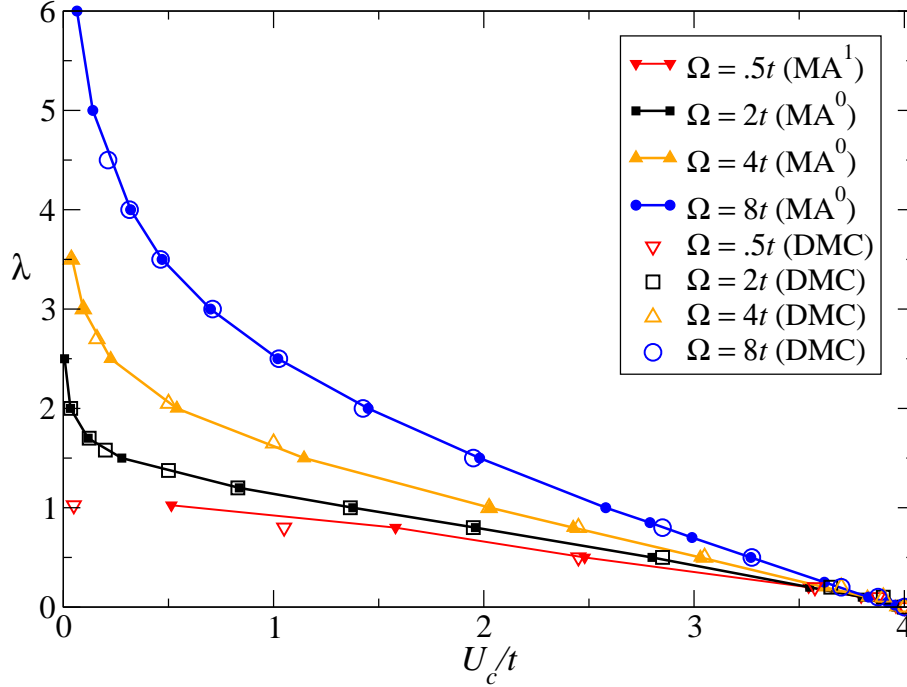


Figure 2.4: Phase diagram separating the regime where the polaron is mobile (below the line) and trapped (above the line). The effective coupling is $\lambda = g^2/(6t\Omega)$, and the threshold trapping potential U_c is shown for several values of Ω/t . The MA results (filled symbols) compare well with the DMC results of Ref. [4] (empty symbols).

local part in MA⁰, i.e. setting $v_0(l, \omega) \rightarrow \delta_{l,0}v_0(0, \omega)$, is already a very good approximation. Including the correction from the 6 nearest neighbor sites ($l_c = 1$) lowers the energy somewhat, but the contribution from the second nearest neighbor sites ($l_c = 2$) is no longer visible on this scale in either the MA⁰ or MA¹ level.

By repeating this process for different values of the parameters we can trace U_c in the parameter space. This is shown in Fig. 2.4, for $\Omega/t = 0.5, 2, 4, 8$ and various effective couplings. The MA results (filled symbols) are in good quantitative agreement with the DMC results (empty symbols) for larger values of phonon frequency, $\Omega \geq t$. Shown here are MA⁰ results for cutoff $l_c = 0$. Using MA¹ and/or increasing the cutoff changes the values of U_c by less than 1% everywhere we checked. For the smaller frequencies such as $\Omega = 0.5t$, MA is known to become quantitatively less accurate

2.3. Polaron near a single impurity

at intermediary couplings [14, 50], and indeed, here we see a discrepancy with the DMC data even for the MA¹ results. To improve the quantitative agreement here, one should use a 2- or 3-site MA variational approximation for the phonon cloud, as discussed in Ref. [55].

As expected, U_c approaches the threshold value for a bare particle for $\lambda \rightarrow 0$ which is roughly $3.96t$. U_c decreases for stronger effective couplings, but the lines never intersect the λ -axis: $U_c = 0$ is impossible, since the polaron cannot be trapped (localized) in a clean system, although it can have an extremely heavy effective mass when λ is strong. This is also the reason why U_c decreases with increasing λ : a heavier quasiparticle is easier to trap by the impurity [4]. However, we claim that this is not the full story, and that the renormalization of the trapping potential also plays a non-trivial role, as detailed below.

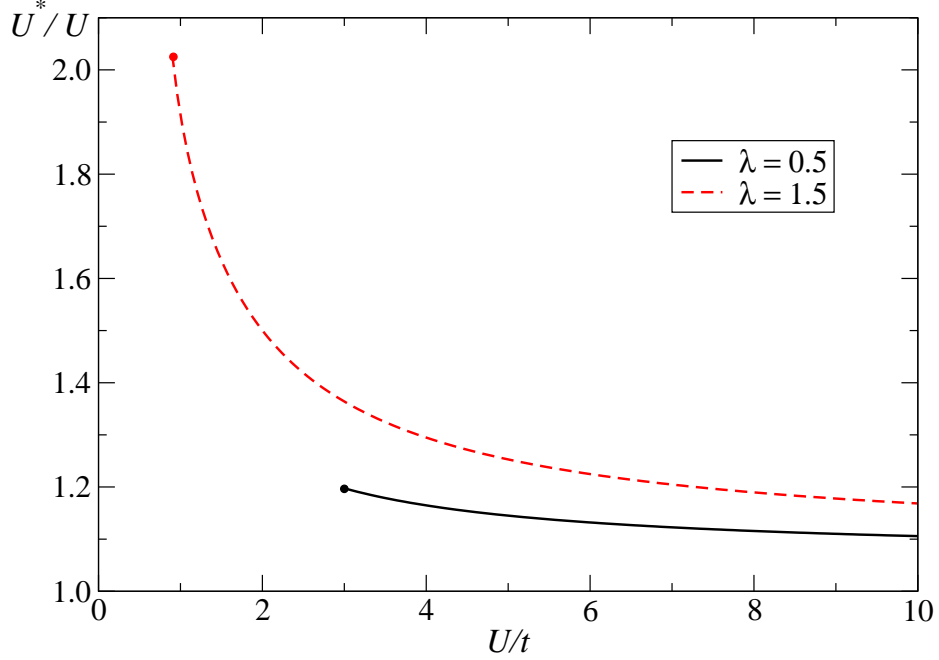


Figure 2.5: (color online) Effective value of the impurity attraction U^*/U , extracted from the scaling $E_B^*/t^* = f(U^*/t^*)$, for $\lambda = 0.5, 1.5$ and $\Omega = 3t$. In order to have the best fit to the data, we plot each curve starting from slightly larger U/t than the corresponding U_c/t given in Fig. (2.4). For more details, see text.

Consider Hamiltonian (2.16), which describes the impurity problem in

2.3. Polaron near a single impurity

the absence of electron-phonon coupling. The binding energy of the impurity state (once formed) is a monotonic function of the only dimensionless parameter of this problem, U/t : $\frac{E_B}{t} = f\left(\frac{U}{t}\right)$ for any $\frac{U}{t} \geq \frac{U_c}{t} \approx 3.96$. In the presence of electron-phonon coupling, if one views the polaron as a quasiparticle with an effective hopping t^* which scatters on the same impurity U as the bare particle (instantaneous approximation), then the polaron binding energy should be $\frac{E_B^*}{t^*} = f\left(\frac{U}{t^*}\right)$ for any $\frac{U}{t^*} \geq \frac{U_c}{t^*} \approx 3.96$. In particular, this predicts $U_c/t = 3.96t^*/t$ to decrease with increasing λ , in qualitative agreement with Fig. 2.4. This hypothesis can be tested. The function $f(x)$ is easy to calculate numerically; we can also extract the binding energy E_b^* for the trapped states by comparing their energy to the ground state energy of the polaron in the clean system, and the effective hopping $t^* \sim 1/m^*$ is directly linked to the effective polaron mass m^* in the clean system [14].

What we find is that such a scaling is not obeyed. Instead, one needs to also rescale the impurity potential, i.e. use $\frac{E_B^*}{t^*} = f\left(\frac{U^*}{t^*}\right)$ where $U^* \neq U$. Of course, this scaling assumes that the scattering potential is local. As we discussed, this is not true although it is a good approximation for medium and large couplings.

In Fig. 2.5 we show the renormalized value U^*/U extracted this way, as a function of U/t above the corresponding threshold values U_c/t , for a medium and a large effective coupling $\lambda = 0.5, 1.5$ and $\Omega = 3t$. Qualitatively similar curves are found for other parameters. We see that $U^* \rightarrow U$ only when $U \rightarrow \infty$ and becomes the dominant energy scale (hence anything else is a small perturbation). For fixed values of U and Ω , U^* is found to increase with increasing coupling λ – this is also expected, since the renormalization is directly caused by the electron-phonon coupling, see Fig. 2.2(b). This renormalization is a direct illustration of the general result of Eq. (2.15): the electron-phonon coupling changes not only the properties of the polaron (its effective mass), but also the effective disorder potential it experiences.

However, it is very wrong to expect that the potential renormalization can always be described by a simple rescaling by some overall value. Indeed, Eq. (2.15) shows that the renormalized potential is expected to be a function of energy, because of retardation effects. This function is not roughly constant, instead it has significant and very non-trivial dependence on ω , as illustrated by plotting $v_0(0, \omega)$ over a wide energy range, in Fig. 2.6. Similar curves are found for other values of the parameters. Over a narrow range of energies around $\omega \sim -7.5t$ where the bound state forms for these parameters (see Fig. 2.3), $v_0(0, \omega)$ varies slowly and can be approximated as an overall negative constant. This explains why here we can approximate

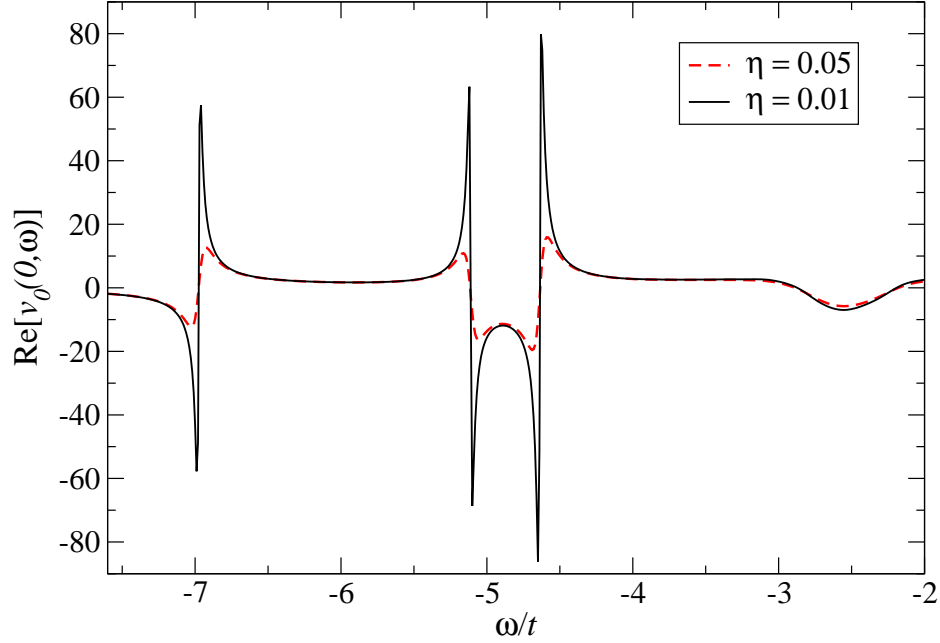


Figure 2.6: (color online) Real part of the additional on-site MA^0 disorder potential $v_0(0, \omega)$ over a wide energy range, for $U = 2t, \Omega = 2t, \lambda = 0.8$ and two values of η .

$\epsilon_0^*(\omega) = -U + v_0(0, \omega) \approx -U^*$, with $U^* > U$, as discussed above. At higher energies, however, $v_0(0, \omega)$ goes through singularities and changes sign from negative to positive and back. Although at first sight these singularities are surprising, they should be expected based on Eq. (2.12). The self-energy of the Holstein polaron is known to have such singularities, especially at medium and higher couplings where an additional second bound state forms and the continuum above shows strong resonances spaced by Ω [14]. In particular, as $\lambda \rightarrow \infty$ and the spectrum evolves towards the discrete Lang-Firsov limit $E_n = -\frac{g^2}{\Omega} + n\Omega$, the self-energy has a singularity at the top of each corresponding band. The renormalized potential of Eq. (2.12) is the difference between two such curves, displaced from each other. It is therefore not surprising that it has such nontrivial behavior.

Physically, such strong retardation effects are not surprising either, since the additional potential $v_0(i, \omega)$ describes the scattering of the electron in the presence of the phonon cloud. The structure of the phonon cloud varies with energy; for instance, one expects quite different clouds at low energies

2.3. Polaron near a single impurity

within the polaron band vs at higher energies, where there is a continuum of incoherent states with finite lifetimes. This suggests that the diagrams of Fig. 2.2(b) that contribute most to the series change with energy, and so does the total result. As a final note, we mention that at these higher energies, MA¹ should be used. It is well-known that MA⁰ fails to describe properly the location of the polaron+one phonon continuum, since it does not include the corresponding variational states [51]. This problem is fixed at the MA¹ and higher levels [50].

To summarize, the MA approximation is found to agree well with results from DMC in describing the trapping of Holstein polaron near a single attractive impurity. Although it is not quantitatively as accurate as DMC, besides efficiency its main advantage is that the analytic equations that describe MA allow us to understand the relevant physics. In particular, we showed that coupling to bosons renormalizes the disorder in a very non-trivial way.

2.3.2 Impurity changing the electron-phonon coupling

We now assume that the impurity does not change the on-site energy, but instead it modifies the value of electron-phonon coupling at its site

$$\mathcal{H} = \hat{T} + \Omega \sum_j b_j^\dagger b_j + \sum_j g_j c_j^\dagger c_j (b_j + b_j^\dagger), \quad (2.21)$$

where $g_j = g + (g_d - g)\delta_{j,0}$. Thus, g_d and g are the electron-phonon couplings at the impurity site and in the bulk of the system, respectively. Since $\hat{V}_d = 0$ in this case, the non-interacting part of the Hamiltonian is $\mathcal{H}_d = \mathcal{H}_0$. Thus, $G_{jj}^d(\omega - n\Omega) \rightarrow G_{jj}^0(\omega - n\Omega) \equiv g_0(\omega - n\Omega)$ in the continued fractions, Eq. (2.8), whose dependance on the site index j is now through the coupling g_j only. As a result, the effective disorder potential $v_0(j, \omega)$ vanishes everywhere except at the impurity site, $j = 0$:

$$v_0(j, \omega) \equiv \Delta(\omega)\delta_{j,0}, \quad (2.22)$$

where $\Delta(\omega) = g_d A_1(0, \omega) - g A_1(\omega)$, and $A_1(0, \omega)$ is like in Eq. (2.11) but with $g \rightarrow g_d$. This shows that even though $\epsilon_i = 0$ in this case, the inhomogeneity gives rise to an effective potential $\epsilon_i^*(\omega) = \delta_{i,0}\Delta(\omega)$. This is now local because only when the particle is at the impurity site it can experience a different coupling. Equation (2.13) can now be solved analytically to give

$$\rho(0, \omega) = -\frac{1}{\pi} \text{Im} \left(\frac{g_0(\tilde{\omega})}{1 - \Delta(\omega)g_0(\tilde{\omega})} \right). \quad (2.23)$$

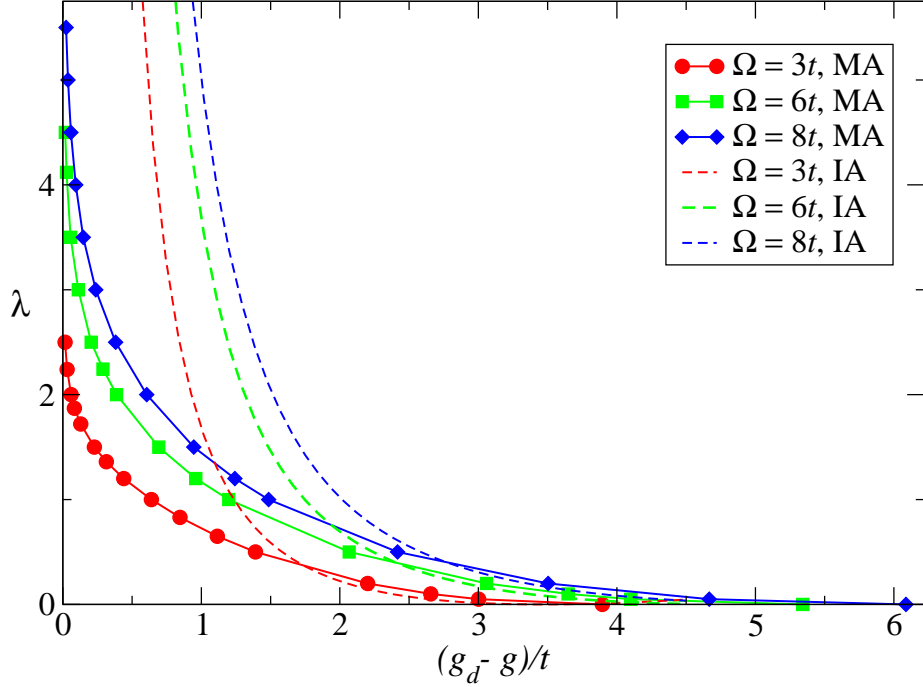


Figure 2.7: (color online) Phase diagram separating the regime where the polaron is delocalized (below the line) and trapped (above the line), as a function of the difference between the impurity and the bulk electron-phonon coupling, $g_d - g$. Symbols show MA^0 results, while the dashed lines correspond to the instantaneous approximation.

We can now find the values of $g_d - g$ for an impurity state to emerge below the continuum, for given values of g and Ω . The results are shown in Fig. 2.7 for $g_d > g$, when the polaron formation energy at the impurity site, $-g_d^2/\Omega$, is lower than the bulk value $-g^2/\Omega$, and a bound state may be expected to form even within the instantaneous approximation. Symbols show MA^0 results, while the dashed lines are for the instantaneous approximation (DMC results are not available for this case). The two agree quantitatively only in the limit $\lambda \rightarrow 0$. This proves that the additional renormalization included in MA is significant for this type of impurity, as well. We note that all critical lines intercept the x -axis at a finite value, i.e. for any value of Ω and $g = 0$, there is a critical finite value g_d above which an impurity state forms. For example, for $\Omega = 3t$ this critical value is $g_d \approx 3.9t$ and it increases with growing Ω , as expected.

2.3. Polaron near a single impurity

Unlike for an impurity which changes the on-site potential, and which can bind at most one impurity state, impurities which change the electron-phonon coupling can bind multiple impurity levels. As g_d increases and the energy of the impurity level moves towards lower energies, additional bound states, spaced by roughly Ω , emerge whenever the distance between the last one and the bulk polaron band is of order Ω . The origin of this sequence of bound states is straightforward to understand in the limit $g_d \gg g, t$, where the dominant term in the Hamiltonian is

$$\mathcal{H} \approx g_d c_0^\dagger c_0 (b_0^\dagger + b_0) + \Omega b_0^\dagger b_0,$$

with $c_0^\dagger c_0 \approx 1$ as the weight of the bound state is concentrated at the impurity site. This Hamiltonian can be exactly diagonalized using the Lang-Firsov transformation [15]. Using new operators $B_0 = b_0 + \alpha$, where α is a real number, this Hamiltonian can be written as

$$\mathcal{H} = \Omega B_0^\dagger B_0 + (g_d - \alpha\Omega)(B_0^\dagger + B_0) + \alpha^2\Omega - 2\alpha g_d.$$

Choosing $\alpha = g_d/\Omega$ diagonalizes this Hamiltonian, resulting in a series of equally spaced eigenenergies $E_n = n\Omega - g_d^2/\Omega$. For finite g_d , all states which lie below the bulk polaron continuum become impurity states, and basically describe excited bound states with additional phonons at the impurity site.

So far we have considered $g_d > g$, where a ground-state impurity level can emerge. It is important to note that discrete peaks can also appear for $g_d < g$, although not at low energies. This happens when λ is sufficiently large that there is a gap between the bulk polaron band and higher features in the spectrum, such as the polaron+one phonon continuum, or the band associated with the second bound state, once it forms [56]. A typical example is shown in Fig. 2.8, where in the presence of an impurity with a weaker coupling $g_d < g$ (full line), a discrete state appears above the polaron band. Since most of its weight is removed from the bulk polaron band (dashed line), we interpret this as being an ‘‘anti-bound’’ polaron state. A similar state is also expected to appear for a repulsive on-site $U < 0$ potential.

2.3.3 Isotope impurity

The last case we consider is an isotope impurity. Because of the different mass of an isotope substitution, $M_d \neq M$, its phonon frequency $\Omega_d \sim M_d^{-1/2}$ as well as electron-phonon coupling $g_d \propto 1/\sqrt{M_d\Omega_d} \sim M_d^{-1/4}$ are different. Interestingly, both the effective coupling $\lambda_d = g_d^2/(6t\Omega_d) = g^2/(6t\Omega) = \lambda$ and the polaron formation energy $-g_d^2/\Omega_d = -g^2/\Omega$ show no isotope effect

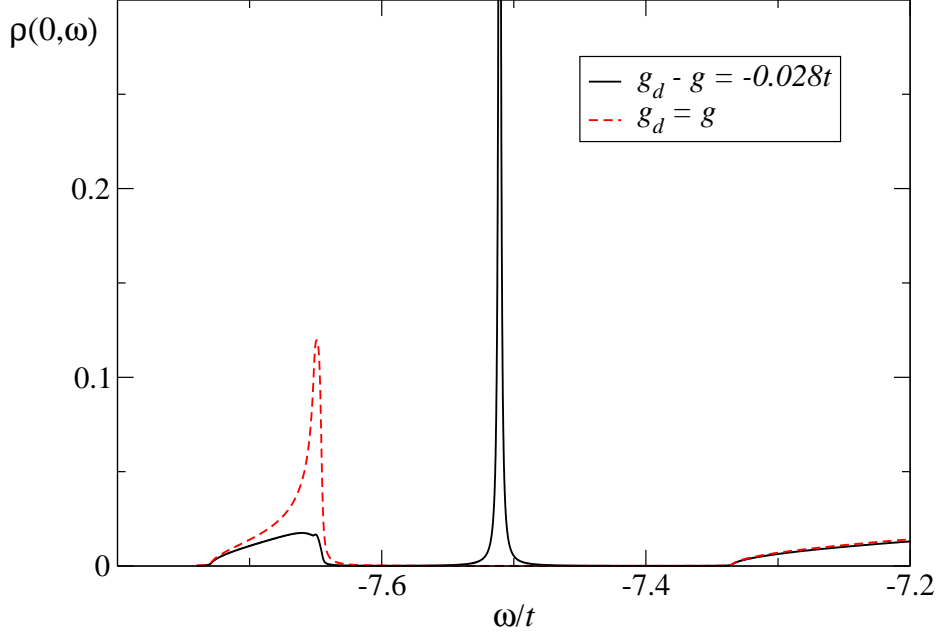


Figure 2.8: For large λ , in the clean system (dashed red line) the first polaron band is separated by an energy gap from the next features in the spectrum (here, the band associated with the second bound state). For $g_d < g$, an “anti-bound” impurity state is pushed inside this gap (black full line). Parameters are $\Omega = t = 1$, $\lambda = 1.2$ and $\eta = 10^{-3}$.

[57]. As a result, within the instantaneous approximation of Eq. (2.14) one would predict that the isotope is “invisible” and the polaron spectrum is basically unaffected by its presence.

We consider a single isotope impurity located at the origin

$$\mathcal{H} = \hat{T} + \sum_j g_j c_j^\dagger c_j (b_j + b_j^\dagger) + \sum_j \Omega_j b_j^\dagger b_j, \quad (2.24)$$

where $\Omega_j = \Omega + (\Omega_d - \Omega)\delta_{j,0}$ and $g_j = g + (g_d - g)\delta_{j,0}$ are chosen such that $\lambda_d = \lambda$. Just like in the previous section, because there is no on-site disorder $\epsilon_i = 0$, $G_{jj}^d(\omega) = G_{jj}^0(\omega)$ and the effective disorder potential is again local, i.e. it vanishes everywhere other than the impurity site. As a result, the LDOS at the impurity site is given by Eq. (2.23), except that here

$$\Delta(\omega) = \Sigma_d(\omega) - \Sigma_{\text{MA}^0}(\omega), \quad (2.25)$$

2.3. Polaron near a single impurity

where $\Sigma_d(\omega)$ has the same functional form as $\Sigma_{\text{MA}^0}(\omega)$, but with $g \rightarrow g_d$ and $\Omega \rightarrow \Omega_d$.

By investigating this LDOS for different values of parameters we find that there exists a threshold value of the effective coupling, λ^* , below which low-energy bound states do not form irrespective of how small or large M_d/M is. In other words, for $\lambda < \lambda^*$ the behavior agrees with the prediction of the instantaneous approximation.

We can estimate λ^* as follows. Consider the case of a very light isotope, so that $\Omega_d, g_d \gg \Omega, g, t$. In this limit, $\Sigma_d(\omega) \rightarrow -g_d^2/\Omega_d = -6t\lambda$. The bound state appears when the LDOS is singular as its denominator vanishes

$$1 - \Delta(\omega)g_0(\tilde{\omega}) = 0 \rightarrow \Sigma_{\text{MA}^0}(\omega) + 1/g_0(\tilde{\omega}) = -6t\lambda, \quad (2.26)$$

where Eq. (2.25) and $\Sigma_d(\omega) \approx -6t\lambda$ are used.

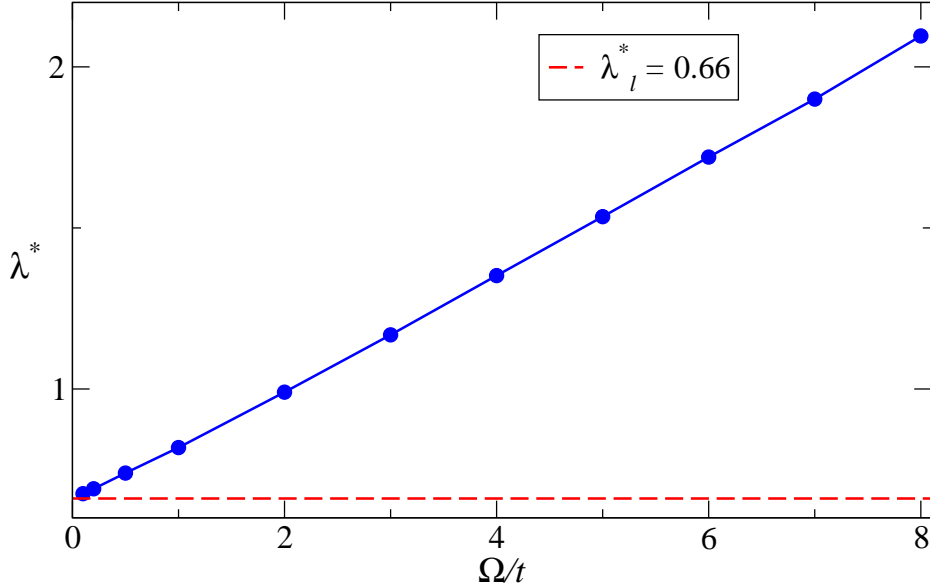


Figure 2.9: (color online) Critical effective coupling λ^* above which an impurity state may appear for a sufficiently light isotope. Below this line, polarons cannot be bound near isotopes. Symbols shows MA^0 results. The dashed line is the analytic low-bound for λ^* discussed in the text.

Consider now the limiting case when a bound state emerges just below the bulk polaron ground state, i.e. Eq. (2.26) has a solution at $\omega \leq E_{GS}$. In the clean system, the polaron ground state energy E_{GS} is the lowest pole

2.3. Polaron near a single impurity

of $G(\mathbf{k} = \mathbf{0}, \omega) = [\omega - \varepsilon(\mathbf{k} = \mathbf{0}) - \Sigma_{\text{MA}^0}(\omega)]^{-1}$, so it satisfies:

$$E_{GS} = -6t + \Sigma_{\text{MA}^0}(E_{GS}).$$

Using this in Eq. (2.26) suggests that a solution can exist if $\lambda > \lambda^*$, where

$$\lambda^* = \left| \frac{E_{GS}}{6t} \right| - 1 - \frac{1}{6tg_0(-6t)}, \quad (2.27)$$

in which $g_0(-6t) \approx -1/3.96t$ for 3D tight-binding model. Since $E_{GS} \rightarrow -6t$ as $\lambda \rightarrow 0$, we find that $\lambda^* \rightarrow 0.66$ in this limit, and that it increases as E_{GS} becomes more negative, for example with increasing λ . These considerations are confirmed by the data shown in Fig. 2.9. Here, the symbols show values of λ^* found numerically with MA^0 , and the dashed line is the lower bound of 0.66, discussed above.

For $\lambda > \lambda^*$, bound impurity states can appear near isotopes if g_d and $\Omega_d = g_d^2/(6t\lambda)$ are sufficiently large. In Fig. 2.10 we show critical lines for two cases, $\Omega = 4t, 8t$. The symbols show the MA^0 results, which converge towards their corresponding λ^* values as $\Omega_d \rightarrow \infty$, as expected. Of course, the largest values considered for Ω_d are unphysical; we use them only to illustrate the convergence towards λ^* .

The existence of a region of the parameter space where bound polaron states appear near an isotope is in direct contradiction of the instantaneous approximation, and again illustrates the importance of the renormalized disorder potential $\Delta(\omega)$ which makes their trapping possible. In this context, it is worth mentioning that there is clear evidence for electronic states bound near isotope O^{16} defects in CuO_2 planes [58], although the precise nature of these states has not been clarified and the measurements are certainly not in the extremely underdoped regime where our single-polaron results are valid.

Interestingly, when such bound states form near an isotope, the spectrum is different than that for the other two types of impurities. As shown in Fig. 2.11, bound states now appear simultaneously both below and above the bulk polaron continuum, not just below it. This provides a possible ‘‘fingerprint’’ for polarons trapped near isotopes. Finally, we note that even when no low-energy impurity state is observed, it is again possible to have higher energy bound states inside the gaps opening between various features in the bulk polaron spectrum.

To summarize, in the presence of isotope defects, polarons in the weakly coupled regime $\lambda < \lambda^*$ always remain delocalized. Only for $\lambda > \lambda^*$ it is possible to trap polarons near an isotope. This makes the isotope substitution quite distinct from the other two cases, where bound states exist for any λ if the impurity is strong enough.

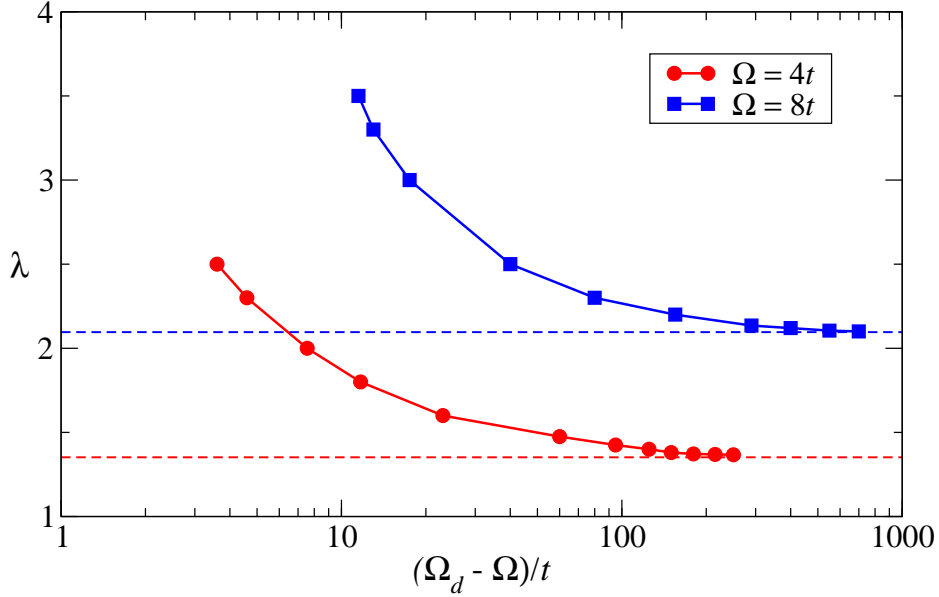


Figure 2.10: Phase diagram separating the regime where the polaron is delocalized (below the line) and trapped (above the line), as a function of the difference between the $\Omega_d - \Omega$, on a logarithmic scale. Symbols show MA⁰ results for $\Omega = 4t, 8t$. As $\Omega_d \rightarrow \infty$, these critical lines converge towards their corresponding λ^* (dashed lines), below which polaron states are always delocalized.

2.4 Summary and conclusions

We studied the threshold for the emergence of polaron bound states near various types of single impurities, using the momentum-average approximation. Electron-phonon coupling was shown to strongly renormalize the impurity potential in a nontrivial way which includes strong retardation effects. This is a feature that is completely absent in the instantaneous approximation, which is the only other available “simple” description of this problem.

We considered the simplest models of impurities that change the strength of the on-site energy, the local electron-phonon coupling, or are isotope substitutions that modify both the coupling and the phonon energy. We calculated the polaron binding phase diagrams for each case. The first case had been considered previously by numerical methods [4, 46], and our results are in good quantitative agreement with their predictions. To our knowledge, the other two cases have not been investigated before. We showed that in the

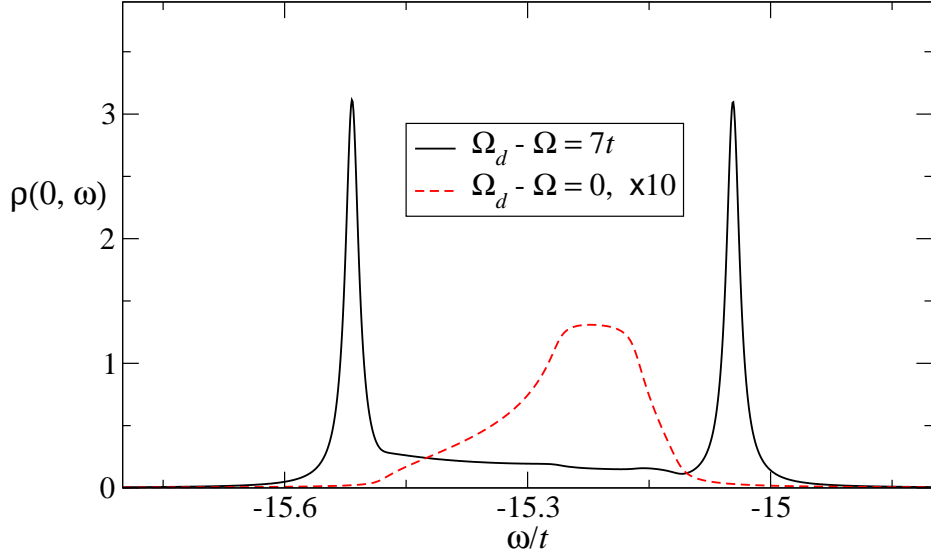


Figure 2.11: LDOS at the impurity site near an isotope with $\Omega_d = \Omega + 7t$ (full line). Two discrete states, one above and one below the bulk polaron band, are seen. For comparison, the DOS in the clean system (multiplied by 10) is shown as a dashed line. Parameters are $\Omega = 4t$, $\lambda = 2.5$ and $\eta = 10^{-2}$.

first two cases bound states always exist for a sufficiently strong impurity, however the polaron remains delocalized for the case of isotope substitution of arbitrary strength if the effective coupling is weaker than a threshold value, λ^* . Differences in the LDOS at the impurity site have also been found, such as the possibility to bind multiple states near an impurity that changes the coupling, or the unusual fingerprint of discrete states both below and above the bulk polaron continuum, for an isotope bound state.

Of course, a realistic description of an impurity in a real system may combine several of these inhomogeneities, and even the form of the electron-phonon coupling could be affected. MA gives an efficient yet quite accurate way to deal with such cases, and can be easily generalized to other types of couplings where MA has been used successfully to describe bulk properties.

Whereas we expect the single impurity results to remain valid for a system with multiple impurities if the mean free path is long and the polaron interacts with one impurity at a time, in the presence of significant disorder, when multiple scattering processes become important, the polarons can undergo Anderson localization. This limit has been addressed within a generalized DMFT approach [42], however we believe that our simpler

2.4. *Summary and conclusions*

formulation might provided additional insight and uncover previously unexplored aspects of Anderson localization for polarons. The opposite limit of weak (and extended) disorder is discussed in the next chapter.

Chapter 3

A perturbational study of the lifetime of a Holstein polaron in the presence of weak disorder

3.1 Introduction

Studying the behavior of solid state systems under the simultaneous action of disorder and interactions is a significant challenge in condensed matter physics. Strong correlations in interacting systems often give rise to sharp quasiparticles. Scattering of such quasiparticles from weak disorder should just limit their lifetime. For strong disorder and no interactions, it is well understood [59] that constructive interference of the backscattered waves can localize single particles such that they lose their itinerancy. If interactions are turned on, there is no consensus about the effect of disorder on the quasiparticles of interacting systems.

In chapter 1 I studied the bound state of a Holstein polaron around single impurities of arbitrary strength. For the case where disorder is extended all over the lattice, if one views the polaron as a particle with a renormalized mass, strong disorder should result in Anderson localization. However, phonon-assisted hopping of carriers between localized states is well established as a conduction process in lightly doped semiconductors [60]. This suggests that, for suitable electron-phonon couplings, polarons may still be itinerant in a disorder potential that would localize particles with the same effective mass. A possible explanation for this was offered in the first chapter, where the momentum average (MA) approximation was used to show that the electron-phonon coupling renormalizes the disorder potential in a strongly energy-dependent manner, so that the effective disorder seen by polarons can be drastically different from the bare disorder.

A possible approach for studying this problem, valid for weak disorder,

is to use perturbation theory and perform the disorder average analytically, similarly to the Born approximation widely employed for charge carriers in the absence of electron-phonon coupling [61]. Because localization cannot be described within a perturbational calculation, the polaron eigenstates remain extended and self-averaging over all disorder realizations is appropriate.

In this chapter, I follow this approach and calculate, using MA and for weak disorder, the disorder-averaged Green's function of the Holstein polaron and the resulting polaron lifetime and energy shift. Because here we focus only on the lowest-energy polaron states, which are already accurately described at the MA⁰ level, in the following we restrict ourselves to this flavor and call it MA for simplicity.

The chapter is organized as follows. In Sec. 3.2, I present the generalization of MA to include disorder perturbationally. Sec. 3.3 contains the results and their analysis, and Sec. 3.4 is for conclusion. Some of the computational details are given in appendixes.

3.2 The model and its solution

We start again with the Hamiltonian for a Holstein polaron in a lattice with random on-site energies

$$\mathcal{H} = \mathcal{H}_d + \hat{V}_{\text{el-ph}} = \mathcal{H}_0 + \hat{V}_d + \hat{V}_{\text{el-ph}}, \quad (3.1)$$

where the non-interacting part of the Hamiltonian, \mathcal{H}_d , is divided into $\hat{V}_d = \sum_i \epsilon_i c_i^\dagger c_i$, describing the on-site disorder potential experienced by the charge carrier, and

$$\mathcal{H}_0 = -t \sum_{\langle i,j \rangle} (c_i^\dagger c_j + \text{H.c.}) + \Omega \sum_i b_i^\dagger b_i \quad (3.2)$$

describing the kinetic energy of charge carrier plus the (optical) phonon energies ($\hbar = 1$). The interaction term

$$\hat{V}_{\text{el-ph}} = g \sum_i c_i^\dagger c_i (b_i^\dagger + b_i) \quad (3.3)$$

describes the Holstein coupling between a single charge carrier and phonons. c_i and b_i are annihilation operators for the charge carrier and phonons, respectively, in a simple cubic lattice whose sites are indexed by i . The spin of the carrier is irrelevant and is therefore ignored.

3.2. The model and its solution

The on-site energies, $\{\epsilon_i\}$, are taken from an uncorrelated symmetric random distribution

$$\mathcal{P}(\{\epsilon_i\}) = \prod_i \mathcal{P}(\epsilon_i). \quad (3.4)$$

For Anderson disorder, $\mathcal{P}(\epsilon_i)$ is the completely random, flat distribution

$$\mathcal{P}(\epsilon_i) = \begin{cases} 1/(2\Delta) & \text{if } -\Delta \leq \epsilon_i \leq \Delta \\ 0 & \text{otherwise,} \end{cases} \quad (3.5)$$

where Δ can be thought of as the strength of disorder. For a binary alloy, $\mathcal{P}(\epsilon_i) = x\delta(\epsilon_i - \epsilon_A) + (1-x)\delta(\epsilon_i - \epsilon_B)$, with x being the concentration of A-type atoms and energies are shifted so that $x\epsilon_A + (1-x)\epsilon_B = 0$.

Our aim is to calculate the single polaron Green's function (GF) of this problem and average it analytically over all disorder configurations given by Eq. (3.4) and (3.5). From now on, we use an overbar to denote disorder-averaged quantities. The strength of disorder, $\sigma \equiv (\overline{\epsilon_i^2})^{1/2}$, is taken to be weak compared to polaron bandwidth in the clean system, so that it can be treated perturbationally. As a result, the polaronic picture remains valid but its lifetime is expected to become finite due to scattering from the disorder potential \hat{V}_d .

Since \hat{V}_d is weak compared to other terms in the Hamiltonian, we treat it as a perturbation. Dividing the Hamiltonian as $\mathcal{H} = \mathcal{H}_H + \hat{V}_d$, where \mathcal{H}_H is the Hamiltonian of the Holstein polaron in the clean lattice, we use Dyson's identity, $\hat{G}(\omega) = \hat{G}_H(\omega) + \hat{G}(\omega)\hat{V}_d\hat{G}_H(\omega)$, to relate $\hat{G}(\omega)$ of the system with disorder to that of the clean system, $\hat{G}_H(\omega)$. To the second order in \hat{V}_d , we find

$$\begin{aligned} \hat{G}(\omega) \approx & \hat{G}_H(\omega) + \hat{G}_H(\omega)\hat{V}_d\hat{G}_H(\omega) \\ & + \hat{G}_H(\omega)\hat{V}_d\hat{G}_H(\omega)\hat{V}_d\hat{G}_H(\omega). \end{aligned} \quad (3.6)$$

Because disorder breaks translational invariance, the eigenstates for any single disorder realization are not labelled by the lattice momentum \mathbf{k} . However, averaging over all disorder configurations restores the translational invariance and makes \mathbf{k} a good quantum number again. As a result, $\overline{\langle 0|c_{\mathbf{k}}\hat{G}(\omega)c_{\mathbf{k}'}^\dagger|0\rangle} = \delta_{\mathbf{k},\mathbf{k}'}\bar{G}(\mathbf{k},\omega)$ and we only need to calculate the diagonal matrix element

$$\begin{aligned} \bar{G}(\mathbf{k},\omega) = & G_H(\mathbf{k},\omega) + \sum_i \bar{\epsilon}_i \langle 0|c_{\mathbf{k}}\hat{G}_H(\omega)c_i^\dagger c_i \hat{G}_H(\omega)c_{\mathbf{k}}^\dagger|0\rangle \\ & + \sum_{i,j} \overline{\epsilon_i \epsilon_j} \langle 0|c_{\mathbf{k}}\hat{G}_H(\omega)c_i^\dagger c_i \hat{G}_H(\omega)c_j^\dagger c_j \hat{G}_H(\omega)c_{\mathbf{k}}^\dagger|0\rangle. \end{aligned} \quad (3.7)$$

3.2. The model and its solution

Here, $G_{\text{H}}(\mathbf{k}, \omega) = \langle 0 | c_{\mathbf{k}} \hat{G}_{\text{H}}(\omega) c_{\mathbf{k}}^{\dagger} | 0 \rangle$ is the polaron GF in the clean system:

$$G_{\text{H}}(\mathbf{k}, \omega) = \frac{1}{\omega - \varepsilon(\mathbf{k}) - \Sigma_{\text{MA}}(\omega) + i\eta} \quad (3.8)$$

where $\varepsilon(\mathbf{k}) = -2t \sum_i \cos(k_i)$. For completeness, its MA solution is briefly reviewed in Appendix A.

Since $\bar{\varepsilon}_i = 0$ for symmetrically distributed disorder, the first-order contribution vanishes³. Furthermore, because the disorder is uncorrelated, $\overline{\varepsilon_i \varepsilon_j} = \bar{\varepsilon}_i^2 \delta_{ij} \equiv \sigma^2 \delta_{ij}$ and the disorder-averaged GF becomes

$$\bar{G}(\mathbf{k}, \omega) - G_{\text{H}}(\mathbf{k}, \omega) = \sigma^2 \sum_i \langle 0 | c_{\mathbf{k}} \hat{G}_{\text{H}}(\omega) c_i^{\dagger} c_i \hat{G}_{\text{H}}(\omega) c_i^{\dagger} c_i \hat{G}_{\text{H}}(\omega) c_{\mathbf{k}}^{\dagger} | 0 \rangle. \quad (3.9)$$

The challenge is to use MA to calculate the matrix elements appearing in the sum. We do this to the same level of accuracy as $G_{\text{H}}(\mathbf{k}, \omega)$ is evaluated [48].

These matrix elements can be broken into products of generalized GF by inserting identity operators, \mathcal{I} , between the creation and annihilation operators. Since the MA flavor we use here is equivalent with assuming that the phonon cloud only extends over one site [48], at this level of accuracy it suffices to truncate $\mathcal{I} \approx \sum_{l,n} (1/n!) b_l^{\dagger n} | 0 \rangle \langle 0 | b_l^n$, i.e., to ignore states with phonons at two or more sites (such states can be added systematically in higher flavors of MA). Doing so results in

$$\begin{aligned} \bar{G}(\mathbf{k}, \omega) - G_{\text{H}}(\mathbf{k}, \omega) &= \sigma^2 \sum_{i,l,s,n,m} \frac{1}{n!m!} \langle 0 | c_{\mathbf{k}} \hat{G}_{\text{H}}(\omega) c_i^{\dagger} b_l^{\dagger n} | 0 \rangle \\ &\quad \times \langle 0 | b_l^n c_i \hat{G}_{\text{H}}(\omega) c_i^{\dagger} b_s^{\dagger m} | 0 \rangle \langle 0 | b_s^m c_i \hat{G}_{\text{H}}(\omega) c_{\mathbf{k}}^{\dagger} | 0 \rangle. \end{aligned}$$

This expression involves two different generalized propagators that we have to evaluate, namely $\langle 0 | c_{\mathbf{k}} \hat{G}_{\text{H}}(\omega) c_i^{\dagger} b_l^{\dagger n} | 0 \rangle$ and $\langle 0 | b_l^n c_i \hat{G}_{\text{H}}(\omega) c_i^{\dagger} b_s^{\dagger m} | 0 \rangle$.

First, as detailed in Appendix C, to the level of accuracy of MA⁰, for $n \geq 1$ both propagators vanish unless $i = l$. Therefore, we only have to evaluate $F_{\mathbf{k}i}^{(n)}(\omega) \equiv \langle 0 | c_{\mathbf{k}} \hat{G}_{\text{H}}(\omega) c_i^{\dagger} b_i^{\dagger n} | 0 \rangle$ for $n \geq 1$. Note that $F_{\mathbf{k}i}^{(0)}(\omega)$ is already known: $F_{\mathbf{k}i}^{(0)}(\omega) = \langle 0 | c_{\mathbf{k}} \hat{G}_{\text{H}}(\omega) c_i^{\dagger} | 0 \rangle = G_{\text{H}}(\mathbf{k}, \omega) \exp(-i\mathbf{k} \cdot \mathbf{R}_i) / \sqrt{N}$, where we have used $\langle 0 | c_{\mathbf{k}} \hat{G}_{\text{H}}(\omega) c_{\mathbf{k}}^{\dagger} | 0 \rangle = \delta_{\mathbf{k}\mathbf{k}'} G_{\text{H}}(\mathbf{k}, \omega)$. Here, $N \rightarrow \infty$ is the number of sites in the lattice. The details of the calculation for $n \geq 1$ are presented in Appendix C. The final result is

$$F_{\mathbf{k}i}^{(n)}(\omega) = \Gamma_n(\omega) F_{\mathbf{k}i}^{(0)}(\omega), \quad (3.10)$$

³A finite average can be removed trivially by an overall energy shift.

3.3. Results

where $\Gamma_n(\omega)$ are easy to calculate products of continued fractions.

Next, we calculate $W^{nm}(\omega) = \langle 0 | b_i^n c_i \hat{G}_H(\omega) c_i^\dagger b_i^{\dagger m} | 0 \rangle$. Note that because of the invariance to translations in the clean system, this quantity is actually independent of i . The detailed derivation of these functions is also presented in Appendix C.

With these expressions in hand, the disorder averaged GF, to second order in σ , becomes

$$\bar{G}(\mathbf{k}, \omega) = G_H(\mathbf{k}, \omega) + \sigma^2 [G_H(\mathbf{k}, \omega)]^2 \sum_{n,m=0}^{\infty} \frac{\Gamma_n(\omega) W^{nm}(\omega) \Gamma_m(\omega)}{n!m!}. \quad (3.11)$$

To the same order, this identifies the sum in Eq. 3.11 as the disorder self-energy in the presence of coupling to phonons,

$$\Sigma_{\text{dis}}(\omega) = \sigma^2 \sum_{n,m=0}^{\infty} \frac{\Gamma_n(\omega) W^{nm}(\omega) \Gamma_m(\omega)}{n!m!}. \quad (3.12)$$

This is our main result. From a computational point of view, because the factorials in the denominator grow rapidly with increasing index, the infinite sums can be safely truncated at finite values for n and m . Cutoffs of 20 proved sufficient for all cases we examined. Using $G_H(\mathbf{k}, \omega) = 1/(\omega - \varepsilon(\mathbf{k}) - \Sigma_{\text{MA}}(\omega) + i\eta)$ we can finally write

$$\bar{G}(\mathbf{k}, \omega) = \frac{1}{\omega - \varepsilon(\mathbf{k}) - \Sigma_{\text{tot}}(\omega) + i\eta}, \quad (3.13)$$

where the total self-energy is $\Sigma_{\text{tot}}(\omega) = \Sigma_{\text{MA}}(\omega) + \Sigma_{\text{dis}}(\omega)$. This implicit summation gives a more accurate expression for the disorder-averaged GF than Eq. (3.11), with which it agrees to $\mathcal{O}(\sigma^2)$.

3.3 Results

We are now prepared to study the effect of weak disorder on the polaron lifetime and energy. At this level of perturbation theory, disorder only enters through its standard deviation σ . In the following, we assume Anderson disorder of width 2Δ , for which $\sigma = \Delta/\sqrt{3}$. We will use either Δ or σ to characterize the disorder, as convenient, but we emphasize that any other type of disorder that has the same σ would lead to the same answer within this perturbational approximation. To characterize the electron-phonon coupling, it is convenient to use the effective coupling $\lambda = g^2/(6t\Omega)$.

3.3. Results

Once the GF is known, the energy broadening of an otherwise coherent polaron state of momentum \mathbf{k} , which is inversely proportional to its lifetime, is given by the width of the lowest peak in the spectral function, $\bar{A}(\mathbf{k}, \omega) = -\frac{1}{\pi} \text{Im} \bar{G}(\mathbf{k}, \omega)$. This broadening measures the rate at which the polaron leaves that momentum state due to scattering from the impurity potential \hat{V}_d . In a clean system, the polaron states below the phonon-emission threshold, $E_{GS} + \Omega$, are infinitely long lived, therefore the low-energy spectral weight is a Dirac delta function (in fact, a Lorentzian of width $\eta \rightarrow 0$). Mathematically, this is a consequence of the fact that (in the absence of disorder) the polaron self-energy $\Sigma_{\text{MA}}(\omega)$ has a vanishing imaginary part for all energies inside the polaron band.

Disorder-induced finite lifetime broadens the delta functions into almost Lorentzians. As a reference, we first review the case without electron-phonon coupling, $\lambda = 0$, for which the only nonzero term in Eq. (3.12) corresponds to $m = n = 0$. Therefore

$$\Sigma_{\text{dis}}(\omega) = \sigma^2 W^{00}(\omega) = \sigma^2 g_0(\omega), \quad (3.14)$$

where $g_0(\omega)$ is again the momentum-averaged single particle GF,

$$g_0(\omega) = \frac{1}{N} \sum_{\mathbf{k}} \frac{1}{\omega - \varepsilon(\mathbf{k}) + i\eta}. \quad (3.15)$$

The resulting spectral weight has a peak of width $\tau_{\mathbf{k}}^{-1}$ centred at energy $E_{\mathbf{k}}$ which is given by the pole condition

$$\omega - \varepsilon(\mathbf{k}) - \Sigma_{\text{dis}}(\omega) + i\eta = 0, \quad (3.16)$$

where $\omega = E_{\mathbf{k}} - i\tau_{\mathbf{k}}^{-1}$ and $\eta \rightarrow 0^+$.

Because $\tau_{\mathbf{k}}^{-1} \sim \sigma^2$ is small for weak disorder, we approximate $\Sigma_{\text{dis}}(\omega) \approx \Sigma_{\text{dis}}(E_{\mathbf{k}}) + \mathcal{O}(\sigma^4)$. Using this in Eq. (3.16) gives $E_{\mathbf{k}}$ and $\tau_{\mathbf{k}}^{-1}$ as follows [62]:

$$\begin{aligned} E_{\mathbf{k}} &= \varepsilon(\mathbf{k}) + \text{Re} \Sigma_{\text{dis}}(E_{\mathbf{k}}) \\ \tau_{\mathbf{k}}^{-1} &= -\text{Im} \Sigma_{\text{dis}}(E_{\mathbf{k}}). \end{aligned} \quad (3.17)$$

The first expression determines the energy shift compared to the electron energy in the clean system, $\varepsilon(\mathbf{k})$. Since $\text{Re}[g_0(\omega)]$ is negative for $\omega < 0$ and positive for $\omega > 0$, this implies that the energy band slightly widens up in the presence of disorder.

Using Eq. (3.14), the inverse lifetime becomes $\tau_{\mathbf{k}}^{-1} = -\sigma^2 \text{Im}[g_0(E_{\mathbf{k}})]$. However, $\text{Im}[g_0(E_{\mathbf{k}})]$ is proportional to the total density of states (DOS) for

the clean system,

$$\text{Im}[g_0(E_{\mathbf{k}})] = -\frac{\pi}{N} \sum_{\mathbf{k}'} \delta(E_{\mathbf{k}} - \varepsilon(\mathbf{k}')) = -\pi \rho_0(E_{\mathbf{k}}),$$

and therefore

$$\tau_{\mathbf{k}}^{-1} = \pi \sigma^2 \rho_0(E_{\mathbf{k}}) = \pi \sigma^2 \rho_0(\varepsilon(\mathbf{k})) + \mathcal{O}(\sigma^4). \quad (3.18)$$

This is simply Fermi's golden rule. Since the density of states vanishes outside the energy band of the clean system, $\varepsilon(\mathbf{k}) \in [-6t, 6t]$, this result predicts infinite lifetime for all states with $|E_{\mathbf{k}}| \geq 6t$, and finite lifetime for all states within the free particle band. We will return to this point later.

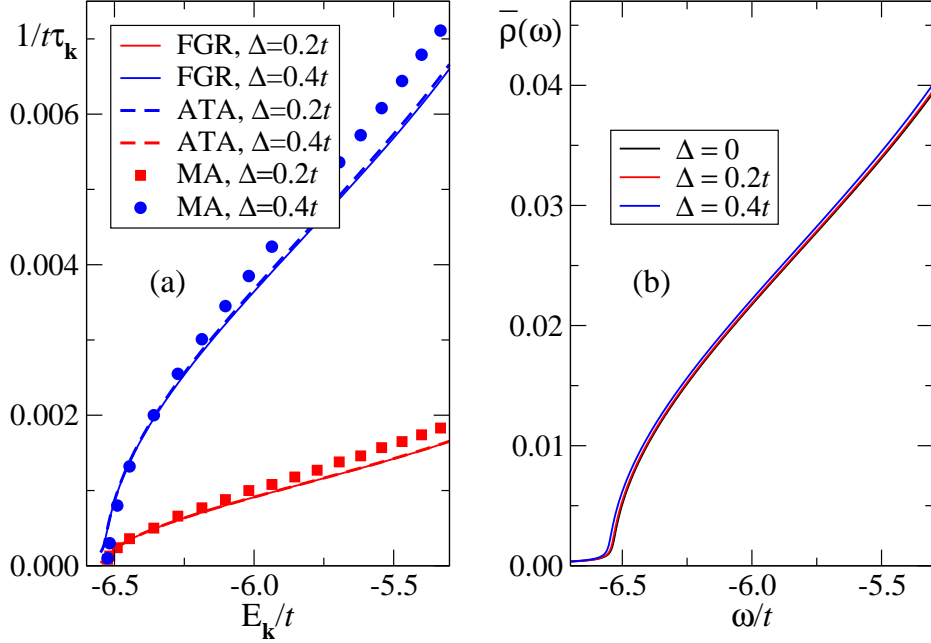


Figure 3.1: (a) Inverse polaron lifetime $1/\tau_{\mathbf{k}}$ vs its peak energy $E_{\mathbf{k}}$, and (b) average density of states $\bar{\rho}(\omega)$, for a weak electron-phonon coupling and two values of the disorder Δ . The solid and dashed lines are the corresponding Fermi golden rule (FGR) and ATA results, respectively (see text for more details). Other parameters are $\Omega = t, \eta/t = 10^{-2}$ in (a) and $\eta/t = 5 \times 10^{-3}$ in (b).

3.3.1 Weak electron-phonon coupling

The analysis is performed similarly in the presence of electron-phonon coupling, but then using the appropriate total self-energy, Eq. (3.13). We first consider weak electron-phonon coupling, $\lambda = 0.5$. In Fig. 3.1(a) we plot the polaron inverse lifetime for states in the lowest polaron band, for two different values of the disorder strength, $\Delta = 0.2t$ and $0.4t$ (squares and circles, respectively). These values are extracted from Lorentzian fits to the lowest peak in $\bar{A}(\mathbf{k}, \omega)$. The broadening η is decreased until $E_{\mathbf{k}}$ and $\tau_{\mathbf{k}}^{-1}$ converged to the values presented in Fig. (3.1) that are independent of η .

For this small λ , the MA ground state energy of the polaron in the clean system is $E_{GS} = -6.534t$. The weak disorder does not shift the eigenstates significantly. In fact, as shown in Fig. 3.1(b), the average density of states $\bar{\rho}(\omega) = -\frac{1}{\pi} \text{Im} \sum_{\mathbf{k}} \bar{G}(\mathbf{k}, \omega)$ is nearly identical to that of the clean system, although the band becomes slightly broader with increasing Δ . The inverse lifetime vanishes below the clean system band edge, E_{GS} , and it increases as $\sqrt{E_{\mathbf{k}} - E_{GS}}$ above, which is the expected DOS for the clean system at the bottom of the band. This is very similar to the $\lambda = 0$ result, except for the renormalization of the DOS by the electron-phonon interaction. Indeed, if we think of the polaron as a simple quasiparticle whose density of states is $\rho(\omega)$ [renormalized from $\rho_0(\omega)$ for a free electron], the inverse lifetimes we find at the bottom of the polaron band are in good agreement with those predicted by Fermi's golden rule (FGR), $\pi\sigma^2\rho(E_{\mathbf{k}})$ (see full lines).

While the agreement between the two is good near the bottom of the band, it becomes systematically worse at higher energies. To verify that this amount of disorder is still sufficiently small so that the disagreement is not due to using perturbational results outside their validity range, we also show average T-matrix (ATA) results (dashed lines). ATA is a simple way to treat disorder beyond the lowest order in perturbation theory, for a system with $\lambda = 0$. We briefly discuss it in Appendix D, as well as how we extend it for finite λ . ATA converges to $\pi\sigma^2\rho(\omega)$ in the limit of small σ , therefore the agreement between FGR and ATA confirms that the contribution of higher order terms in σ is indeed negligible. The disagreement with MA at higher energies is, therefore, not an artifact of using perturbation theory.

The meaning of this disagreement at higher energies should, however, be treated with some caution. It is well known [51, 63] that this flavor of MA fails to reproduce the correct polaron+one phonon continuum, which should start at $E_{GS} + \Omega$ (this problem is fixed by MA¹ and higher flavors). One consequence is that MA overestimates the bandwidth of the polaron at weak couplings. Indeed, in Fig. 3.1(a) we see that the polaron band extends

well past $E_{GS} + \Omega$. In other words, we know that at these higher energies MA is not accurate enough, so the results shown in Fig. 3.1 should only be trusted close to the bottom of the band, where the agreement is good.

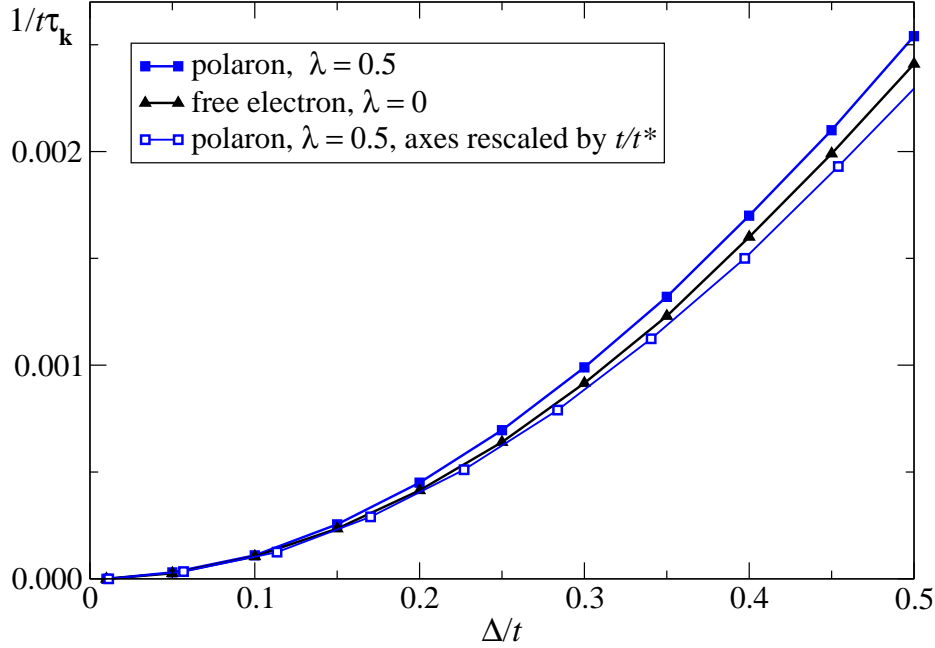


Figure 3.2: Inverse lifetime of the polaron of momentum $\mathbf{k} = (\pi/8, 0, 0)$ and $\lambda = 0.5$ vs the strength of disorder, Δ/t (full squares). The inverse lifetime for a free electron with the same momentum is shown by triangles. Empty squares show $1/(t^* \tau_{\mathbf{k}})$ vs Δ/t^* for the polaron (for this λ , $t^* = 0.881t$). Other parameters are $\Omega = t, \eta/t = 10^{-2}$.

The monotonic increase of the polaron's inverse lifetime with increasing disorder strength is shown in Fig. 3.2, for the lowest polaron state of momentum $\mathbf{k} = (\pi/8, 0, 0)$ and $\lambda = 0.5$ (full squares). For comparison, also shown is the corresponding lifetime of a bare electron ($\lambda = 0$, triangles) with the same momentum. Both curves show the expected $\propto \sigma^2$ increase predicted by Fermi's golden rule, but the polaron lifetime is somewhat shorter. The most likely reason for this is the renormalization of the polaron mass by electron-phonon coupling. Indeed, if instead we plot $1/(t^* \tau_{\mathbf{k}})$ vs Δ/t^* using the polaron lifetimes, the results are much closer to those of the free electron, especially for small values of the disorder (empty squares).

The conclusion, thus far, is that Fermi's golden rule agrees well with our

results at energies where this flavor of MA can be trusted. In other words, at weak electron-phonon coupling, the effect of disorder can be quantitatively understood if we think of the polaron as a simple particle with a renormalized mass (or DOS), and use Fermi's golden rule.

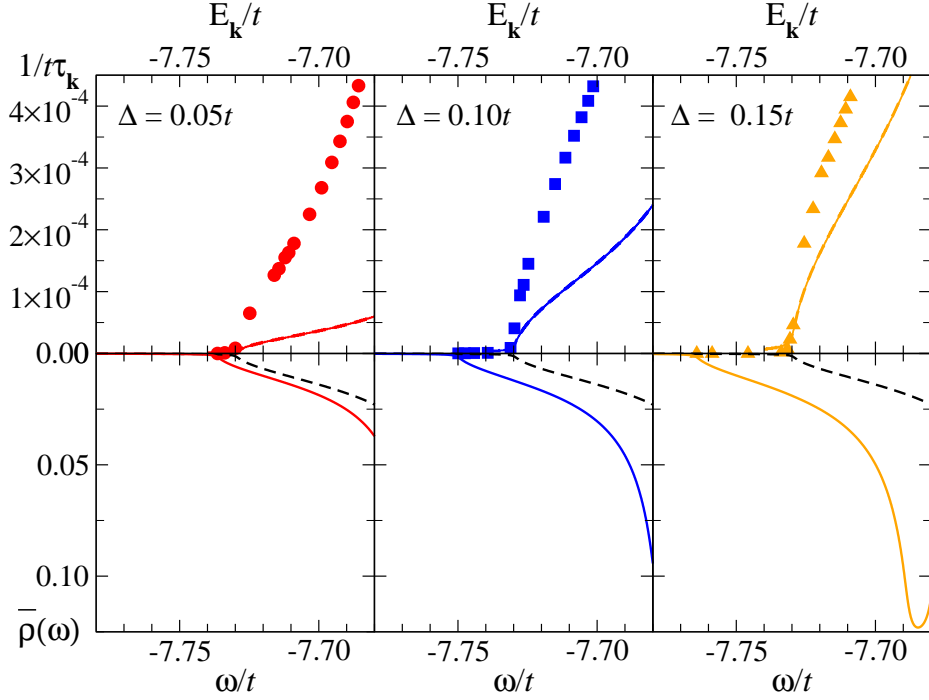


Figure 3.3: (Color online). Top panels: $1/(t\tau_{\mathbf{k}})$ vs $E_{\mathbf{k}}/t$ for three levels of disorder: $\Delta/t = 0.05, 0.1$ and 0.15 . The symbols shows the MA result for a strong coupling $\lambda = 1.2$, while the full and dashed lines show Fermi's golden rule and the ATA predictions, respectively. Bottom panels: The average DOS $\bar{\rho}(\omega)$ for that Δ (full line) and the DOS in the clean system, $\rho_{\text{H}}(\omega)$ (dashed line) vs ω . Parameters are $\Omega = t, \eta = 10^{-3}t$.

3.3.2 Strong electron-phonon coupling

We now check whether this also holds true at strong electron-phonon coupling. We use $\lambda = 1.2$ for which a robust small polaron appears in the clean system. The top panels in Fig. 3.3 show the polaron inverse lifetime vs. its energy for increasing strength of disorder (symbols), as well as Fermi's golden rule (full lines) and the ATA (dashed lines) predictions. The latter

3.3. Results

two are indistinguishable, confirming that these levels of disorder are indeed perturbationally small. The bottom panels show the average density of states, $\bar{\rho}(\omega)$ (full lines). For comparison, the polaron DOS in the absence of disorder, $\rho_{\text{H}}(\omega)$, is also shown (dashed line).

Let us first consider the DOS. As in the other cases we see that, by increasing disorder, the band edge shifts down to lower energies. However, the effect is quantitatively much more significant here compared to the weak coupling case, Fig. 3.1(b), because the polaron band is much narrower. This is seen in Fig. 3.4, where we show the same densities of states but over the whole polaron band. One surprise is that the entire band moves to lower energies with increasing disorder. This is different from what happens for a bare particle, where the band broadens symmetrically on both sides. The different behavior at the upper edge is likely due to the difference in their spectra. While for a single particle the energy band is the only feature in its spectrum, the spectrum of the polaron is quite complicated, with many other features, such as a band associated with the second bound state, the polaron+one-phonon continuum, etc., lying above the lowest polaron band [48]. With increasing disorder all these features should move toward lower energies. Level repulsion from these high energy states would explain why the upper edge of the polaron band moves to lower energies.

The inverse lifetime again vanishes for states whose energy lies below the band edge of the clean system, $E_{\mathbf{k}} < E_{GS} \approx -7.73t$. Because the shift of the disorder-averaged DOS is now significant, this means that, for a quite large energy range at the bottom of the band, the polaron has an infinite lifetime despite the presence of disorder. We emphasize that this is qualitatively similar to the result for a bare particle at the bottom of its band; it is simply more pronounced here. The meaning of this (un-physical) infinite lifetime for these low-energy states is discussed extensively below; briefly, we believe that it signals a failure of the perturbation theory at these energies. These low-energy states are most susceptible to localization, so the perturbational calculation and its predictions are not reliable here.

For high energy polaron states with $E_{\mathbf{k}} > E_{GS}$, the lifetime in the presence of disorder becomes finite, as expected. However, here the MA results disagree quantitatively with the FGR and ATA results at all energies. The latter two are nearly indistinguishable, suggesting again that these levels of disorder are small enough that perturbation theory should be valid. The disagreement cannot be blamed on MA, either: at such strong couplings and correspondingly low energies, MA is extremely accurate for the entire polaron band [14, 48]. The disagreement is, therefore, physically meaningful and its origin can be quite easily traced. If we explicitly separate the

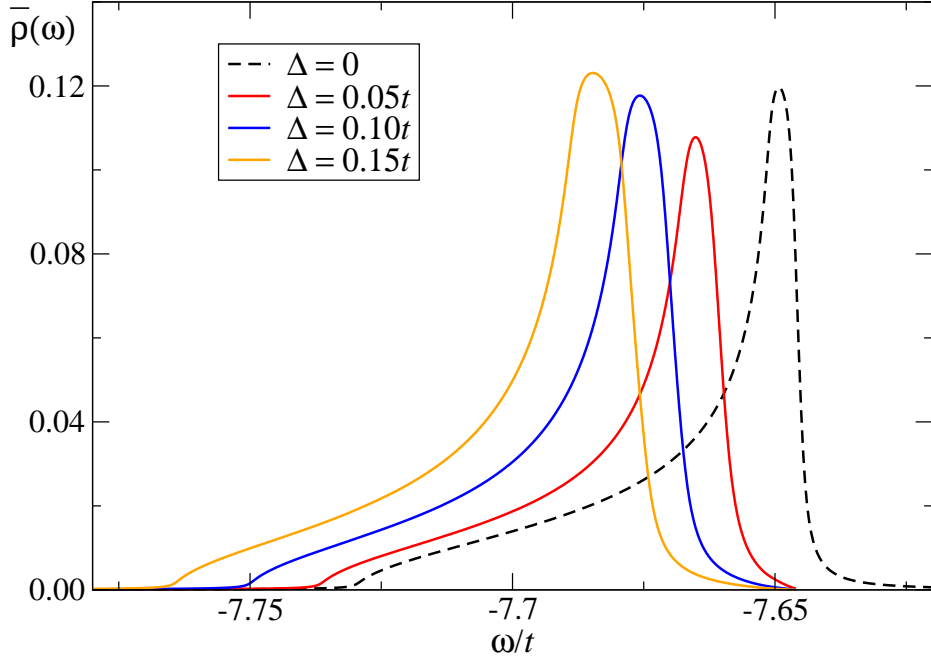


Figure 3.4: (Color online) The same average DOS vs ω displayed in the lower panels of Fig. 3.3, but now shown for the entire polaron band.

$n = m = 0$ contribution in the disorder self-energy, Eq. (3.12) becomes

$$\Sigma_{\text{dis}}(\omega) = \sigma^2 g_0(\omega - \Sigma_{\text{MA}}(\omega)) + \sigma^2 \sum_{n+m>0} \frac{\Gamma_n(\omega) W^{nm}(\omega) \Gamma_m(\omega)}{n!m!}.$$

If the contribution of terms with $n + m > 0$ can be ignored, this result reduces to Fermi's golden rule, since $\rho(\omega) = -\frac{1}{\pi} \text{Im} g_0(\omega - \Sigma_{\text{MA}}(\omega))$. The disagreement between MA and FGR, then, comes from the contribution of the terms with $n + m > 0$. These terms cannot be ignored at strong electron-phonon coupling. Consider, for instance, $F_{\mathbf{k}i}^{(n)}(\omega) = \langle 0 | c_{\mathbf{k}} \hat{G}_{\text{H}}(\omega) c_i^\dagger b_i^{\dagger n} | 0 \rangle$, which is proportional to $\Gamma_n(\omega)$. If we Fourier transform to real times, $F_{\mathbf{k}i}^{(n)}(\tau)$ is proportional to the amplitude of probability that if an electron is injected in the system, it is found in the presence of n bosons at a later time τ , all at the same site. At strong couplings, the electron dresses itself with a large phonon cloud to become a polaron, so the probability of finding it with many phonons in its vicinity should be considerable, while the probability of finding the electron without any phonons ($n = 0$) is exponentially small. In the large λ limit, the terms which are expected to contribute most are

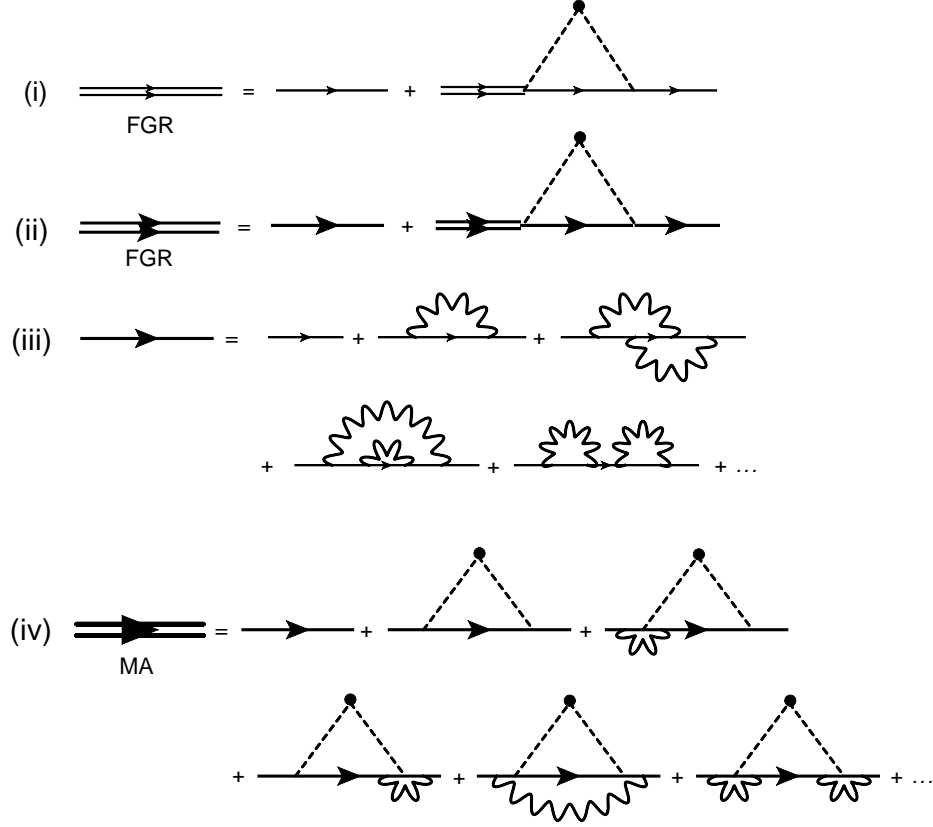


Figure 3.5: (i) FGR approximation for the disorder-averaged Green's function of a carrier (double thin line), in terms of that of the free carrier (thin line) and uncorrelated disorder (dashed line) in the absence of electron-phonon coupling; (ii) FGR approximation for the disorder-averaged GF of a polaron (double thick line), in terms of that of the clean polaron (thick line); (iii) clean polaron GF in terms of free carrier (thin lines) and phonon (curly lines) propagators; (iv) the first few terms in the MA approximation for the disorder averaged GF of a polaron.

those with $n \approx g^2/\Omega^2$, i.e., values close to the average number of phonons in the polaron cloud. In contrast, for small λ the phonon cloud is very fragile and, in fact, most of the time the electron is alone (resulting in a large quasiparticle weight). This is why, for weak coupling, keeping only the $n = m = 0$ term in the sum is a good approximation.

These considerations are illustrated diagrammatically in Fig. 3.5. Panel

3.3. Results

(i) shows the Born approximation for the disorder averaged GF of a carrier, which leads to Fermi golden's rule expression for the lifetime, as already discussed. Panel (ii) shows the same for the disorder averaged GF of the polaron; as discussed above, this is equivalent with keeping only the $n = m = 0$ term in the disorder self-energy, Eq. (3.12). Since each clean polaron propagator starts and ends with a free carrier propagator, this approximation means that the electron can scatter from disorder only in the absence of phonons; this is why this approximation fails at large electron-phonon coupling, where the chance of having no phonons around during an impurity scattering is extremely weak. In contrast, the full MA expression includes diagrams such as shown in panel (iv), where phonon and disorder lines cross. One can think of these as leading to an effective renormalization of the disorder strength, especially since these diagrams are very similar to those which result in the renormalization of a single impurity potential [1], details discussed in chapter 2.

The complete evolution of $\tau_{\mathbf{k}}^{-1}$ and $E_{\mathbf{k}}$ with disorder Δ at strong electron-phonon coupling is shown in Fig. 3.6 for two different momenta $\mathbf{k}_1 = (2\pi/9, 0, 0)$ and $\mathbf{k}_2 = (\pi/6, 0, 0)$, whose free electron energies are $\varepsilon(\mathbf{k}_1) \approx -5.5t$ and $\varepsilon(\mathbf{k}_2) \approx -5.7t$, respectively. In Fig. 3.6(a), we trace their inverse lifetimes as a function of disorder. At small Δ , the energies of both these states are well above E_{GS} and their scattering rates increase monotonically with Δ , as one would expect on general grounds. However, the inverse lifetimes reach a maximum after which they begin to decrease fast and vanish eventually. The value of Δ where $\tau_{\mathbf{k}}^{-1}$ vanishes corresponds to the disorder at which $E_{\mathbf{k}} = E_{GS}$. For larger disorder, $E_{\mathbf{k}}$ moves below the free polaron band edge, and its lifetime remains infinite. This is more clearly shown by Fig. 3.6(b), where the inverse lifetimes are plotted vs. the corresponding eigenenergy $E_{\mathbf{k}}$ for these two momenta, as disorder is increased. This confirms that the scattering rates for both polaron states vanish when their energy drops below E_{GS} , whose location is marked by the asterisk. The value of Δ where this happens depends on how far above E_{GS} was the energy $E_{\mathbf{k}}$ of this polaron, in the limit of $\Delta \rightarrow 0$.

Figure 3.3 shows that using the FGR expression, i.e. $\tau_{\mathbf{k}}^{-1} = \pi\sigma^2\rho(E_{\mathbf{k}})$, is quantitatively wrong. We can also compare the polaron lifetime, where finite, with that of a free particle of renormalized mass, similar to the comparison in Fig. 3.2. This is shown in Fig. 3.7, where we compare $1/(t^*\tau_{\mathbf{k}})$ vs Δ/t^* for the polaron, with the inverse lifetime of a free electron at the same momentum. While roughly quadratic dependence is observed for the polaron at small disorder, the coefficient is quite different from that for the free electron. For strong disorder, the disagreement is even worse.

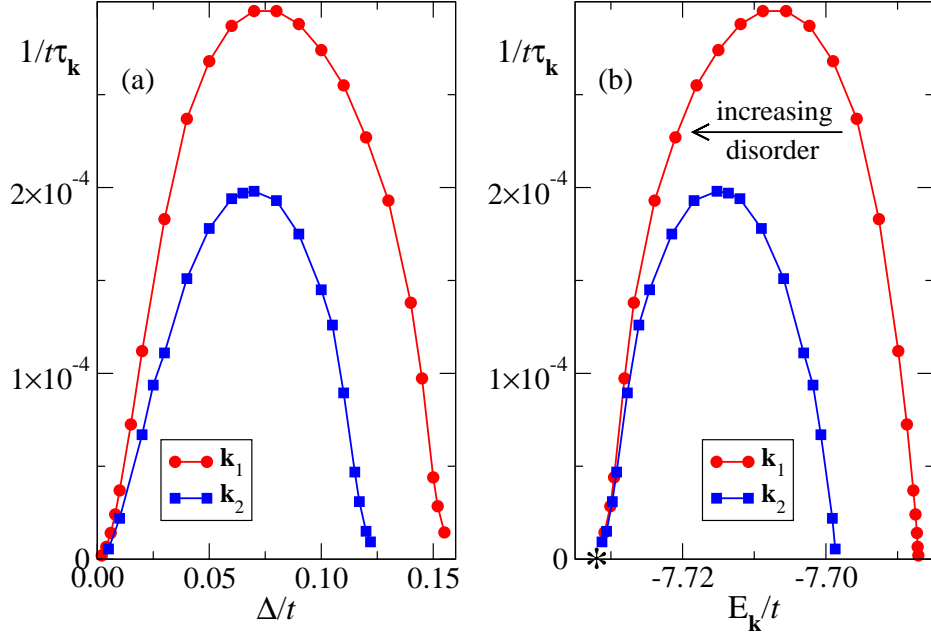


Figure 3.6: (Color online) (a) Inverse lifetime vs disorder, and (b) inverse lifetime vs energy $E_{\mathbf{k}}$, as disorder is turned on, for two momenta $\mathbf{k}_1 = (2\pi/9, 0, 0)$ and $\mathbf{k}_2 = (\pi/6, 0, 0)$, for a polaron with $\lambda = 1.2, \Omega = t, \eta = 10^{-3}t$. The asterisk in panel (b) marks the clean polaron GS energy in the clean system, E_{GS} , for these parameters. See text for more details.

This shows that for intermediate and large electron-phonon coupling, where a heavy small polaron forms, its lifetime in the presence of disorder is not described quantitatively by the predictions corresponding to a bare particle with renormalized mass. The polaron has an internal structure which manifests itself as a significant deviation from Fermi's golden rule predictions even for weak disorder. The scattering of the electron in the presence of its phonon cloud is quite different from that of a bare particle of the same effective mass, but without a cloud [1, 32].

3.4 Summary and conclusions

Using MA to deal with the electron-phonon coupling and perturbation theory to deal with the weak disorder, we derived an expression for the disorder-averaged GF of the Holstein polaron in a simple cubic lattice with random

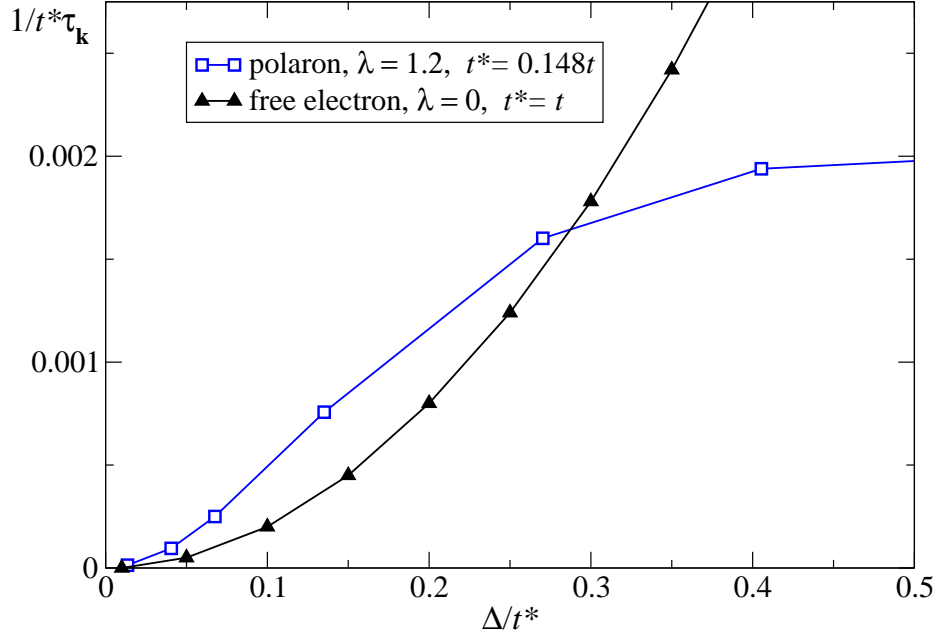


Figure 3.7: (color online) Same data as shown in Fig. 3.6(a) but with rescaled axes; $1/(t^*\tau_{\mathbf{k}})$ vs Δ/t^* for momentum $\mathbf{k}_2 = (2\pi/9, 0, 0)$ (empty squares) is compared with the free electron lifetime (triangles) at the same momentum, for $\lambda = 1.2$ where $t^* = 0.148t$. Other parameters are $\Omega = t$ and $\eta/t = 10^{-3}$.

on-site energies. This allowed us to find an analytic expression for the lowest-order contribution from disorder to the polaron self-energy.

The disorder-averaged spectral function was used to extract the lifetime and energy shift of various polaron states. For weak electron-phonon coupling, we found that the MA results are in reasonable quantitative agreement with those predicted by Fermi's golden rule for a free particle with a properly renormalized mass.

At intermediate and larger electron-phonon coupling where a small polaron forms, however, the MA results quantitatively disagree with Fermi's golden rule estimate everywhere the lifetime is finite and for all levels of disorder. The reason for this is the fact that the scattering of the electron in the presence of its (robust) phonon cloud is quite different from the scattering of a bare particle with renormalized mass. This is the same physics that leads to a significant renormalization of the disorder potential seen by a polaron as compared to the bare disorder, as discussed in the previous

3.4. Summary and conclusions

chapter [1, 32]. This demonstrates again that, in the small polaron limit, it is wrong to assume that the only effect of the polaron cloud is to renormalize the polaron's mass.

It is important to note that this calculation is only valid for weak disorder. It is based on perturbation theory, and in principle it can be improved by going to higher orders along the same lines we used to calculate the lowest-order contribution. However, one should remember that as disorder becomes stronger, Anderson localization will eventually occur, and that this cannot be captured within perturbation theory. Also, once disorder is large enough to lead to localization, the disorder-averaged GF loses its meaning and usefulness. Instead, here the signature of localization becomes manifest in the distribution of various quantities such as the local density of states, not in their average value.

A surprise, at least at first sight, is the fact that this calculation predicts an infinite lifetime for a range of energies at the bottom of the polaron band. This interval can include a significant fraction of the polaron states, especially at stronger electron-phonon coupling and larger disorder. As we already mentioned, this is in fact similar to what happens for a free particle, which also is predicted, within this level of perturbation theory, to have an infinite lifetime for all momenta for which $|E_{\mathbf{k}}| > 6t$. The difference is only quantitative: the energy shift for a free particle is tiny compared with its bandwidth of $12t$, whereas for a small polaron this shift can be comparable with its significantly narrower bandwidth even for rather weak disorder.

A likely reason for this can be inferred from the fact that, for a free particle, states at the band edge become localized immediately upon introduction of disorder. In other words, we already know that there is a finite range of energies (which, for weak disorder, falls outside the free particle bandwidth) where treating disorder perturbationally and calculating the disorder-averaged GF is meaningless. It is then reasonable to conclude that the states for which this perturbational scheme predicts infinite lifetimes are, in fact, already localized. If this is correct and generalizes to the polaron case, it suggests that, unlike for a free particle, for a polaron localization sets in differently at the lower vs the upper polaron bandedge. We have already speculated that this difference may be due to the influence of the higher-energy states that exist in the polaron spectrum. Confirmation of these conclusions will require a study going beyond a perturbational treatment of disorder.

Chapter 4

Binding carriers to a non-magnetic impurity in a two-dimensional square Ising anti-ferromagnet

4.1 Introduction

In chapters 2 and 3, I studied some of the effects caused by disorder on a Holstein polaron, which is a quasiparticle resulting from the dressing of a charge carrier by lattice vibrations. I change gears in this chapter to focus on a different type of charge carrier-boson coupling problem, namely a hole in a two-dimensional anti-ferromagnet (AFM) [64–68]. This is in part motivated by the physics of high- T_c superconductivity in cuprates. In their parent compound, the strong hybridization between copper $3d$ and oxygen $2p$ orbitals drives their CuO_2 layer into a correlated insulating state in which the holes on neighboring copper atoms align their spins anti-ferromagnetically in order to gain the superexchange energy, J . Upon doping these AFM layers with charge carriers, superconductivity emerges [69, 70].

A major setback in the search for an analytic description of the behavior of these charge carriers is the lack of a simple wave function for the ground state of the undoped AFM. The semi-classical Néel state breaks spin rotation symmetry and is therefore smeared out by quantum spin fluctuations to a significant degree that is hard to capture with simple wave functions [71]. This leaves numerical calculations as the only way to make quantitative predictions [72]. While implementing such numerical calculations is already a complicated task even for a clean system, a further complication comes from the presence of disorder and imperfections in the real materials, introduced during the sample growth and preparation. Given the low dimensionality, even weak disorder may have dramatic effects on the motion of charge carriers in the CuO_2 layers.

Impurities have been shown to be responsible for a range of phenomena in low-dimensional correlated electron systems, and they can be also utilized for probing correlations which are otherwise difficult to observe in the ground state [73]. For the undoped parent compound, mean-field analysis of the disordered Hubbard model predicts the emergence of an inhomogeneous metallic phase in which the Mott gap is locally closed wherever the disorder is strong enough to do so [74]. However, it is not always the case that impurities destroy the order in the underlying system. For instance, impurities induce local magnetic order in one-dimensional (1D) quantum magnets [75], and long-range antiferromagnetism is predicted upon doping some quantum spin liquids with nonmagnetic impurities [76]. In any event, a complete understanding of the interplay between disorder and AFM correlations and especially of their role in controlling the carrier dynamics away from half-filling is still lacking.

Here, I consider a much simpler variant of this problem where, at zero temperature, a hole is created in a 2D Ising AFM on a square lattice, and is also subject to the on-site attractive potential of an impurity that can be visited by the hole. Thus, this model is very different from previous models of an impurity in a 2D Heisenberg AFM, which assumed that the hole cannot visit the impurity site, and is coupled to it at most through exchange [77, 78]. As we discuss in the following, our results have some similarities but also considerable differences from those obtained numerically in these other models.

I investigate the local density of states (LDOS) near this impurity to study the appearance of bound states, focusing specifically on the relevance of the magnetic sublattice on which the impurity is located. The advantage of our approach is that the wave function of the undoped 2D AFM is the simple Néel state, and this allows us to study the problem (quasi)analytically. Of course, spin fluctuations are completely absent, but as we argue in our discussion, our results allow us to speculate about (at least some of) their likely effects.

A single hole in an Ising AFM was initially believed to be localized even in the absence of impurities, because when the hole hops it reshuffles the spins along its path, thereby it creates a string of wrongly oriented spins. Finite mobility was believed to arise only due to spin fluctuations which can remove pairs of such defects [79, 80], but they are absent from the Ising Hamiltonian.

However, it is discussed in detail in the following sections that the hole is actually delocalized even in the Ising AFM by going twice around closed loops. The string of misaligned spins that are created in the first round is

removed when spins are reshuffled again during the second round. When the last one is removed, the hole ends up at a different site from where it started, and by repeating this process it can move anywhere on its original sublattice (spin conservation ensures that the hole propagates on one sublattice). This raises the question of how the hole's motion will be affected by an attractive impurity, especially by one located on the other sublattice than the one on which the hole resides. While one expects the hole to become bound to the impurity if they are on the same sublattice, if they are on different sublattices, one may expect the hole not to be sensitive to the presence of the impurity and therefore remain unbound. We investigate this problem using a variational method introduced in Ref. [2] to study the clean case, which we generalize here to systems that are not invariant under translations.

I introduce the model and its variational solution in Sec. 4.2. The generalization of this variational method to inhomogeneous systems is discussed in Sec. 4.3, followed in Sec. 4.4 by results for a single impurity located (i) on the same, and (ii) on the other sublattice than the quasiparticle. I conclude by giving a summary and discussing possible further developments of this work in Sec. 4.5.

4.2 The Model

We consider the motion of a single hole doped into a spin- $\frac{1}{2}$ Ising antiferromagnet on a 2D square lattice. The Hamiltonian of the undoped system is

$$\mathcal{H}_{\text{AFM}} = J \sum_{\langle i,j \rangle} [S_i^z S_j^z + \frac{1}{4}] = \bar{J} \sum_{\langle i,j \rangle} [\sigma_i^z \sigma_j^z + 1], \quad (4.1)$$

where σ^z is the Pauli matrix and $\bar{J} = J/4 (> 0)$. Since the square lattice is bipartite, the vacuum state of Hamiltonian (4.1), $|0\rangle$, is the Néel-ordered state where all spins on one sublattice point up and those on the other sublattice point down. Excitations are gapped spin-flips that are like localized magnons. The creation operator for a magnon is written in terms of the spin raising and lowering operators, $\sigma^\pm = \sigma^x \pm i\sigma^y$:

$$d_i^\dagger = \begin{cases} \sigma_i^- & \text{if } i \in \uparrow \text{ sublattice,} \\ \sigma_i^+ & \text{if } i \in \downarrow \text{ sublattice.} \end{cases} \quad (4.2)$$

Consider now the doped case, Fig. 4.1. Creating a hole on a particular lattice site corresponds to removing the spinfull particle located at that site.

4.2. The Model

Therefore the hole creation operators are

$$h_i^\dagger = \begin{cases} c_{i\uparrow} & \text{if } i \in \uparrow \text{ sublattice,} \\ c_{i\downarrow} & \text{if } i \in \downarrow \text{ sublattice,} \end{cases} \quad (4.3)$$

where $c_{i\sigma}$ is the fermion annihilation operator. Once the hole is created (h_i^\dagger), it can move in the lattice via nearest-neighbor (nn) hopping. As each site's nn belong to the other sublattice, when the hole switches sites with a nearby spin, the latter will find itself surrounded by parallel spins. Therefore, a magnon is created on this site (d_i^\dagger). The same hop may annihilate a magnon from the hole's arrival site (d_j), if there was one already there. Therefore, the Hamiltonian can be written as [2]

$$\mathcal{H} = \mathcal{H}_{\text{AFM}} + \mathcal{P} \left\{ -t \sum_{\langle i,j \rangle} [h_j^\dagger h_i (d_i^\dagger + d_j) + \text{H.c.}] \right\} \mathcal{P} - U h_0^\dagger h_0, \quad (4.4)$$

where \mathcal{P} is the projection operator enforcing no double occupancy: at any site, there is a hole or there is a spin which is either properly oriented or is flipped, $h_i^\dagger h_i + d_i^\dagger d_i + d_i d_i^\dagger = 1$. Thus, the second term describes the hopping of the hole which is accompanied by either magnon creation or annihilation. In addition, there is an attractive potential of strength U centered at the origin $\mathbf{r} = \mathbf{0}$, which changes the on-site energy of the visiting hole (variations of the local hoppings and exchanges can be trivially included in the model and our solution, but should not lead to any qualitative changes if they are small or moderate in size). Physically, such a potential can be due to an attractive non-magnetic impurity located above the origin, in a different layer, which modulates the on-site energy at the origin. Another possibility comes from replacing the atom at the origin by an impurity atom with the same valence, but whose orbitals lie at lower energies than those of the background atoms. This is very different from the impurity models studied in previous work where the impurity is an inert site that can not be visited by carriers [77], and there is at most exchange between the spin of the impurity and that of carriers located on neighboring sites [78].

Note that bosons in this model actually help the hole to move in the lattice by modulating its kinetic energy. This contrasts with the Holstein model, where the bosons (phonons) affect the potential energy of a particle that was already mobile, thereby increase its effective mass. Hamiltonian (4.4) is similar to the limiting form ($t_f \rightarrow 0$) of the Edwards fermion-boson model which describes the modulation of a particle's hopping via coupling

4.3. Propagation of the hole in the clean system

to dispersionless bosons (b) [81–83]:

$$\mathcal{H}_{\text{Edw.}} = -t_f \sum_{\langle i,j \rangle} (c_i^\dagger c_j + \text{H.c.}) + \Omega \sum_i b_i^\dagger b_i - t_b \sum_{\langle i,j \rangle} c_i^\dagger c_j (b_j^\dagger + b_i). \quad (4.5)$$

Unlike in our model, however, there is no constraint in this model regarding the number of bosons at any site which can be simultaneously occupied by the particle as well. Furthermore, in a Néel AFM the energy of neighboring magnons is not additive as in the Edwards model.

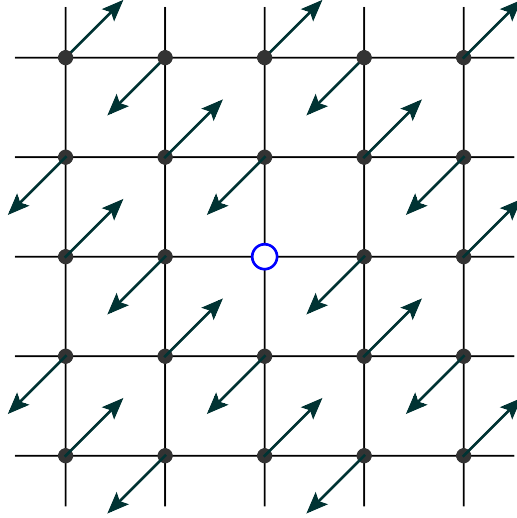


Figure 4.1: Square lattice of Néel-ordered Ising spins. Removing one of the spin-up particles creates a hole and results in a configuration with $s_z = -\frac{1}{2}$.

4.3 Propagation of the hole in the clean system

In this section, we construct the equations of motion for the zero-temperature retarded Green's function (GF) of the hole moving through the lattice in the absence of impurity, $U = 0$. Due to the translational invariance in the clean system, one can do this in the momentum-space and calculate $G(\mathbf{k}, \omega)$, which is done in Ref [2]. Here, we present a real-space derivation which is needed once the translational invariance is broken when the impurity is added. The real-space single hole retarded GF is defined as

$$G_{\mathbf{0},\mathbf{R}}(\omega) = \langle 0 | h_{\mathbf{0}} \hat{G}(\omega) h_{\mathbf{R}}^\dagger | 0 \rangle, \quad (4.6)$$

4.3. Propagation of the hole in the clean system

where $\hat{G}(\omega) = \lim_{\eta \rightarrow 0^+} 1/(\omega - \mathcal{H} + i\eta)$ is the resolvent of Hamiltonian (4.4) when $U = 0$. By separating the Hamiltonian as $\mathcal{H} = \mathcal{H}_{\text{AFM}} + \mathcal{H}_t$ where \mathcal{H}_t is the second term responsible for hopping, equations of motion for $G_{\mathbf{0},\mathbf{R}}(\omega)$ can be generated by repeated use of the Dyson identity

$$\hat{G}(\omega) = \hat{G}_{\text{AFM}}(\omega) + \hat{G}(\omega)\mathcal{H}_t\hat{G}_{\text{AFM}}(\omega),$$

in which $\hat{G}_{\text{AFM}}(\omega) = \lim_{\eta \rightarrow 0^+} 1/(\omega - \mathcal{H}_{\text{AFM}} + i\eta)$. Using this, Eq. (4.6) becomes

$$G_{\mathbf{0},\mathbf{R}}(\omega) = g_0(\omega)[\delta_{\mathbf{0},\mathbf{R}} - t \sum_{\mathbf{u}} F_1(\mathbf{R}, \mathbf{u}, \omega)], \quad (4.7)$$

where $g_0(\omega) = 1/(\omega - 4\bar{J} + i\eta)$ and $4\bar{J}$ is the cost of breaking four AFM bonds when the hole is created in the lattice. Here, the lattice constant is set to unity, $a = 1$, $\mathbf{u} = \pm\mathbf{x}, \pm\mathbf{y}$ are the four nn vectors. F_1 is a new GF which describes a process where the hole starts together with a magnon next to it,

$$F_1(\mathbf{R}, \mathbf{u}, \omega) = \langle 0 | h_{\mathbf{0}} \hat{G}(\omega) d_{\mathbf{R}}^\dagger h_{\mathbf{R}+\mathbf{u}}^\dagger | 0 \rangle. \quad (4.8)$$

To simplify the notation, from now on we do not explicitly write the dependence on ω for all these GFs.

The equation of motion for F_1 can be similarly generated. Upon applying the Dyson identity, the hole can hop back to \mathbf{R} and remove the magnon, or it can hop further away and create a second magnon, with an associated GF F_2 , and so on. However, states with many magnons are less likely to occur due to the energy cost of creating the magnons. In order to avoid the rise in the number of magnons, the hole can trace back its path to remove them, but this effectively confines the hole to the vicinity of its creation site, and results in an immobile quasiparticle which is surrounded by a cloud of magnons. It turns out that the hole is freed to move on the lattice by executing the so-called *Trugman* loop processes in which it goes twice around a closed path. By doing so, magnons that are created at the first pass are annihilated when the hole arrives at those sites for the second time. It is not hard to see that when the very last magnon is annihilated, the hole ends up two hops away from its starting point. This is equivalent to a second or third nn hop on the main lattice which translates into a first and second nn hop on the hole's sublattice, respectively.

Longer loops involve more costly intermediate states with many magnons. This suggests that we can proceed within a variational approach in which a limit is set for the maximum number of magnons that can be generated as the hole propagates. We choose to work with up to three magnons, which is the minimum number necessary for the hole to complete a loop. Moreover,

4.3. Propagation of the hole in the clean system

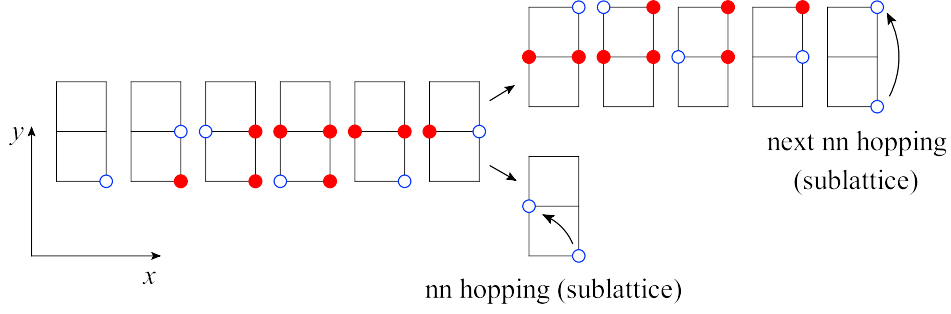


Figure 4.2: Effective first- and second-nearest-neighbor hoppings of the hole (the blue circle) achieved with loops involving only up to three magnons. The latter is realized when the hole starts a second loop before removing the last magnon it created during the first loop. The magnons are shown by red circles. The properly oriented spins are not shown.

we only keep configurations consistent with these short closed loops (i.e., we exclude, for example, configurations where all three magnons are collinear). Figure 4.2 shows how both types of effective hoppings can be generated with the three magnons types of configurations that we keep in our variational calculation. One can include more configurations in numerical simulations, but this was shown to result in only quantitative differences as long as t/J is not too large [2, 84].

Coming back to the equation of motion for F_1 , it relates F_1 to $G_{\mathbf{0},\mathbf{R}}$ and also to three GFs with two magnons, F_2 . One of these, with the two magnons collinear with the hole, cannot lead to a closed loop without generating more than three magnons. Therefore we exclude it from the variational space, as discussed. Hence, we are left with only three terms

$$F_1(\mathbf{R}, \mathbf{u}) = -tg_1[G_{\mathbf{0},\mathbf{R}} + \sum_{\mathbf{v} \perp \mathbf{u}} F_2(\mathbf{R}, \mathbf{u}, \mathbf{v})], \quad (4.9)$$

where $F_2(\mathbf{R}, \mathbf{u}, \mathbf{v}) = \langle 0 | h_{\mathbf{0}} \hat{G}(\omega) d_{\mathbf{R}}^\dagger d_{\mathbf{R}+\mathbf{u}}^\dagger h_{\mathbf{R}+\mathbf{u}+\mathbf{v}}^\dagger | 0 \rangle$, $\mathbf{v} = \pm \mathbf{x}$ if $\mathbf{u} = \pm \mathbf{y}$ and vice versa, $g_1 = 1/(\omega - 10\bar{J} + i\eta)$ and $10\bar{J}$ is the energy of the hole and a magnon next to each other. Within our variational space, the equation of motion for F_2 is

$$F_2(\mathbf{R}, \mathbf{u}, \mathbf{v}) = -tg_2[F_1(\mathbf{R}, \mathbf{u}) + F_3(\mathbf{R}, \mathbf{u}, \mathbf{v}, -\mathbf{u})], \quad (4.10)$$

where

$$F_3(\mathbf{R}, \mathbf{a}, \mathbf{b}, \mathbf{c}) = \langle 0 | h_{\mathbf{0}} \hat{G}(\omega) d_{\mathbf{R}}^\dagger d_{\mathbf{R}+\mathbf{a}}^\dagger d_{\mathbf{R}+\mathbf{a}+\mathbf{b}}^\dagger h_{\mathbf{R}+\mathbf{a}+\mathbf{b}+\mathbf{c}}^\dagger | 0 \rangle$$

4.3. Propagation of the hole in the clean system

and $g_2 = 1/(\omega - 14\bar{J} + i\eta)$. The other pair of three-magnon configurations that can be reached starting from $d_{\mathbf{R}}^\dagger d_{\mathbf{R}+\mathbf{u}}^\dagger h_{\mathbf{R}+\mathbf{u}+\mathbf{v}}^\dagger |0\rangle$ do not belong to our variational space and are hence discarded. Finally, in this variational space F_3 relates to F_2 only

$$F_3(\mathbf{R}, \mathbf{u}, \mathbf{v}, -\mathbf{u}) = -tg_3[F_2(\mathbf{R}, \mathbf{u}, \mathbf{v}) + F_2(\mathbf{R} + \mathbf{u} + \mathbf{v}, -\mathbf{v}, -\mathbf{u})], \quad (4.11)$$

with $g_3 = 1/(\omega - 16\bar{J} + i\eta)$, $16\bar{J}$ being the energy of the allowed three-spin-defect configurations.

These equations can be used to eliminate all F_3, F_2, F_1 unknowns and be left with equations involving only $G_{0,\mathbf{R}}$. The details are presented in Appendix E. The final results is

$$\begin{aligned} G_{0,\mathbf{R}}(\omega) &= \bar{g}_0(\omega)[\delta_{\mathbf{R},\mathbf{0}} - t_1(\omega) \sum_{\boldsymbol{\delta}} G_{0,\mathbf{R}+\boldsymbol{\delta}}(\omega) \\ &\quad - t_2(\omega) \sum_{\boldsymbol{\xi}} G_{0,\mathbf{R}+\boldsymbol{\xi}}(\omega)], \end{aligned} \quad (4.12)$$

in which $\bar{g}_0(\omega) = 1/(\omega - 4\bar{J} + 4t\zeta_1(\omega) + i\eta)$, $t_1(\omega) = 2t\zeta_3(\omega)$, $t_2(\omega) = t\zeta_2(\omega)$ and $\boldsymbol{\delta} = \pm\mathbf{u} \pm \mathbf{v}$ and $\boldsymbol{\xi} = \pm 2\mathbf{u}$ are all the second and third nn vectors of the main lattice, respectively. The explicit expressions of $\zeta_{1,2,3}(\omega)$ functions are given in Appendix E.

Equation (4.12) shows that the hole moves as a quasiparticle with the effective second and third nn hoppings $t_1(\omega)$ and $t_2(\omega)$, respectively, and an effective on-site energy

$$\varepsilon(\omega) = 4\bar{J} - 4t\zeta_1(\omega). \quad (4.13)$$

The hole, in this quasiparticle, is accompanied by a cloud of magnons which are constantly created and annihilated, helping it to freely propagate in the lattice. Note that sites \mathbf{R} , $\mathbf{R} + \boldsymbol{\delta}$, and $\mathbf{R} + \boldsymbol{\xi}$ belong to the same sublattice. Therefore, the quasiparticle effectively propagates in the sublattice the hole is originally created on, and whose first and second nn vectors are $\boldsymbol{\delta}$ and $\boldsymbol{\xi}$, respectively. The constraint that forces the quasiparticle to move on one sublattice is very general, being due to the spin-conserving nature of the Hamiltonian (4.4). It prevents the hole from ending up on the other sublattice without leaving an odd number of magnons behind: if the hole starts on one sublattice and ends up on the other one, the z component of the total spin angular momentum of the system changes from $S_i^z = \pm 1/2$ to $S_f^z = \mp 1/2$, therefore there needs to be an odd number of magnons around to compensate for the change of spin $S_f^z - S_i^z = \mp 1$.

4.3. Propagation of the hole in the clean system

Before presenting the real-space solution of Eq. (4.12), note that we have now enough information to identify the momentum-space Green's function

$$G(\mathbf{k}, \omega) = \langle 0 | h_{\mathbf{k}} \hat{G}(\omega) h_{\mathbf{k}}^\dagger | 0 \rangle = \frac{1}{\omega - \epsilon(\omega, \mathbf{k}) + i\eta}, \quad (4.14)$$

where $h_{\mathbf{k}} = \frac{1}{\sqrt{N}} \sum_{\mathbf{r}} \exp(-i\mathbf{k} \cdot \mathbf{r}) h_{\mathbf{r}}$ and the sum runs over $\bar{N} \rightarrow \infty$ sites of the hole's sublattice. $\epsilon(\omega, \mathbf{k})$ is the self-energy encoding the effect of being dressed by magnons, that is responsible for the dynamical generation of the hole's energy dispersion:

$$\begin{aligned} \epsilon(\omega, \mathbf{k}) = & \varepsilon(\omega) - 2t_1(\omega)[\cos(k_x + k_y) + \cos(k_x - k_y)] \\ & - 2t_2(\omega)[\cos(2k_x) + \cos(2k_y)]. \end{aligned} \quad (4.15)$$

As required, this is identical to the solution derived using a momentum space formalism in Ref. [2] and [85]. The spectral weight $A(\mathbf{k}, \omega) = -\frac{1}{\pi} \text{Im}G(\mathbf{k}, \omega)$ is then used to identify the quasiparticle excitations and their various properties such as energy dispersion, effective mass, etc [2].

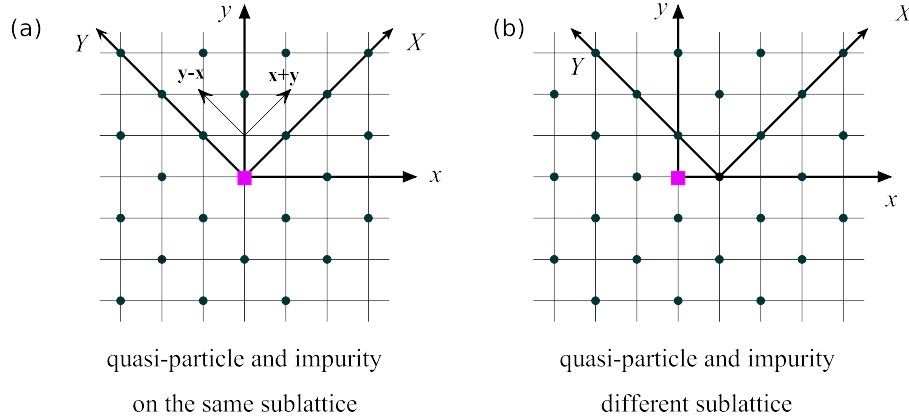


Figure 4.3: The choice of coordinate systems for the lattice with impurity. The impurity, shown as purple square, is at the origin of the xy axes that span the original lattice with unit vectors \mathbf{x}, \mathbf{y} . The XY axes are rotated by 45° and span the sublattice (black dots) on which the quasiparticle propagates via the elementary vectors $\mathbf{y} \pm \mathbf{x}$.

Equation (4.12) can be solved directly in real space by the method of continued fractions detailed in Ref. [86]. For completeness, we briefly outline it here. Let n and m be the x and y components of $\mathbf{R} \neq \mathbf{0}$ on the coordinates axes XY which is rotated by 45° with respect to the lattice. It spans the

4.3. Propagation of the hole in the clean system

sublattice on which the quasiparticle moves, marked by dots in Fig. 4.3(a), whose elementary vectors are $\mathbf{y} \pm \mathbf{x}$. In this coordinate system, Eq. (4.12) can be written as

$$\begin{aligned} \frac{G_{n,m}}{\bar{g}_0} &= -t_1(G_{n+1,m} + G_{n-1,m} + G_{n,m+1} + G_{n,m-1}) \\ &\quad -t_2(G_{n+1,m+1} + G_{n+1,m-1} + G_{n-1,m+1} + G_{n-1,m-1}), \end{aligned} \quad (4.16)$$

where $G_{n,m} \equiv G_{\mathbf{0},\mathbf{R}}$, $\mathbf{R} = n(\mathbf{y} + \mathbf{x}) + m(\mathbf{y} - \mathbf{x})$, is a shorthand notation. Eq. (4.16) can be expressed as a single-index recursive relation by grouping distinct GFs with $n \geq m \geq 0$ into column vectors V_M according to their Manhattan distance, defined as $M = n + m$

$$V_{M=2r} = \begin{pmatrix} G_{2r,0} \\ G_{2r-1,1} \\ \vdots \\ G_{r,r} \end{pmatrix}, V_{M=2r-1} = \begin{pmatrix} G_{2r-1,0} \\ G_{2r-2,1} \\ \vdots \\ G_{r,r-1} \end{pmatrix}.$$

These are the only distinct GFs at Manhattan distance M and all others can be related to these using symmetries: $G_{n,m} = G_{m,n} = G_{n,-m} = G_{-n,m}$. In terms of these vectors, Eqs. (4.16) can be grouped into the following matrix form

$$\lambda_r V_r = \tilde{\alpha}_r V_{r-2} + \alpha_r V_{r-1} + \beta_r V_{r+1} + \tilde{\beta}_r V_{r+2} \quad (4.17)$$

for $r \geq 2$ and

$$\begin{aligned} V_0 &= \bar{g}_0(\omega) + \beta_0 V_1 + \beta_0 V_2 \\ V_1 &= \alpha_1 V_0 + \beta_1 V_2 + \tilde{\beta}_1 V_3 \end{aligned} \quad (4.18)$$

for the GFs with $M = 0, 1$. Here, λ , $\tilde{\alpha}$, α , β and $\tilde{\beta}$ are extremely sparse matrices whose elements can be read from Eq. (4.16). Combining two copies of Eq. (4.17) for $r = 2s - 1$ and $r = 2s$ gives

$$\Gamma_s W_s = A_s W_{s-1} + B_s W_{s+1}, \quad (4.19)$$

where $W_s = \begin{pmatrix} V_{2s-1} \\ V_{2s} \end{pmatrix}$ and

$$\Gamma_s = \begin{pmatrix} \lambda_{2s-1} & -\beta_{2s-1} \\ -\alpha_{2s} & \lambda_{2s} \end{pmatrix}, A_s = \begin{pmatrix} \tilde{\alpha}_{2s-1} & \alpha_{2s-1} \\ 0 & \tilde{\alpha}_{2s} \end{pmatrix}, B_s = \begin{pmatrix} \tilde{\beta}_{2s-1} & 0 \\ \beta_{2s} & \tilde{\beta}_{2s} \end{pmatrix}.$$

Since Eq. (4.19) links three consecutive terms, its solution can be expressed as a continued fraction (of matrices). Assuming a solution as $W_s = \Omega_s W_{s-1}$ and using it in Eq. (4.19) gives

$$\Omega_s = (\Gamma_s - B_s \Omega_{s+1})^{-1} A_s, \quad (4.20)$$

4.3. Propagation of the hole in the clean system

which can be evaluated for Ω_s starting from a cutoff c such that $\Omega_{c+1} = 0$. This results in the continued fraction solution for Ω_s . In particular, this gives Ω_2 which relates W_2 (set of V_3 and V_4) to W_1 (set of V_1 and V_2). Finally, the diagonal element of Green's function $G_{00}(\omega)$ is found by using these in Eqs. (4.18) and (4.17) with $r = 2$ to solve for $V_0 = G_{0,0}(\omega)$. It gives the hole's local density of states (LDOS):

$$\begin{aligned}\rho(\mathbf{r}, \omega) &= -\frac{1}{\pi} \text{Im} \langle 0 | h_{\mathbf{r}} \hat{G}(\omega) h_{\mathbf{r}}^\dagger | 0 \rangle \\ &= -\frac{1}{\pi} \text{Im} G_{0,0}(\omega),\end{aligned}\tag{4.21}$$

which is same as the total density of states in the clean system. Other components of the GF, $G_{0,\mathbf{R}\neq 0}(\omega)$, can then be calculated from $G_{0,0}(\omega)$ using these recursive relations: using Ω_2 , V_3 is written in terms of V_1 and V_2 . This is used in Eq. (4.18) which is then solved for V_1 and V_2 , and so on.

In practice, the calculation is done for a finite lattice which is chosen sufficiently large that the GFs become negligible beyond its boundaries (the broadening η introduces an effective lifetime $1/\eta$ that prevents the quasiparticle from going arbitrarily far away from its original location). Note that the equations are modified for the lattice sites close to the boundary: if the hole can not hop outside the boundary, some of the generalized GFs F_1, F_2, F_3 must be set to zero for sites close to the boundary, ensuring that the hole does not go beyond the border. This modifies effective hoppings and on-site energy near the boundary. If the cutoff is large enough, however, the solution becomes insensitive to these details.

The top panels in Fig. 4.4 show the hole's total density of states (DOS) for two moderate values of t/J , for which this variational approximation was shown to be in good agreement with the numerical results [2]. The quasiparticle bandwidth for $t = 6$ is considerably larger than that for $t = 3$, showing the rapid decrease of the quasiparticle's effective mass with increasing hopping. In the lower panels, we plot its effective hoppings $t_1(\omega), t_2(\omega)$ and on-site energy $\varepsilon(\omega)$ at the same energy range. It shows that their energy dependence is relatively weak and that $t_2(\omega)$, which would make the DOS asymmetric, is vanishingly small. This explains why the quasiparticle, in spite of being dressed with magnons, has a DOS similar to that of a featureless bare particle with only a renormalized first nn hopping. However, its weak effective hopping (compared to t) and low quasiparticle weight, Fig. (4.5), suggests that the polaron is actually quite different from the bare hole as it is dressed by magnons.

4.4. The effect of the impurity

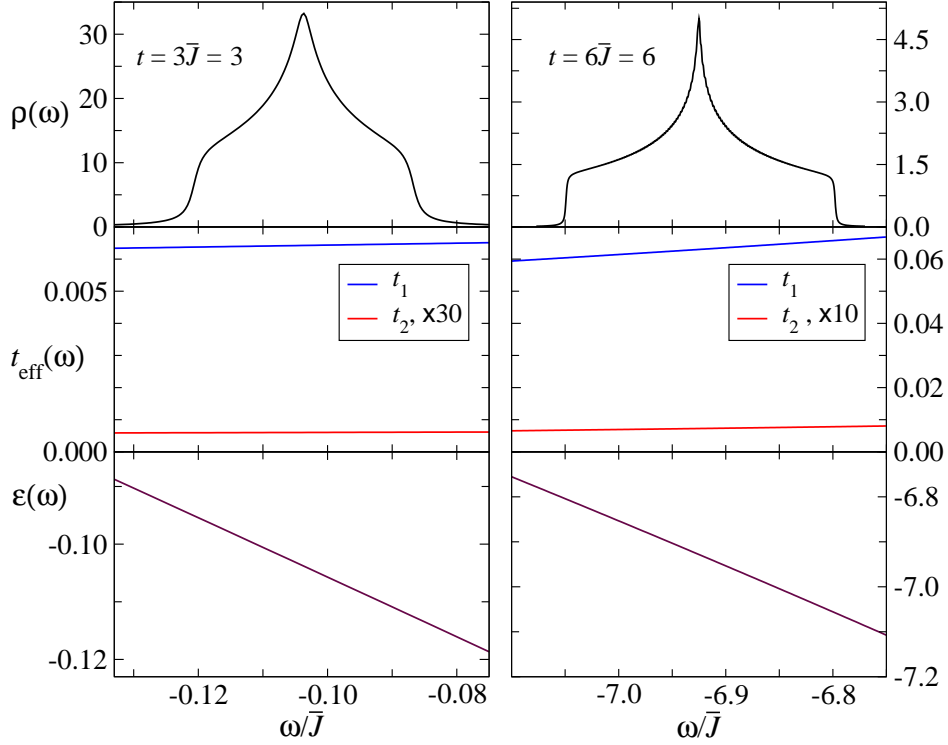


Figure 4.4: The total density of states (top panels), effective hoppings $t_1(\omega), t_2(\omega)$ (middle panels) and on-site energy $\varepsilon(\omega)$ (bottom panels) in the clean system for two different values of t/\bar{J} . The effective parameters are relatively constant within the energy band, explaining why the DOS has the generic form expected for a bare particle with nearest-neighbor hopping on a square lattice. Here $\bar{J} = 1$, $\eta = 10^{-3}$ and $t = 3$ (left panels) and $t = 6$ (right panels), respectively.

4.4 The effect of the impurity

In the previous section it was confirmed that the hole's motion in the clean system is described by an effective tight-binding Hamiltonian with second and third nearest-neighbor hoppings which keep the quasiparticle on the same sublattice at all times. In this section I investigate the effect of an attractive impurity on the spectrum of the quasiparticle. The impurity can be on the sublattice in which the quasiparticle moves, or it can be on the other sublattice. In the former case, one expects the quasiparticle to bind to the impurity. As mentioned in the introduction, when they are on different

4.4. The effect of the impurity

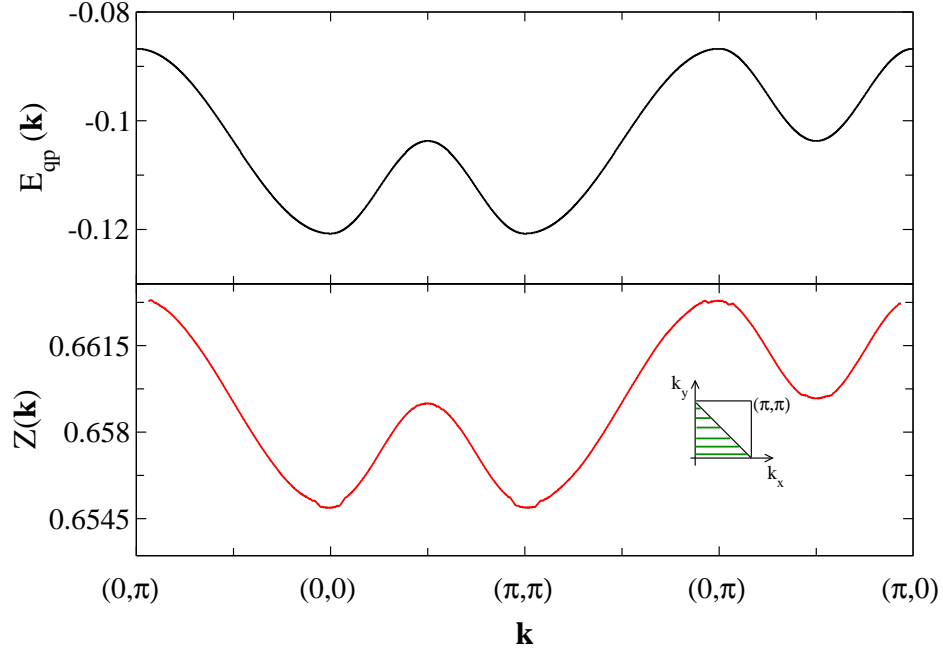


Figure 4.5: (Top): the energy dispersion and the quasiparticle weight for the lowest polaron band. The ground state is at $\mathbf{k} = (0, 0)$, while $\mathbf{k} = (\frac{\pi}{2}, \frac{\pi}{2})$ is a saddle point. The top-right quadrant of the full Brillouin zone (BZ) and that of the corresponding magnetic BZ (dashed green) is shown at the inset. The band folding due to AFM order leads to symmetric dispersion along $(0, 0) - (\pi, \pi)$. The quasiparticle weight has only minor variations which can be related to the fact that the polaron bandwidth (≈ 0.3) is considerably smaller than the energy of a typical spin defect (few \bar{J}) in the magnon cloud. $t = 3\bar{J} = 3$ and $\eta = 10^{-3}$.

sublattices one might naively expect the quasiparticle to remain mobile and insensitive to the presence of impurity. However, we will see that this is not the case.

4.4.1 Quasiparticle and impurity on the same sublattice

The translational invariance of the clean system requires the equal spreading of the hole's wave function over the entire lattice. This is expected to change when introducing an attractive impurity and, in particular, there may exist low-energy bound states where it is energetically more favourable for the hole to stay close to the impurity. This tendency can be studied using

4.4. The effect of the impurity

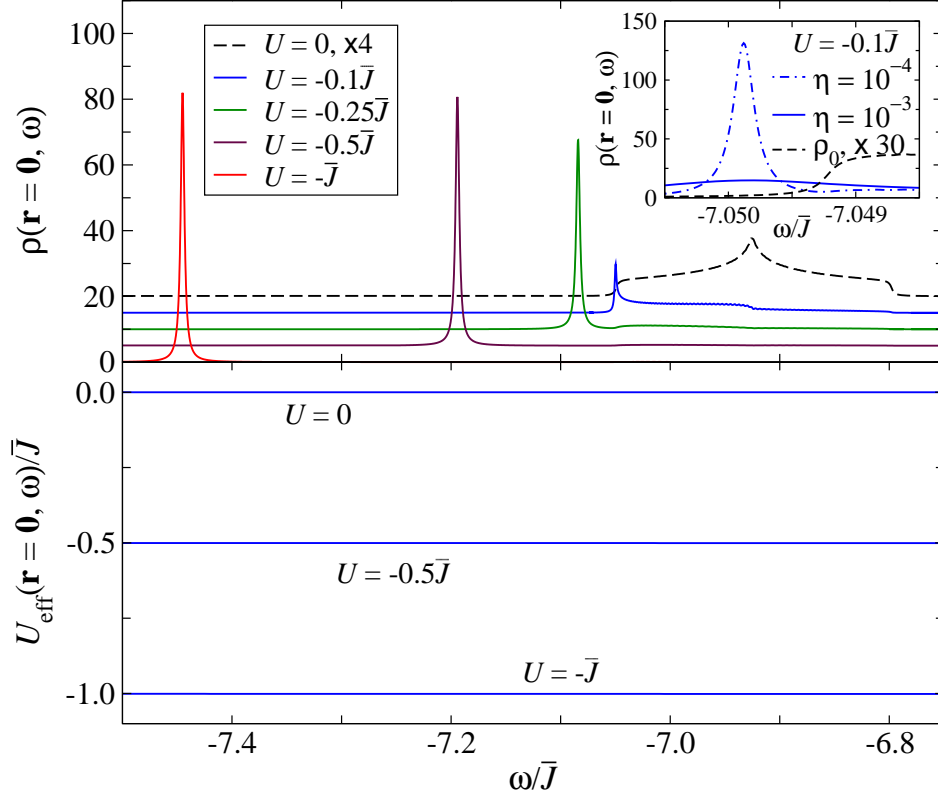


Figure 4.6: (Top) LDOS at the impurity site for various values of U . The dashed line is the DOS in the clean system, times 4. At finite U , a single bound state splits from the continuum and its binding energy increases with U . Curves are shifted vertically to help visibility. (bottom) The effective on-site energy at the impurity site is essentially equal to U . Parameters are $t = 6$, $\bar{J} = 1$ and $\eta = 10^{-3}$.

the hole's Green's function, $G_{\mathbf{0},\mathbf{R}}(\omega)$, where \mathbf{R} and the impurity site, $\mathbf{r} = \mathbf{0}$ belong to the same sublattice. This can be calculated as we explained in the previous section, while keeping track of the position of hole with respect to the impurity in order to include the energy gain U whenever they meet. This modifies some of the equations of motion. For example, Eq. (4.7) now reads as

$$G_{\mathbf{0},\mathbf{R}}(\omega) = g_0(\omega, \mathbf{R})[\delta_{\mathbf{0},\mathbf{R}} - t \sum_{\mathbf{u}} F_1(\mathbf{R}, \mathbf{u}, \omega)], \quad (4.22)$$

4.4. The effect of the impurity

where $g_0(\omega, \mathbf{R}) = 1/(\omega + i\eta + U\delta_{\mathbf{R},\mathbf{0}} - 4\bar{J})$. The coefficients in the equations of motion for F_2 also become position-dependent, reflecting the possibility of the hole being at the impurity site. The equations for F_1 and F_3 , for which the hole is on the sublattice without the impurity, remain the same as their counterparts in the clean system. Tracking these changed coefficients and their effects on the effective hoppings and on-site energies, we now find

$$G_{\mathbf{0},\mathbf{R}}(\omega) = \tilde{g}_0(\omega, \mathbf{R})[\delta_{\mathbf{R},\mathbf{0}} - \sum_{\delta} \tilde{t}_1(\mathbf{R}, \delta, \omega)G_{\mathbf{0},\mathbf{R}+\delta}(\omega) - \sum_{\xi} \tilde{t}_2(\mathbf{R}, \xi, \omega)G_{\mathbf{0},\mathbf{R}+\xi}(\omega)], \quad (4.23)$$

which is similar to Eq. (4.12), but now \tilde{t}_1 and \tilde{t}_2 depend both on the location and on the direction of hopping, if \mathbf{R} has the impurity within the range of its second or third nn. If \mathbf{R} is further away, the effective parameters take the same values as in the clean system.

Equation (4.23) can be solved similar to Eq. (4.12), that is, by grouping GFs according to their Manhattan distance. Because the problem is still symmetric about the origin where the impurity is located, $G_{\mathbf{0},\mathbf{R}}(\omega)$ continues to have the same symmetries as in the clean system. Therefore, only the GFs corresponding to $n \geq m \geq 0$ need to be calculated.

Given the almost constant values of ε , t_1 and t_2 in this range of energies and the fact that the problem is two dimensional, bound states are expected to appear for any finite U . The top panel in Fig. 4.6 shows the LDOS at the impurity site $\mathbf{r} = \mathbf{0}$ for various values of the on-site attraction U . The peaks that appear below the DOS of the clean system (shown by the dashed line) are proportional to Dirac delta functions which are broadened into Lorentzians by the finite η . They signal the appearance of quasiparticle bound states, characterized by exponential decay of the quasiparticle's wave function $\psi_b(\mathbf{r})$ away from the impurity. The inset verifies that this is true even for the smallest U : the height of the "shoulder"-like feature appearing at the bottom of the band in the main figure scales like $1/\eta$ and evolves into a separate Lorentzian for small enough η , showing the presence of a bound state below the continuum.

The bottom panel shows the effective attraction at the impurity site defined as the difference between the effective on-site potential, Eq. (4.13), at $\mathbf{r} = \mathbf{0}$ and that of sites far away from the impurity (or in the clean system), $U_{\text{eff}}(\mathbf{r} = \mathbf{0}, \omega) = \text{Re}[\varepsilon(\mathbf{r} = \mathbf{0}, \omega) - \varepsilon(\omega)]$. Not surprisingly, $U_{\text{eff}}(\mathbf{r} = \mathbf{0}, \omega) \approx U$, although a small energy dependence, associated with the hole's fluctuation to nearby sites, is observed if the scale is significantly expanded.

4.4. The effect of the impurity

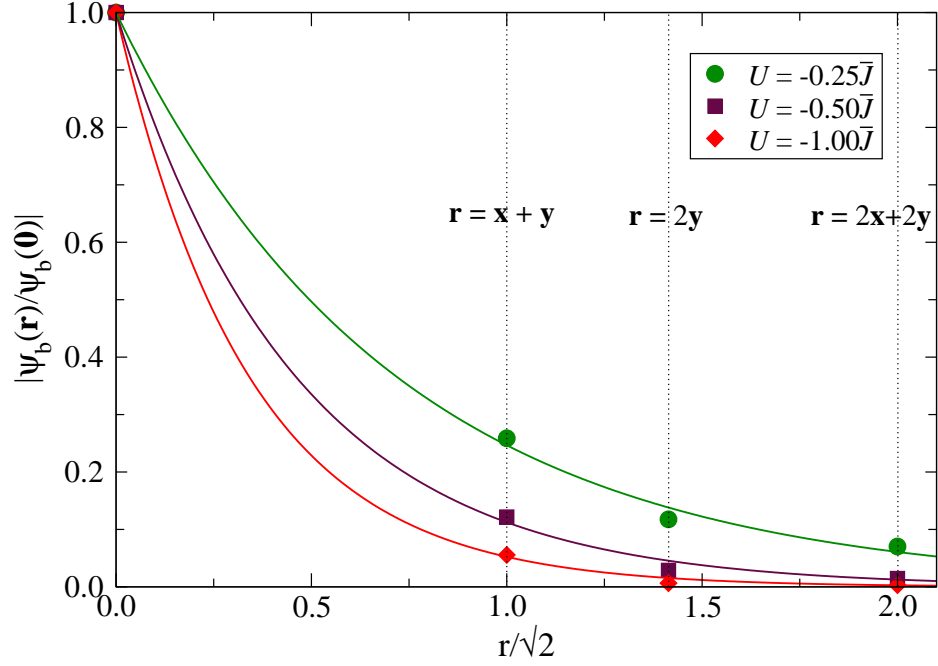


Figure 4.7: Relative amplitude of the wave functions corresponding to three of the bound states shown in Fig. 4.6, at various distances from the impurity site. Lines are exponential fits. States with bigger binding energies have shorter decay lengths.

The exponential decay of the quasiparticle's wave function away from the impurity can be verified explicitly by calculating the amplitude of these bound states at various distances from the impurity, \mathbf{r} . This can be done by approximating $G_{\mathbf{0},\mathbf{r}}(\omega)$, at the bound state energy E_b , to the term in the Lehmann representation which is dominated by the bound state,

$$G_{\mathbf{0},\mathbf{r}}(\omega = E_b) = \lim_{\eta \rightarrow 0} \sum_{\psi} \frac{\psi(\mathbf{0})^* \psi(\mathbf{r})}{\omega - E_{\psi} + i\eta} \Big|_{\omega=E_b} \approx \frac{1}{i\eta} \psi_b(\mathbf{0}) \psi_b(\mathbf{r})^*. \quad (4.24)$$

Figure 4.7 shows the ratio $|\psi_b(\mathbf{r})/\psi_b(\mathbf{0})| = |G_{\mathbf{0},\mathbf{r}}(E_b)/G_{\mathbf{0},\mathbf{0}}(E_b)|$. The dots are the numerical values, while the lines are exponential fits. Those corresponding to larger binding energies (more negative E_b) are more tightly bound to the impurity and therefore decay faster, as expected. This agrees with the larger quasiparticle weight of these states at $\mathbf{r} = \mathbf{0}$, (see Fig. 4.6).

4.4. The effect of the impurity

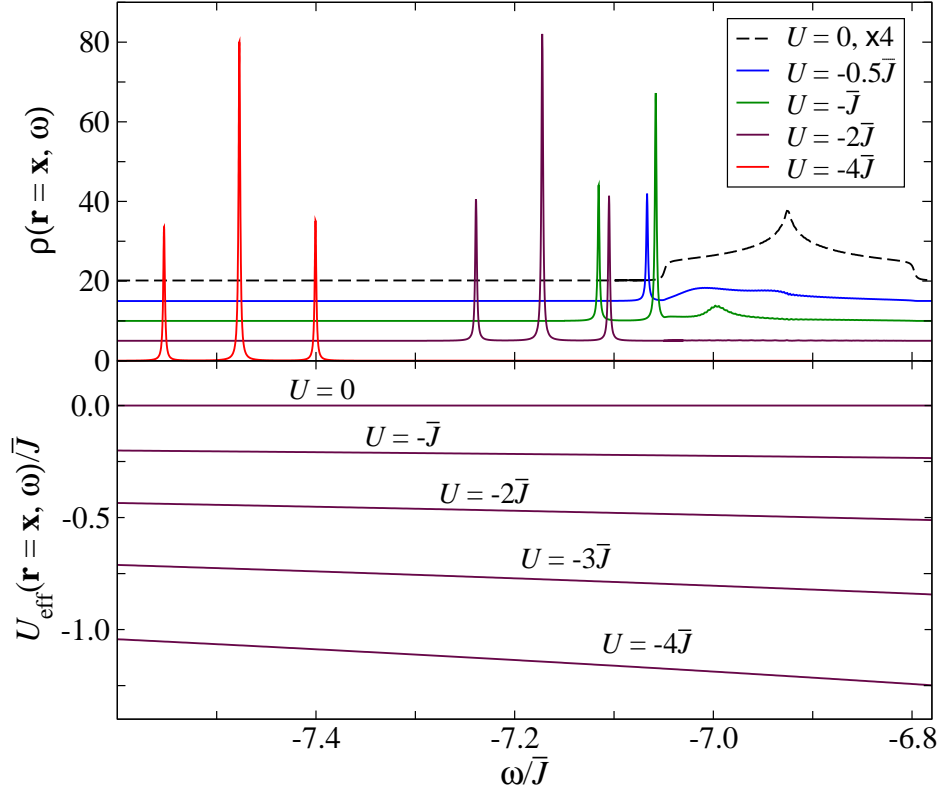


Figure 4.8: (Top) LDOS $\rho(\mathbf{r}=\mathbf{x};\omega)$ with curves shifted vertically to help visibility; (Bottom) $U_{\text{eff}}(\mathbf{r}=\mathbf{x};\omega)$ at the quasiparticle's sublattice site located nearest to the impurity. Up to three bound states split from the continuum upon increasing U . The presence of the impurity at $\mathbf{r}=\mathbf{0}$ induces a finite effective on-site attraction at $\mathbf{r}=\mathbf{x}$, whose value is significantly smaller than U (Bottom). Parameters are $t=6$, $\bar{J}=1$, and $\eta=10^{-3}$.

4.4.2 Quasiparticle and impurity on different sublattices

We now investigate the more interesting case with the impurity and the quasiparticle located on different sublattices. To this end, we construct the Green's function $G_{\mathbf{x},\mathbf{R}}(\omega)$ in which \mathbf{x} and \mathbf{R} are on the quasiparticle's sublattice (the rotated frame XY is centered to the right of the impurity, see Fig. 4.3(b)). In particular, we are interested in the LDOS on this sublattice closest to the impurity $\rho(\mathbf{r}=\mathbf{x},\omega)=-\frac{1}{\pi}\text{Im}G_{\mathbf{x},\mathbf{x}}(\omega)$, where the amplitude of possible bound states is strongest.

The equations of motion for $G_{\mathbf{x},\mathbf{R}}(\omega)$ are derived as before, however here

4.4. The effect of the impurity

the equations for F_1 and F_3 are modified by the presence of the impurity if \mathbf{R} is close enough to it. This leads to equations of motion for $G_{\mathbf{x},\mathbf{R}}(\omega)$ that are similar to those in Eq. (4.23), but with different values for the effective hoppings and on-site energies close to the impurity. We solve these equations using the same method, but note that the number of distinct GFs is considerably higher compared to the previous case due to the lower symmetry here.

In Fig. 4.8, we plot $\rho(\mathbf{r} = \mathbf{x}, \omega)$ for various values of U . The appearance of Dirac delta peaks shows that bound states exist in this case as well. A comparison with $\rho(\mathbf{r} = \mathbf{0}, \omega)$ in Fig. 4.6 for the same value of U shows that these peaks have different energies. Therefore, they are distinct bound states and we are not just looking at the tails of the same states. This is further confirmed by the fact that up to three bound states appear here for sufficiently large U , as opposed to only one when the quasiparticle and the impurity were on the same sublattice.

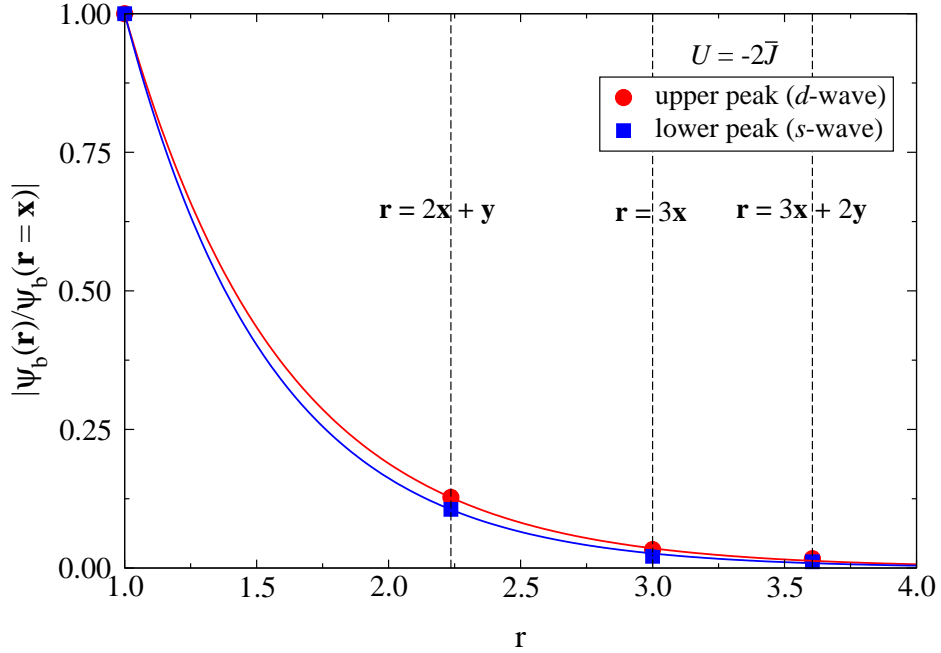


Figure 4.9: Relative amplitude of the upper and lower bound states for $U = -2\bar{J}$, at various distances from the impurity site. Lines are exponential fits.

These bound states exist in spite of the fact that the impurity is not lo-

4.4. The effect of the impurity

cated on the sublattice to which the quasiparticle belongs. As noted above, within a naive picture one does not expect this: the quasiparticle should not be trapped by an on-site impurity located on the other sublattice. This shows that the quasiparticle does not interact with the *bare* disorder, but with a *renormalized* one which extends to the quasiparticle's sublattice, in spite of the fact that the bare impurity is local. This is reminiscent of the renormalization of the disorder potential by electron-phonon coupling which we encountered in the last two chapters. It comes about because the quasiparticle's effective motion on one sublattice is made possible via hopping of the hole through the other sublattice, where the hole and impurity can interact. We define the effective on-site attraction as

$$U_{\text{eff}}(\mathbf{x}, \omega) = \text{Re}[\varepsilon(\mathbf{x}, \omega) - \varepsilon(\omega)]$$

which again compares the effective on-site energy near the impurity to that of sites far away from the impurity (or the clean system). This quantity is plotted in the lower panel of Fig. 4.8 for various values of U . It is finite even though there is no bare disorder at $\mathbf{r} = \mathbf{x}$. However, $U_{\text{eff}}(\mathbf{x}, \omega)$ is much weaker than U since it is an indirect effect and this explains why the binding energies for these peaks are much smaller than in the previous case. Retardation (dependence on ω) is now clearly visible, especially for the larger values of U . It is caused by the magnons accompanying the hole: in order to interact with the impurity, the hole must hop onto the other sublattice, however its ability to do so depends on the structure of the surrounding cloud of magnons. At low energies, the probability for the hole to visit the impurity is further suppressed due to the energy cost associated with the magnons generated during hopping. This explains why U_{eff} becomes weaker at these energies. A similar effect has been predicted for hole-doped CuO ladders with non-magnetic impurities that affect the propagating holes even if they do not lie in their path [87].

Perturbation theory to zero order in t suggests that there should be a finite threshold for U in order for bound states to appear. It can be estimated by comparing the hole's energy at any other site in the lattice, $4\bar{J} + \mathcal{O}(t^2)$, to its minimum energy at the impurity site, $10\bar{J} - U + \mathcal{O}(t^2)$ (the increased energy is due to the presence of at least one spin defect). If $U < 6\bar{J}$, this implies that it should not be energetically favorable for the hole to be at the impurity site. Including corrections proportional to t^2 does not change this and a finite threshold value is still predicted. However, we do not find any such threshold in the full calculation. This emphasizes again the importance of the (higher-order) loop processes in describing the actual behavior.

4.4. The effect of the impurity

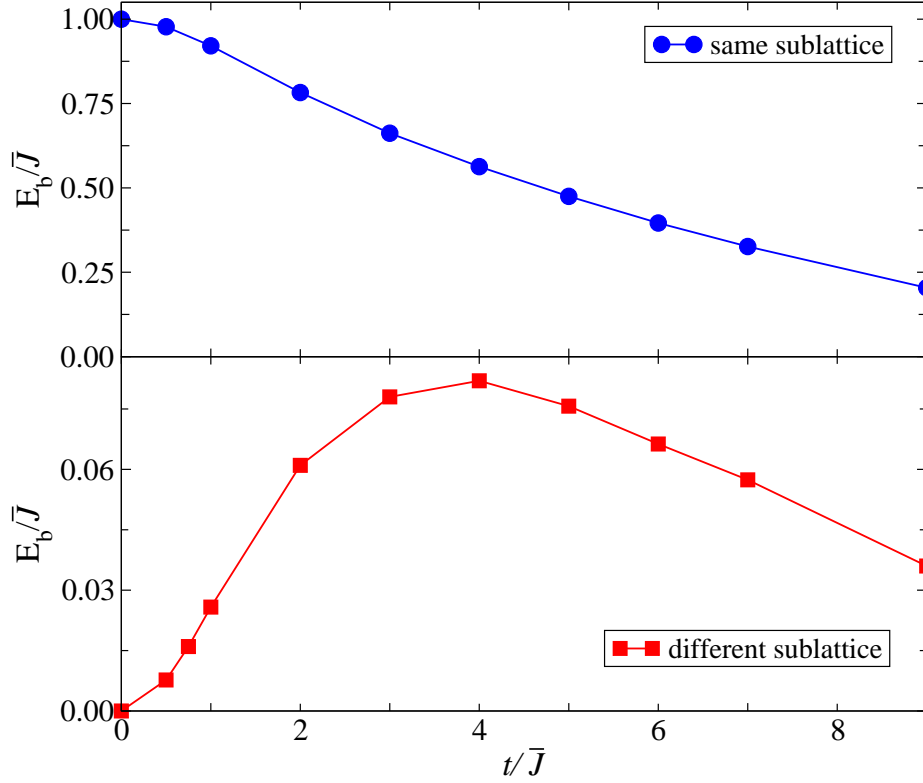


Figure 4.10: Binding energy of the s -wave bound state at $U = -\bar{J}$ vs. t/\bar{J} , when the quasiparticle and the impurity are on the same sublattice (top panel) and different sublattices (bottom panel). The smaller binding energy at strong hopping is due to the reduction in the quasiparticle's effective mass, which makes it harder to trap. When the quasiparticle and the impurity are on different sublattices, the enhancement of U_{eff} at small t dominates over the effective mass decrease, explaining the growth of the binding energy here.

Fig. 4.8 shows that a total of three bound states emerge upon increasing the impurity attraction U . Further increase of U increases their binding energy, but it does not give rise to more bound states. One can identify the nature of each bound state by comparing its amplitudes on the four neighboring sites of the impurity, $\langle \mathbf{r} = \mathbf{u} | \psi_b \rangle$. These are extracted from $G_{\mathbf{x}, \mathbf{u}}(\omega = E_b)$, just as we did in Eq. (4.24). For the lower peak, we find the same value of $\langle \mathbf{u} | \psi_b^1 \rangle$ for all \mathbf{u} , implying s -wave symmetry. A state with s -wave symmetry is expected to have the strongest binding to the

4.4. The effect of the impurity

impurity since, to the leading order in hopping, all of its four segments meet constructively on the impurity. For the upper peak, $\langle \mathbf{x} | \psi_b^3 \rangle = -\langle \mathbf{y} | \psi_b^3 \rangle = \langle -\mathbf{x} | \psi_b^3 \rangle = -\langle -\mathbf{y} | \psi_b^3 \rangle$, i.e., this state has d -wave symmetry. The middle state has p_x symmetry: $\langle \mathbf{x} | \psi_b^2 \rangle = -\langle -\mathbf{x} | \psi_b^2 \rangle$ and $\langle \mathbf{y} | \psi_b^2 \rangle = \langle -\mathbf{y} | \psi_b^2 \rangle = 0$. It has a degenerate twin bound state with p_y symmetry, which has zero amplitude at $\mathbf{r} = \mathbf{x}$ and therefore it does not appear in $\rho(\mathbf{x}, \omega) \propto \text{Im}G_{\mathbf{x}, \mathbf{x}}(\omega)$. Since the full lattice has rotational symmetry about the impurity, the resulting bound states are expected to mirror this symmetry as well. The spatial profile of s - and d -wave states is presented in Fig. 4.9. It shows that they have very similar decay lengths, consistent with their fairly similar binding energies and with the fact that their corresponding peaks in Fig. 4.8 have similar quasiparticle weights. The p_x state, however, is expected to have about twice larger weight as it is distributed between only \mathbf{x} and $-\mathbf{x}$ lobes, whereas the s and d states have equal weights in all four directions. Again, this is consistent with its spectral weight shown in Fig. 4.8.

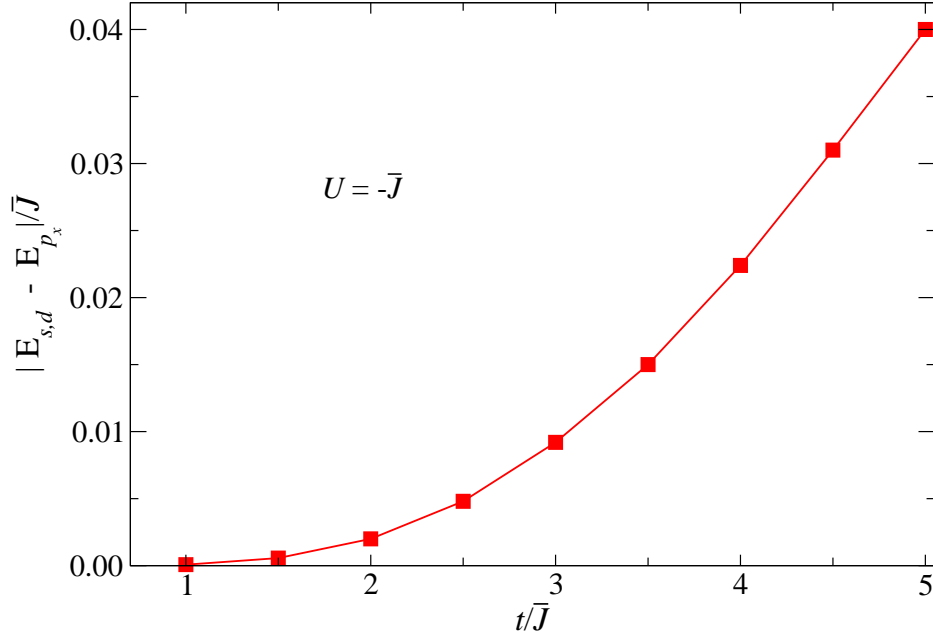


Figure 4.11: The gap between the p_x and either of the s or d states, for a fixed U . Its enhancement as a function of t/\bar{J} reflects the rotational kinetic energy gain of the quasiparticle as it becomes lighter with increasing t .

Fig. 4.10 shows the binding energy E_b of the s -wave state as a function of hopping t , when $U = -\bar{J}$. It exhibits quite different trends in the two cases.

As the hopping becomes stronger, the kinetic energy of the quasiparticle is increased (its effective mass decreases). A lighter quasiparticle is harder to trap and this explains why its binding energy at fixed U gets weaker when it is on the same sublattice with the impurity (top panel).

When the quasiparticle is on the other sublattice (bottom panel), it interacts with the impurity by virtue of U_{eff} which is dynamically generated and therefore strongly depends on t . At $t = 0$, the hole is locked at a lattice site and is unaware of the presence of impurity, therefore $E_b = 0$. As t is increased, U_{eff} is enhanced as the hole is able to visit the impurity, whereas the quasiparticle's effective mass is reduced as it gains more kinetic energy. The former tends to increase the binding energy while the latter reduces it, and it is their competition that sets the dependence of binding energy on the hopping, t . The initial growth of E_b implies that the enhancement of U_{eff} dominates over the reduction of effective mass at small t . However, since U_{eff} is weaker than U for all t (Fig. 4.8), further increase of the hopping makes the hole too light to be easily trapped by U_{eff} and the binding energy eventually starts to decrease. While only the binding energy of the s -wave state is shown in the lower panel of Fig. 4.10, all three peaks exist for small t , although they are energetically very close to each other. With increasing t they move closer to and eventually merge into the continuum such that, at the highest value of t in Fig. 4.10, the s -wave state is the only existing bound state.

The energy gaps between the three bound states (when all are present) are nearly identical. Figure 4.11 shows its evolution with t when $U = -\bar{J}$. Since this must be due to differences in the rotational kinetic energy, it is expected to increase with t , as the quasiparticle's effective mass decreases. This is indeed the observed behavior.

4.5 Summary and conclusions

We investigated the effect of a non-magnetic impurity on the motion of a hole in a 2D square Ising AFM. The resulting quasiparticle, which propagates on one sublattice, is confirmed to form bound states around the impurity. This is true both when the hole and impurity are on the same sublattice and when they are on different ones. The latter occurs because of the renormalization of the effective on-site energy which results in finite effective attraction at the sites next to the impurity that can be visited by the quasiparticle. This also explains why a total of (up to) three bound states with s , p , and d symmetries were found in this case, as opposed to only one s -wave state in

4.5. Summary and conclusions

the case when the quasiparticle is on the same sublattice with the impurity. In this latter case, the impurity is located in the node of p and d symmetry states, therefore such states do not see it and can not be bound to it (In reality, U_{eff} at sites other than those occupied by the impurity is non-zero, but given their longer distance to the impurity site, it is not large enough to bind new states).

Bound states with s , p , and d symmetries have also been observed near an inert vacancy in a Heisenberg AFM. However, in that case, it is the distortion of the magnetic environment around the vacancy that binds the hole [77, 78]. Such a distortion is only possible in a Heisenberg model and comes from a local modification of the spin fluctuations. In an Ising AFM, an inert site would have no effect on the AFM order of the other sites. Moreover, if the hole is not allowed to visit this inert impurity site, there are no Trugman loops including it so the hole loses kinetic energy when located in that neighborhood. As a result, we expect that in an Ising AFM, an inert impurity like that of Ref. [77] would repulse the hole. Bound states could only appear if a sufficiently strong exchange was turned on between the hole and the inert spin, so that the exchange energy gained through it compensates for the loss of kinetic energy. Such a model was analyzed in Ref. [78], although for the Heisenberg model it was found that bound states persist only if this exchange with the inert site is rather weak. All these differences show that the underlying reasons for the appearance of bound states are very different in these other models. This is further substantiated by the fact that while a sublattice dependence is observed in Refs. [77, 78], it consists of a variation of the spectral weight but this is associated with the same eigenstates. By contrast, in our model, the two sublattices show different spectra of bound states.

This result is important because it suggests that two very different patterns of bound states should be observed with scanning tunneling microscopy (STM) in such systems, even if only one type of impurity is present. Note that we assumed that the impurity is located directly at (or above) a lattice site. If, on the other hand, the impurity was located either half-way between two sites or in the center of the plaquettes (such as in the case of strontium dopings in $\text{La}_{2-x}\text{Sr}_x\text{CuO}_4$ superconductor), then it would not break the symmetry between the two sublattices and only one pattern of bound states should appear. These cases can be studied by similar means as presented here.

A major simplifying factor of this problem was the assumption of an Ising AFM. If spin fluctuations are turned on, in a Heisenberg AFM, a major difference is that the hole no longer needs to go twice around closed

loops in order to become delocalized: spin fluctuations can remove pairs of neighboring magnons, thus cutting the string short and releasing the hole. As a result, one expects a significant decrease in the effective mass of the quasiparticle, which is indeed observed [88]. However, it is interesting to note that if there is true long-range AFM order in the plane (as is the case in cuprates, due to coupling between planes), the resulting quasiparticle should continue to primarily reside on one sublattice, because spin fluctuations can only remove/create *pairs* of magnons and spin conservation would continue to make the two sublattices inequivalent. This suggests that the results we present here, which are directly traceable to the fact that the quasiparticle lives on one sublattice, could be relevant for the Heisenberg AFM as well, although it is impossible to say *a priori* if the effective attraction generated when the quasiparticle and impurity are on different lattices would suffice to bind states (we would still expect *s*-symmetry bound states to appear if the quasiparticle and impurity are on the same sublattice).

In the broader context, these results confirm the view that coupling to bosonic degrees of freedom renormalizes not just a quasiparticle's dispersion, but also the effective disorder it sees. If the latter were not the case, no bound states could arise when the quasiparticle lives on a difference sublattice than the impurity. Similar situation for the Holstein polarons has been thoroughly discussed in the previous two chapters, where coupling to lattice phonons results in a non-trivial renormalization of the disorder potential seen by the quasiparticle.

Chapter 5

Accurate variational solution for a hole doped in a CuO_2 layer

5.1 Introduction

After more than two decades from their discovery, cuprate high- T_c superconductors have eluded a comprehensive explanation. All these layered materials contain CuO_2 layers which, in the absence of doping, are antiferromagnetic Mott insulators. It is now widely believed that the superconductivity in cuprates arises when the additional charge carriers are doped into these layers [69, 70]. The hole-doped superconductivity is the more interesting one: it leads to a robust superconductivity that extends over a wide range of dopings, it has the highest T_c at optimal doping, while on the underdoped side a pseudo-gap phase clearly shows up at higher temperatures, with intriguing properties. The first step towards deciphering the mechanism of superconductivity in these compounds is a proper description of the motion of a hole in CuO_2 layer [64–68]. This elucidates the nature of quasiparticles that, at finite doping concentration, will bind together and condense into the superconducting state.

Modern theoretical studies of this problem have been generally based on a three-band $p-d$ model [89] whose unit cell includes two O $2p_{x/y}$ and a Cu $3d_{x^2-y^2}$ orbital, Fig. 5.5(a). Because of reasons that are outlined in the next section, the doping hole tends to mainly reside on O's and only visits the Cu sites by doing virtual hops. At low energies, however, it was proposed that this hole is locked into a singlet state with Cu holes. It can reduce its energy by making virtual hops onto the Cu's provided that it is in a certain linear combination of surrounding O $2p$ orbitals that respects the $3d_{x^2-y^2}$ symmetry of the central Cu orbital. This effectively reduces the multi-band problem to a one-band t - J model for the hole-Cu singlet, also known as the Zhang-Rice singlet [36, 90]. We studied the Ising limit

of this one-band model in chapter 4. The full problem, including the spin fluctuations, can only be solved numerically for finite size systems and this counteracts the apparent simplification associated with the smaller Hilbert space of the effective one-band treatment [91–96].

In this chapter I return to the multi-band model, and devise a variational scheme for calculating the spectral properties of a single hole doped into a CuO_2 layer. This will be based on an effective model introduced in Ref. [3], which was solved via exact diagonalization for finite size clusters. Instead, the variational principle, with some approximations, enables studying an infinite system and is therefore free of finite-size effects.

Sec. 5.2 summarizes the electronic configuration and discusses the multi-band model of the hole-doped CuO_2 layer. The variational solution of that model is then constructed in Sec 5.3. The quasiparticle dispersion and effect of various terms in the Hamiltonian on it, along with the quasiparticle weights are studied in Sec. 5.4 and 5.5. A comparison of our polaron solution and the Zhang-Rice singlet is the subject of Sec. 5.6. Finally, a five-band generalization of this model which includes both in-plane $2p$ orbitals, and its effect on the quasiparticle’s spectral properties, are discussed in Sec. 5.7.

5.2 Three-band model for a cuprate layer and its t - J analogue

The first step in describing the motion of a hole doped into a CuO_2 layer is to understand the electronic configuration of the undoped system. In this compound, the copper cations and oxygen anions are arranged into two intertwined square lattices, Fig. 5.5(a), and have the following electronic configuration

$$\begin{aligned} \text{Cu}^{2+} &: 1s^2 2s^2 2p^6 3s^2 3p^6 3d^9, \\ \text{O}^{2-} &: 1s^2 2s^2 2p^6. \end{aligned}$$

O’s have therefore a closed shell, while there is a single unpaired $3d$ -electron (or a hole) on each Cu ion. Within the three-dimensional crystal structure, coppers are located at the center of an octahedral arrangement of six O ions, with the two apical ones belonging to nearby layers, Fig 5.1(a). The energy levels of Cu in this geometry are shown in Fig. 5.1(b). The crystal field of the surrounding O ligands splits five Cu $3d$ orbitals into a lower t_{2g} group including $3d_{xy}$, $3d_{yz}$ and $3d_{xz}$ orbitals, and a higher e_g group of $3d_{x^2-y^2}$ and $3d_{3z^2-r^2}$ orbitals that directly point towards the ligands. With nine $3d$ -electrons, this results in an energy degenerate configuration for Cu where

5.2. Three-band model for a cuprate layer and its t - J analogue

three electrons are left to occupy four e_g states. In fact, the octahedron undergoes a tetragonal distortion in order to reduce its energy by removing this degeneracy, with the in-plane ligands moving towards the Cu. This opens up a gap between the two e_g (and within the three t_{2g}) orbitals [97] and makes $3d_{x^2-y^2}$ the only partially occupied $3d$ orbital, Fig. 5.1(b).

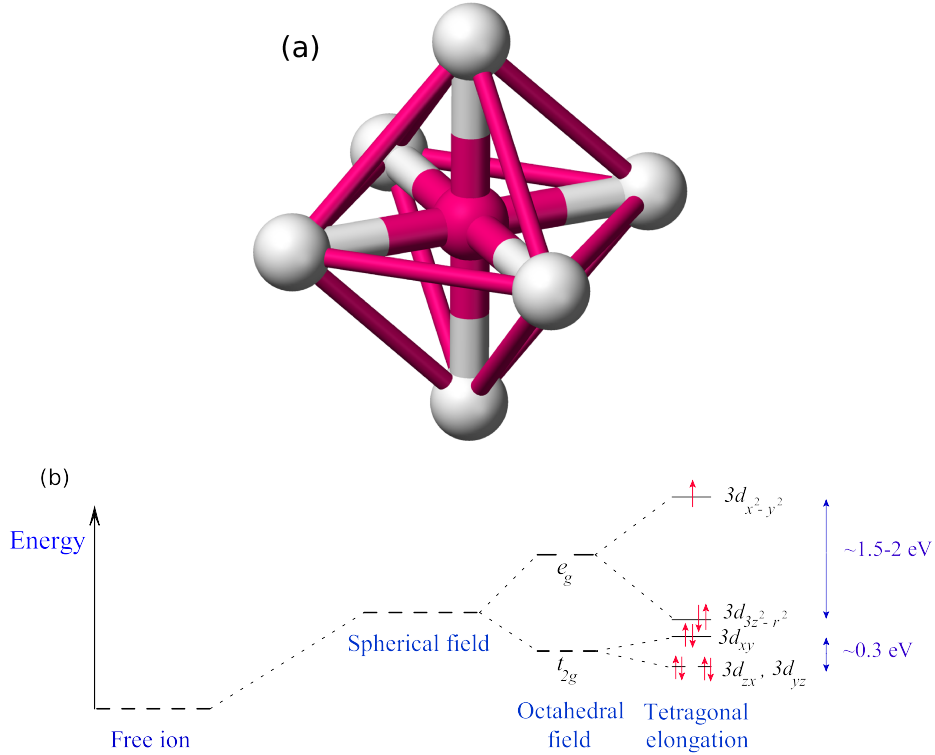


Figure 5.1: (a): Cu, shown in red, is surrounded by six O ligands in octahedral geometry. The static electric field of these ligands partially removes the degeneracy of Cu $3d$ orbitals into e_g and t_{2g} manifolds. This degenerate configuration distorts to remove the remaining degeneracies and ends up having $3d_{x^2-y^2}$ as its highest partially-occupied orbital, (b). The values of splittings for La_2CuO_4 are given. In the case of $\text{Sr}_2\text{CuO}_2\text{Cl}_2$, splitting within e_g is such strong that $3d_{3z^2-r^2}$ orbital is pushed below the entire t_{2g} manifold.

Due to strong hybridization between $2p_{x,y}$ and $3d_{x^2-y^2}$ orbitals, there is a considerable hopping amplitude, t_{pd} , between neighbouring O's and Cu's. The electronic structure of O and Cu ions in the CuO_2 layer is such

5.2. Three-band model for a cuprate layer and its t - J analogue

that the energy of electrons in doubly-occupied $2p$ orbitals of O's is higher by $E_{pd} = E_p - E_d > 0$ compared to that in the singly-occupied $3d_{x^2-y^2}$ orbitals⁴, Fig. 5.2(a). Therefore, the lowest-energy charge excitation in the layer happens between O's and Cu's and costs what is known as the charge-transfer energy $\Delta_{pd} = U_{dd} - E_{pd}$, where U_{dd} is the Hubbard interaction in $3d_{x^2-y^2}$ orbital. Since $\Delta_{pd} > 0$, charge fluctuations are suppressed at low energies and the system becomes an electrical insulator, also known as charge-transfer insulator [98] to distinguish them from Mott insulators where the lowest charge excitation happens between Cu's themselves ($E_{pd} < 0$), Fig. 5.2(b). Nevertheless, virtual hopping of the Cu holes onto O's gives rise to antiferromagnetic superexchange interaction between nearest-neighbour (nn) Cu spins

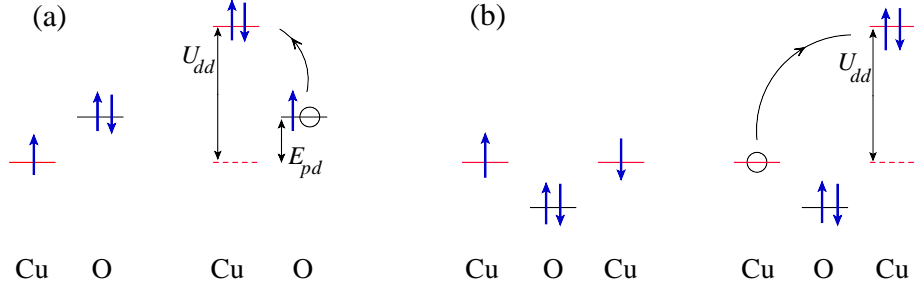


Figure 5.2: (a) The ground state of charge-transfer insulator (left) and its lowest excitation (right) Δ_{pd} higher in energy. \uparrow and \downarrow represent electrons and \circ stands for a hole (electron representation). (b) In a Mott insulator, however, charge excitation with the lowest energy corresponds to an electron moving from one Cu to another at an energy cost of U_{dd} .

$$\mathcal{H}_{J_{dd}} = J_{dd} \sum_{\langle i,j \rangle} \mathbf{S}_i \cdot \mathbf{S}_j, \quad (5.1)$$

in which \mathbf{S}_i is the spin- $\frac{1}{2}$ operator for the hole at Cu site i and J_{dd} is the strength of the superexchange coupling. It is a fourth-order process in t_{pd} as illustrated in Fig. 5.3,

$$J_{dd} \sim \frac{t_{pd}^4}{\Delta_{pd}^2(2\Delta_{pd} + U_{pp})},$$

⁴The difference in the Madelung potential of Cu and O sites is another factor contributing to this.

5.2. Three-band model for a cuprate layer and its t - J analogue

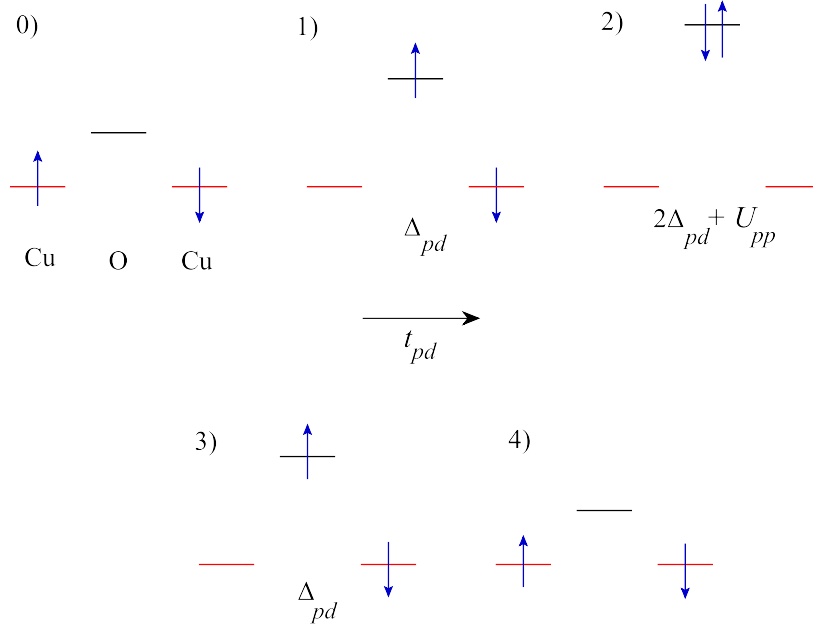


Figure 5.3: One set of processes giving rise to the superexchange coupling, J_{dd} , between two neighbouring Cu holes. Arrows represent the holes and empty O levels corresponds to them being doubly-occupied with electrons (hole notation). The energies of intermediate configurations are given.

where U_{pp} is the Hubbard repulsion between two Cu holes on the same O $2p$ orbital⁵.

Note that the ground state of this Hamiltonian is not the simple classical Néel-ordered state. The quantum fluctuations, $J_{dd}/2(S_i^- S_j^+ + S_i^+ S_j^-)$, smear out the Néel state by flipping pairs of spins, giving rise to spin fluctuations that are sometimes modelled using linear approximations [99]. Exact treatment is only possible numerically for finite size systems [71]. Here, we make a key simplification of replacing the full Heisenberg Hamiltonian with its Ising counterpart whose ground state, $|N\rangle = |\uparrow, \downarrow, \uparrow, \dots\rangle$, is Néel-ordered and has no spin fluctuations

$$\mathcal{H}_{J_{dd}} = J_{dd} \sum_{\langle i,j \rangle} S_i^z S_j^z. \quad (5.2)$$

This will enable us to set up a semi-analytic calculation of a doped hole's

⁵Note that there is a weak correction to this J_{dd} ($\propto 1/U_{dd}$) due to processes involving double-occupancy of Cu, which are neglected in this work.

dynamics in the layer for an essentially infinite system. We will justify the validity of this approximation based on the results it leads to.

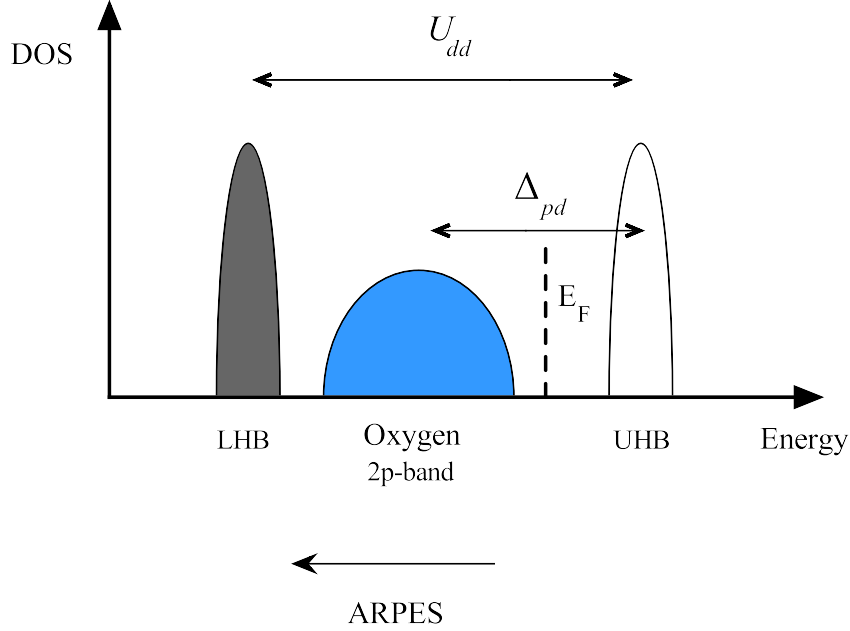


Figure 5.4: Energy diagram of the undoped CuO_2 layer, illustrating a charge-transfer insulator. The filled bands are shaded, above them lies the Fermi energy in the gap. Since $\Delta_{pd} < U_{dd}$, removing electrons created holes on O's rather than on Cu's and this moves the Fermi energy into the O $2p$ -band.

5.2.1 Doping the CuO_2 layer with a hole

Whereas the CuO_2 layer is an insulator at half-filling, it becomes conducting upon doping which moves the Fermi energy into either the upper Hubbard band (electron doping - inverse photoemission) or the O $2p$ -band (hole doping - photoemission), Fig. 5.4. This picture is supported by various spectroscopic studies [100] suggesting that holes primarily reside on O's rather than on Cu's. By doing so, the system can avoid the large Hubbard repulsion $U_{dd} (> U_{pp} > \Delta_{pd})$ between two holes on the same Cu $3d_{x^2-y^2}$ orbital. Assuming $U_{dd} \rightarrow \infty$ and projecting out configurations involving charge fluctuation between Cu's and O's (of order Δ_{pd}), one arrives at the following

5.2. Three-band model for a cuprate layer and its t - J analogue

effective Hamiltonian for the CuO_2 layer with a single hole [3]

$$\begin{aligned}\mathcal{H} &= J_{dd} \sum_{\langle i,j \rangle'} S_i^z S_j^z + \hat{T}_{pp} + \mathcal{H}_{J_{pd}} + \hat{T}_{\text{swap}} \\ &\equiv \mathcal{H}_{J_{dd}} + \mathcal{H}_1,\end{aligned}\quad (5.3)$$

where the prime indicates the lack of exchange coupling between the pair of coppers that have the doping hole on the bridging O and the spin fluctuations of Cu holes are neglected. Note that in reality the first term has to be the Heisenberg interaction, but we have applied the simplification suggested before in Eq. (5.2). \hat{T}_{pp} is the tight-binding Hamiltonian with the nearest-neighbour (nn), t_{pp} , and Cu-bridged next nn hopping, t'_{pp} , and describes the kinetic energy of the hole as it propagates among O $2p_{x/y}$ orbitals, whose relative phases determine the sign of these hoppings

$$\hat{T}_{pp} = t_{pp} \sum_{\mathbf{R},\sigma} r_{\delta} p_{\mathbf{R},\sigma}^{\dagger} p_{\mathbf{R}+\delta,\sigma} - t'_{pp} \sum_{\mathbf{R},\sigma} p_{\mathbf{R},\sigma}^{\dagger} (p_{\mathbf{R}-\varepsilon,\sigma} + p_{\mathbf{R}+\varepsilon,\sigma}). \quad (5.4)$$

Here, $p_{\mathbf{R},\sigma}^{\dagger}$ creates a hole with spin σ on the O ligand $2p$ orbital located at \mathbf{R} . δ and ε are the nn and next nn vectors. $r_{\delta} = \pm 1$ sets the signs of nn hoppings in accordance with the phases of $2p$ orbitals involved, see Fig 5.5(a). The next term, $\mathcal{H}_{J_{pd}}$, describes the antiferromagnetic exchange coupling between the doping hole, $\mathbf{s}_{\mathbf{R}}$, and its two neighbouring coppers at site i :

$$\mathcal{H}_{J_{pd}} = J_{pd} \sum_{\langle i,\mathbf{R} \rangle} \mathbf{s}_{\mathbf{R}} \cdot \mathbf{S}_i. \quad (5.5)$$

Unlike $\mathcal{H}_{J_{dd}}$, we treat this term as a full Heisenberg Hamiltonian. Finally, \hat{T}_{swap} is an additional effective kinetic energy term which describes the motion of the hole between O sites that is mediated by the transfer of a Cu hole, without involving double-occupancy of Cu. Fig. 5.5(c) shows how this can give rise to nn and next nn hopping between O, with the same effective hopping $t_s \sim t_{pd}^2/\Delta_{pd}$: first, the Cu hole hops onto one of its empty neighbouring O orbitals, then the doping hole fills the empty Cu orbital. Note that this results in swapping the spin of the two holes. The explicit form of this Hamiltonian is then as follows

$$\hat{T}_{\text{swap}} = -t_s \sum_{\mathbf{R},\eta} s_{\eta} p_{\mathbf{R},\sigma}^{\dagger} p_{\mathbf{R}+\eta,\sigma'} |\sigma'\rangle \langle \sigma|, \quad (5.6)$$

where $|\sigma\rangle$ refers to the state of Cu spins and prime reflects the possibility of spin flip during the hop; $s_{\eta} = \pm 1$ determines the sign of each nn or next

5.2. Three-band model for a cuprate layer and its t - J analogue

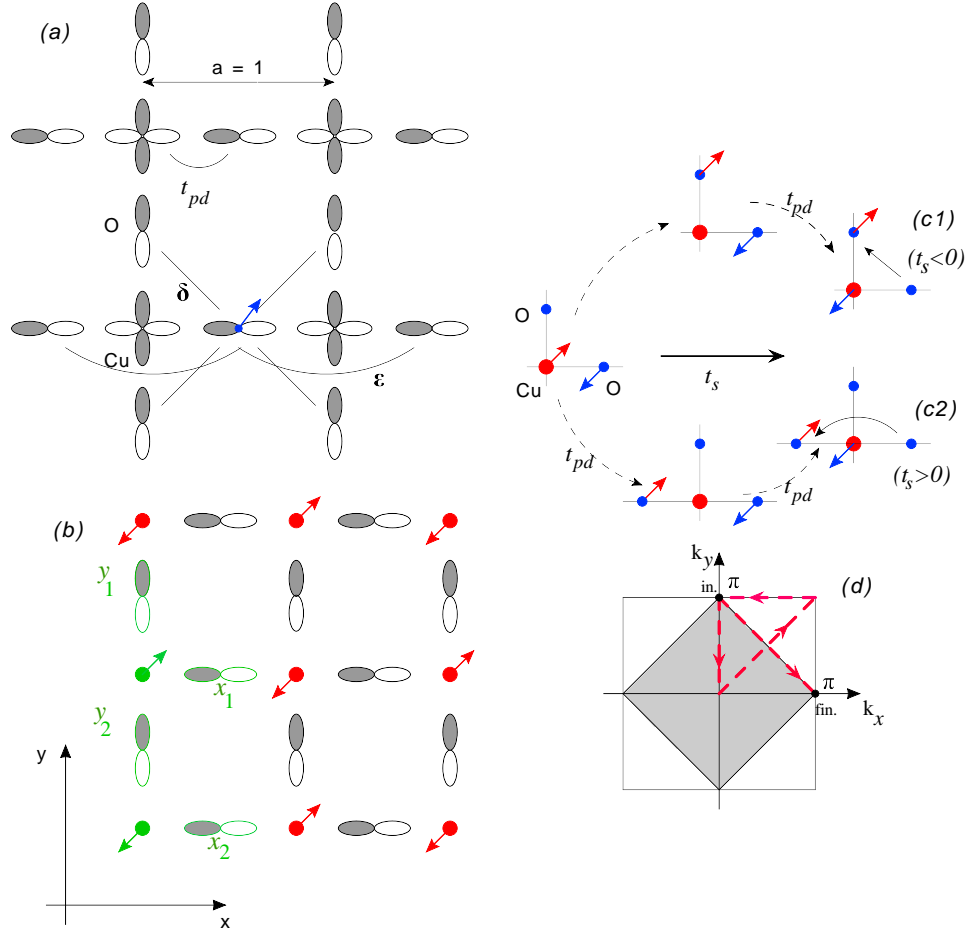


Figure 5.5: (a): The CuO_2 layer with the spin-up hole occupying one of the O $2p$ orbitals. nn (δ) and next nn hops (ϵ) between O's that are considered in our model are shown. For the hole, nn hopping is negative along $y = x$ direction where $2p$ orbitals have their lobes with similar phases pointing towards each other and positive along $y = -x$. (b): Cu and O ions that make the unit cell are shown in green. (c): Processes that give rise to nn (c1) and next nn (c2) spin-swap. (d): The full Brillouin zone of the CuO_2 lattice (the outer square) which encloses the magnetic Brillouin zone (shaded). We study the quasiparticles with momenta lying along the dashed red line, starting from $(0, \pi)$ and ending at $(\pi, 0)$.

nn hop according to the sign of $3d$ and $2p$ orbitals involved, Fig. 5.5(c). If

they had opposite spin directions, swapping flips the Cu spin and creates a localized magnon (a spin defect). Note that J_{pd} can also generate a magnon, but it differs from \hat{T}_{swap} in that it does not involve the motion of the O hole.

Hamiltonian (5.3) is reminiscent of the strong coupling limit of Hubbard model, namely the t - J Hamiltonian. The values of hopping parameters are determined via tight-binding fittings to LDA band structure calculations, whereas the Hubbard repulsions are estimated from cluster calculations compared with various spectroscopic measurements [101]. As a result, there are no free fitting parameters. Given in units of J_{dd} ($\approx 0.10 - 0.15$ eV), the dimensionless parameters are $t_{pp} = 4.13$, $t_s = 2.98$, $J_{pd} = 2.83$ and $t'_{pp} = 0.58t_{pp}$. For complete technical details regarding the derivation of Hamiltonian (5.3) and further discussions, the reader is referred to Bayo Lau's thesis [102].

5.3 Green's functions

In this section, we calculate various Green's functions (GF) describing the propagation of the hole between O sites at zero temperature. The unit cell is shown in Fig. 5.5(b). Because of the underlying Néel order, it contains two distinct Cu atoms (spin-up, spin-down) and therefore four different O. For each O, it is common to take into account only the ligand $2p$ orbital that hybridizes with the $3d_{x^2-y^2}$ orbitals of Cu and this is what we also do in this section. Although this proves to be sufficient as far as the dispersion relations are concerned, we later extend our analysis to include the other in-plane $2p$ orbital when we study the hole's quasiparticle weight.

The single-hole Green's functions are defined as

$$G_{\alpha\beta}(\mathbf{k}, \omega) = \langle N | h_{\mathbf{k},\alpha,\uparrow} \hat{G}(\omega) h_{\mathbf{k},\beta,\uparrow}^\dagger | N \rangle,$$

where $\hat{G}(\omega) = \lim_{\eta \rightarrow 0^+} 1/(\omega - \mathcal{H} + i\eta)$ is the resolvent of the Hamiltonian. $h_{\mathbf{k},\alpha,\uparrow}^\dagger$ creates a spin-up hole in Bloch states made out of O $2p_\alpha$ orbitals

$$h_{\mathbf{k},\alpha,\uparrow}^\dagger = \frac{1}{\sqrt{N}} \sum_{\mathbf{R}_\alpha} e^{i\mathbf{k} \cdot \mathbf{R}_\alpha} p_{\mathbf{R}_\alpha,\uparrow}^\dagger, \quad (5.7)$$

in which N is the number of unit cells, $p_{\mathbf{R}_\alpha,\uparrow}^\dagger$ creates a spin-up hole at O $2p_\alpha$ orbital located at \mathbf{R}_α and $\alpha = p_{x_1}, p_{x_2}, p_{y_1}, p_{y_2}$ are the distinct O $2p$ orbitals in the unit cell, see Fig. 5.5(b). The quasi-momentum \mathbf{k} belongs to the magnetic Brillouin zone (MBZ), the shaded area in Fig. 5.5(d), which

5.3. Green's functions

includes all unique momenta in the reciprocal lattice. These sublattice GFs are useful since their poles correspond to the hole's energy dispersion, $E_n(\mathbf{k})$, and the associated residues give the overlap between the true eigenstates and the single-particle Bloch states, $Z(\mathbf{k}) = |\langle N | h_{\mathbf{k},\alpha,\uparrow} | \psi_{n,\mathbf{k}} \rangle|^2$.

5.3.1 One-magnon approximation

The equations of motion for $G_{\alpha\beta}(\mathbf{k}, \omega)$ can be written using the Dyson identity based on the separation suggested in Eq. (5.3),

$$\hat{G}(\omega) = \hat{G}_{dd}(\omega) + \hat{G}(\omega) \mathcal{H}_1 \hat{G}_{dd}(\omega). \quad (5.8)$$

With four different p orbitals, there are a total of 16 different Green's function. For $\beta = p_{x_1}$, we have

$$G_{\alpha,p_{x_1}}(\mathbf{k}, \omega) = g_0(\omega) [\delta_{\alpha,p_{x_1}} + \langle \mathbf{k}, \alpha, \uparrow | \hat{G}(\omega) \mathcal{H}_1 | \mathbf{k}, p_{x_1}, \uparrow \rangle], \quad (5.9)$$

where $g_0(\omega) = 1/(\omega - J_{dd}/4 + i\eta)$, $J_{dd}/4$ is energy cost of breaking a superexchange bond by the doping hole and $|\mathbf{k}, p_{x_1}, \uparrow\rangle = h_{\mathbf{k},p_{x_1},\uparrow}^\dagger |N\rangle$. \mathcal{H}_1 takes the hole from the $2p_{x_1}$ orbital to other $2p$ orbitals at its vicinity, during which its spin can also be flipped and a magnon is created

$$\begin{aligned} \mathcal{H}_1 p_{\mathbf{R}_{p_{x_1}}, \uparrow}^\dagger |N\rangle &= t_s [-p_{\mathbf{R}_{p_{x_1} + \mathbf{x}/2 + \mathbf{y}/2, \downarrow}}^\dagger |S'\rangle + p_{\mathbf{R}_{p_{x_1} + \mathbf{x}/2 - \mathbf{y}/2, \downarrow}}^\dagger |S'\rangle \\ &\quad - p_{\mathbf{R}_{p_{x_1} + \mathbf{x}, \downarrow}}^\dagger |S'\rangle] + \frac{J_{pd}}{2} p_{\mathbf{R}_{p_{x_1}, \downarrow}}^\dagger |S'\rangle \\ &\quad + t_s [p_{\mathbf{R}_{p_{x_1} - \mathbf{x}/2 + \mathbf{y}/2, \uparrow}}^\dagger |N\rangle - p_{\mathbf{R}_{p_{x_1} - \mathbf{x}/2 - \mathbf{y}/2, \uparrow}}^\dagger |N\rangle \\ &\quad - p_{\mathbf{R}_{p_{x_1} - \mathbf{x}, \uparrow}}^\dagger |N\rangle] + t_{pp} [p_{\mathbf{R}_{p_{x_1} + \mathbf{x}/2 + \mathbf{y}/2, \uparrow}}^\dagger |N\rangle \\ &\quad + p_{\mathbf{R}_{p_{x_1} - \mathbf{x}/2 - \mathbf{y}/2, \uparrow}}^\dagger |N\rangle - p_{\mathbf{R}_{p_{x_1} - \mathbf{x}/2 + \mathbf{y}/2, \uparrow}}^\dagger |N\rangle \\ &\quad - p_{\mathbf{R}_{p_{x_1} + \mathbf{x}/2 - \mathbf{y}/2, \uparrow}}^\dagger |N\rangle] - t'_{pp} [p_{\mathbf{R}_{p_{x_1} + \mathbf{x}, \uparrow}}^\dagger |N\rangle \\ &\quad + p_{\mathbf{R}_{p_{x_1} - \mathbf{x}, \uparrow}}^\dagger |N\rangle], \end{aligned} \quad (5.10)$$

where the distance between neighbouring copper atoms is taken to be unity (\mathbf{x} and \mathbf{y} are unit vectors) and $\mathbf{s} \cdot \mathbf{S} = s^z S^z + (s^+ S^- + s^- S^+)/2$ is used. $|S'\rangle$ is the state of Cu spins where the spin-down Cu next to the hole is flipped:

5.3. Green's functions

$|S'\rangle = S_{\mathbf{R}_{p_{x_1} + \mathbf{x}/2}}^+ |N\rangle$. Using this in the last matrix element in Eq. (5.9) gives

$$\begin{aligned} \langle \mathbf{k}, \alpha, \uparrow | \hat{G}(\omega) \mathcal{H}_1 | \mathbf{k}, p_{x_1}, \uparrow \rangle &= t_s [-V_1^3 + V_1^1 - V_1^2] + \frac{J_{pd}}{2} V_1^0 + t_s [e^{i(k_x - k_y)/2} \\ &\times G_{\alpha, p_{y_1}}(\mathbf{k}, \omega) - e^{i(k_x + k_y)/2} G_{\alpha, p_{y_2}}(\mathbf{k}, \omega) \\ &- e^{ik_x} G_{\alpha, p_{x_2}}(\mathbf{k}, \omega)] + 2t_{pp} [\cos((k_x + k_y)/2) \\ &\times G_{\alpha, p_{y_2}}(\mathbf{k}, \omega) - \cos((k_x - k_y)/2) G_{\alpha, p_{y_1}}(\mathbf{k}, \omega)] \\ &- 2t'_{pp} \cos(k_x) G_{\alpha, p_{x_2}}(\mathbf{k}, \omega). \end{aligned} \quad (5.11)$$

V_M^l are called one-magnon Green's functions and they describe processes

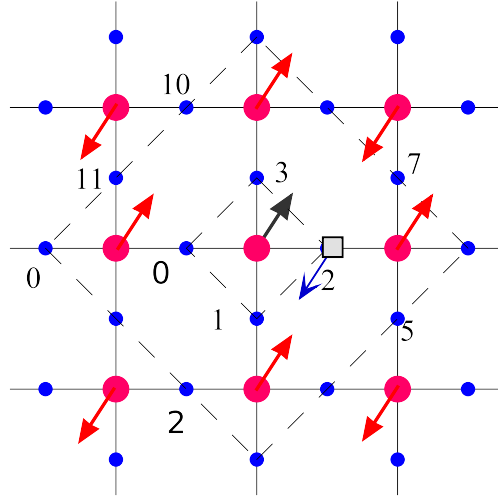


Figure 5.6: Numbering various one-magnon Green's function V_i^M at $M = 1$, 3: the one with the hole lying to the far left is $i = 0$ and the index i increases in the counterclockwise direction. The current configuration corresponds to V_1^2 .

where the spin-down hole starts at any of $4M$ O sites ($l = 0, 1, \dots, 4M - 1$) that are located at Manhattan distance of M from the magnon ($M = 1$ here). The numbering scheme is shown in Fig. 5.6. The explicit expression corresponding to V_1^3 , for example, is the following

$$V_1^3 = \frac{1}{\sqrt{N}} \sum_{\mathbf{R}_{p_{x_1}}} e^{i\mathbf{k} \cdot \mathbf{R}_{p_{x_1}}} \langle N | h_{\mathbf{k}, \alpha \uparrow} \hat{G}(\omega) p_{\mathbf{R}_{p_{x_1} + \mathbf{x}/2 + \mathbf{y}/2, \downarrow}}^\dagger S_{\mathbf{R}_{p_{x_1} + \mathbf{x}/2}}^+ | N \rangle. \quad (5.12)$$

5.3. Green's functions

To generate the equation of motion for these propagators, we again use the Dyson's identity to find

$$V_1^3 = \frac{g_1(\omega)}{\sqrt{N}} \sum_{\mathbf{R}_{px_1}} e^{i\mathbf{k}\cdot\mathbf{R}_{px_1}} \langle N | h_{\mathbf{k},\alpha\uparrow} \hat{G}(\omega) \mathcal{H}_1 p_{\mathbf{R}_{px_1}+\mathbf{x}/2+\mathbf{y}/2,\downarrow}^\dagger S_{\mathbf{R}_{px_1}+\mathbf{x}/2}^+ | N \rangle, \quad (5.13)$$

where $g_1(\omega) = 1/(\omega - 7J_{dd}/4 + i\eta)$ and $7J_{dd}/4$ is the superexchange energy of state with a magnon next to the doping hole.

The swap and Cu-hole exchange interaction parts of \mathcal{H}_1 can annihilate the magnon and flip the hole's spin back to its initial direction. This relates V_1 to various $G_{\alpha,\gamma}(\mathbf{k},\omega)$. They can also link V_1 to new GFs W with two magnons, which are then related to GFs with three magnons and so on. However, creating each additional magnon increases the energy of that state by about $2J_{dd}$ as up to four Cu-Cu bonds are disturbed. Such many-magnon states are therefore energetically expensive and cannot have a significant contribution to the hole's low-energy eigenstates. Based on this, we construct a variational approximation in which we only keep states with up to a certain maximum number of magnons, n_m , and discard those including more magnons. Doing so at the one-magnon level, $n_m = 1$, gives the equation of motion for V_1 as follows

$$\begin{aligned} V_1^0/g_1(\omega) &= t_s[-e^{-i(k_x+k_y)/2}G_{\alpha,p_{y2}}(\mathbf{k},\omega) + e^{i(k_y-k_x)/2}G_{\alpha,p_{y1}}(\mathbf{k},\omega) \\ &\quad - e^{-ik_x}G_{\alpha,p_{x2}}(\mathbf{k},\omega)] + \frac{J_{pd}}{2}[G_{\alpha,p_{x1}}(\mathbf{k},\omega) - V_1^0] \\ &\quad + t_{pp}[V_3^1 + V_1^3 - V_1^1 - V_3^{11}] - t'_{pp}[V_3^0 + V_1^2], \end{aligned} \quad (5.14)$$

where several components of V_3 are introduced. Similar equations can be derived for the other three components of V_1

$$\begin{aligned} V_1^1/g_1(\omega) &= t_s[G_{\alpha,p_{x1}}(\mathbf{k},\omega) - e^{-ik_x}G_{\alpha,p_{x2}}(\mathbf{k},\omega) - e^{-i(k_x+k_y)/2}G_{\alpha,p_{y2}}(\mathbf{k},\omega)] \\ &\quad + \frac{J_{pd}}{2}[e^{i(k_y-k_x)/2}G_{\alpha,p_{y1}}(\mathbf{k},\omega) - V_1^1] + t_{pp}[V_3^2 + V_1^2 - V_1^0 - V_3^4] \\ &\quad - t'_{pp}[V_3^3 + V_1^3], \end{aligned} \quad (5.15)$$

$$\begin{aligned} V_1^2/g_1(\omega) &= t_s[-G_{\alpha,p_{x1}}(\mathbf{k},\omega) + e^{-i(k_x+k_y)/2}G_{\alpha,p_{y2}}(\mathbf{k},\omega) \\ &\quad - e^{i(k_y-k_x)/2}G_{\alpha,p_{y1}}(\mathbf{k},\omega)] + \frac{J_{pd}}{2}[e^{-ik_x}G_{\alpha,p_{x2}}(\mathbf{k},\omega) - V_1^2] \\ &\quad + t_{pp}[V_1^1 + V_3^7 - V_1^3 - V_3^5] - t'_{pp}[V_1^0 + V_3^6], \end{aligned} \quad (5.16)$$

5.3. Green's functions

$$\begin{aligned}
V_1^3/g_1(\omega) &= t_s[e^{-ik_x}G_{\alpha,px_2}(\mathbf{k},\omega) - G_{\alpha,px_1}(\mathbf{k},\omega) \\
&\quad - e^{i(k_y-k_x)/2}G_{\alpha,py_1}(\mathbf{k},\omega)] + \frac{J_{pd}}{2}[e^{-i(k_x+k_y)/2} \\
&\quad \times G_{\alpha,py_2}(\mathbf{k},\omega) - V_1^3] + t_{pp}[V_1^0 + V_3^8 - V_1^2 \\
&\quad - V_3^{10}] - t'_{pp}[V_1^1 + V_3^9]. \tag{5.17}
\end{aligned}$$

One can then generate the equation of motion for V_l^i , $l \geq 3$, in a similar way. Without allowing more magnons to be created, V_l^i 's are linked to other one-magnon GFs at Manhattan distances of $M = l - 2, l, l + 2$. Note that GFs with no magnons, $G_{\alpha,\beta}(\mathbf{k},\omega)$, do not arise here as the hole is not an immediate neighbour of the magnon and cannot annihilate it by the action of \mathcal{H}_1 . The exact form of these equations depends on the $2p$ orbital from which the hole starts and it is the state of nearby Cu spins that determines which T_{swap} hoppings are allowed. For example, for V_3^4 we have

$$\begin{aligned}
\frac{V_3^4}{g_2(\omega)} &= t_{pp}[V_3^5 + V_3^3 - V_1^1 - V_5^7] - t'_{pp}[V_3^2 + V_5^8] \\
&\quad + t_s[V_5^7 - V_3^5 - V_5^8], \tag{5.18}
\end{aligned}$$

where $g_2(\omega) = 1/(\omega - 9J_{dd}/4 + i\eta)$ and $9J_{dd}/4$ is the superexchange energy of Cu holes with one magnon which is not an immediate neighbour of the doping hole. Eq. (5.18) is similar to the two-component recursive relations we encountered in the last chapter and can be solved similarly using the method of continued fractions. By collecting all one-magnon GFs at Manhattan distance l into vectors \mathbf{V}_l , the set of corresponding $4l$ equations can be expressed as a single-indexed recursive relation as follows

$$\lambda_l \mathbf{V}_l = \xi_l \mathbf{V}_{l-2} + \zeta_l \mathbf{V}_{l+2}, \quad l \geq 3 \tag{5.19}$$

where λ_l , ξ_l and ζ_l are sparse matrices. Because this relates three consecutive terms, its solution can be expressed as a continued fraction. Assuming a solution of the form $\mathbf{V}_l = A_l \mathbf{V}_{l-2}$ and using it in Eq. (5.19) results in

$$A_l = (\lambda_l - \zeta_l A_{l+2})^{-1} \xi_l. \tag{5.20}$$

This can be solved by setting A_l to zero beyond a large enough cutoff c , $A_{c+2} = 0$. In particular, it gives A_3 which relates \mathbf{V}_3 to \mathbf{V}_1 . This is then used in equations for \mathbf{V}_1 , Eq. (5.14), to reduce them into equations relating V_1^i to $G_{\alpha,\beta}(\mathbf{k},\omega)$ only

$$P\mathbf{V}_1 = \Lambda\mathcal{G}_\alpha, \tag{5.21}$$

5.3. Green's functions

where $\mathbf{V}_1 = \begin{bmatrix} V_1^0 \\ V_1^1 \\ V_1^2 \\ V_1^3 \end{bmatrix}$, $\mathcal{G}_\alpha = \begin{bmatrix} G_{\alpha,p_{x_1}} \\ G_{\alpha,p_{x_2}} \\ G_{\alpha,p_{y_1}} \\ G_{\alpha,p_{y_2}} \end{bmatrix}$ and P and Λ are some 4×4 matrices.

Using this in Eq. (5.11) we can eliminate its one-magnon GFs in favour of various $G_{\alpha,\beta}(\mathbf{k}, \omega)$. This gives the matrix element $\langle \mathbf{k}, \alpha, \uparrow | \hat{G}(\omega) \mathcal{H}_1 | \mathbf{k}, p_{x_1}, \uparrow \rangle$ as a linear combination of $G_{\alpha,\beta}(\mathbf{k}, \omega)$:

$$\langle \mathbf{k}, \alpha, \uparrow | \hat{G}(\omega) \mathcal{H}_1 | \mathbf{k}, p_{x_1}, \uparrow \rangle = \sum_{\beta} U_{p_{x_1}, \beta} G_{\alpha, \beta}(\mathbf{k}, \omega),$$

where $U_{p_{x_1}, \beta}$ is the first row of a matrix of coefficients, U . Therefore, our original equation of motion for $G_{\alpha,p_{x_1}}(\mathbf{k}, \omega)$, Eq. (5.9), takes the following form

$$\sum_{\beta} U_{p_{x_1}, \beta} G_{\alpha, \beta}(\mathbf{k}, \omega) - \frac{1}{g_0(\omega)} G_{\alpha, p_{x_1}}(\mathbf{k}, \omega) = -\delta_{\alpha, p_{x_1}}, \quad (5.22)$$

where $\alpha = p_{x_1}, p_{x_2}, p_{y_1}, p_{y_2}$. This is a set of four linear equations between sixteen Green's function, $G_{\alpha,\beta}(\omega)$. The other twelve equations are given similarly by the hole starting from $2p_{x_2}$, $2p_{y_1}$ and $2p_{y_2}$ orbitals. These are then trivially solved to give all $G_{\alpha,\beta}(\omega)$.

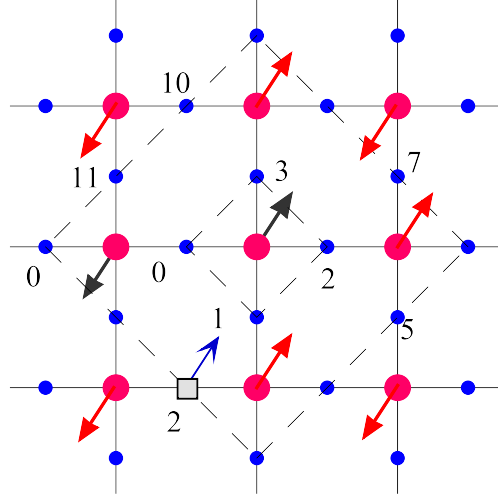


Figure 5.7: Numbering various two-magnon GFs at $M = 1, 3$. The configuration shown corresponds to W_3^2 .

5.3.2 Two-magnon approximation

The one-magnon approximation can be improved by allowing for the creation of a second magnon, i.e. working in the variational space with $n_m = 2$. In doing so, we let the second magnon be created only next to the first one and not further away. This is a good approximation for low-energy quasiparticles whose magnons are bound to the cloud. Also, this disturbs fewer antiferromagnetic bonds and therefore costs less energy compared to configurations with magnons apart. The equation of motion for V_1^0 , for example, is then modified as follows

$$\begin{aligned}
 V_1^0/g_1(\omega) &= t_s[-e^{-i(k_x+k_y)/2}G_{\alpha,py_2}(\mathbf{k},\omega) + e^{i(k_y-k_x)/2}G_{\alpha,py_1}(\mathbf{k},\omega) \\
 &\quad -e^{-ik_x}G_{\alpha,px_2}(\mathbf{k},\omega)] + \frac{J_{pd}}{2}[G_{\alpha,px_1}(\mathbf{k},\omega) - V_1^0] \\
 &\quad +t_{pp}[V_3^1 + V_1^3 - V_1^1 - V_3^{11}] - t'_{pp}[V_3^0 + V_1^2] \\
 &\quad +t_s(W_3^{11} - W_3^1 - W_3^0) + \frac{J_{pd}}{2}W_1^0,
 \end{aligned} \tag{5.23}$$

where W_l^j are two-magnon GFs in which the hole starts at Manhattan distance l from the first magnon (spin-up defect). Fig. 5.7 shows their numbering scheme. The other components of \mathbf{V}_1 are also similarly modified

$$\begin{aligned}
 V_1^1/g_1(\omega) &= \{\dots\} + t_s(W_3^1 - W_3^{11} - W_3^0) + \frac{J_{pd}}{2}W_1^0, \\
 V_1^2/g_1(\omega) &= \{\dots\} + t_s(W_3^{11} - W_3^1 - W_3^0) + \frac{J_{pd}}{2}W_1^0, \\
 V_1^3/g_1(\omega) &= \{\dots\} + t_s(W_3^1 - W_3^{11} - W_3^0) + \frac{J_{pd}}{2}W_1^0,
 \end{aligned} \tag{5.24}$$

where $\{\dots\}$ refers to those terms existing at one-magnon approximation, Eq. (5.14).

For Manhattan distances $l \geq 5$, similar continued-fraction solutions exist for both V and W : $\mathbf{V}_5 = A_5\mathbf{V}_3$ and $\mathbf{W}_5 = A'_5\mathbf{W}_3$; the prime reflects the different superexchange energy of the Cu spins with one ($9J_{dd}/4$) vs two magnons ($13J_{dd}/4$). For $l = 1$ and $l = 3$, however, various V and W are mixed together due to proximity of the hole and magnons. These linear relations,

$$\begin{aligned}
 \mathbf{V}_3 &= \mathbf{V}_3(\mathbf{V}_1, \mathbf{W}_1, \mathbf{W}_3) \\
 \mathbf{W}_1 &= \mathbf{W}_1(\mathbf{V}_1, \mathbf{V}_3, \mathbf{W}_3) \\
 \mathbf{W}_3 &= \mathbf{W}_3(\mathbf{V}_1, \mathbf{V}_3, \mathbf{W}_1),
 \end{aligned} \tag{5.25}$$

are solved for \mathbf{W}_1 , \mathbf{W}_3 and \mathbf{V}_3 in terms of \mathbf{V}_1 . This is then used to reduce Eq. (5.23) to one relating \mathbf{V}_1 and $G_{\alpha,\beta}$ only. The rest of the solution proceeds similar to the one-magnon case.

We note that the restriction of only keeping two-magnon configurations with neighbouring magnons can be easily removed, and indeed this was done in the work described in Ref. [103]. For low energy quasiparticle states, however, this leads to very minor quantitative differences.

5.4 Results

In this section, we use these Green's functions in order to extract the dispersion relation and quasiparticle weight of the hole propagating in the CuO_2 layer as a magnetic polaron. We will then gauge the importance of various terms in the Hamiltonian in controlling the generic features of these quasiparticle properties.

5.4.1 Dispersion relations

Having calculated the Green's functions, we can extract the spectral properties of the hole quasiparticle by studying the associated sublattice spectral functions,

$$A_\alpha(\mathbf{k}, \omega) = -\frac{1}{\pi} \text{Im} G_{\alpha,\alpha}(\mathbf{k}, \omega).$$

We let the quasi-momentum \mathbf{k} run over the full Brillouin zone along various cuts shown in Fig 5.5(d). The spectral weight is plotted in Fig. 5.8 in color scale as a function of \mathbf{k} and energy, ω , showing coherent bands in a wide range of energies. It is obtained within $n_m = 2$ approximation, where only the two-magnon configurations with both magnons next to each other are retained. One expects a continuum of states starting from an energy $E_{1,GS} + 2J_{dd}$, i.e., the ground state of $n_m = 1$ quasiparticle plus the energy of an unbound magnon. This is missing from Fig. 5.8, but it appears if one allows for configurations where the second magnon is away from the one-magnon polaron. This is also why the energy and location of higher energy features is tentative since multiple-magnon states contribute heavily to these higher energy eigenstates, and only after they are included is their convergence expected. As a result, from now on we focus on the lowest energy eigenstates (the quasiparticle band) which have the fastest convergence and correspond to the highest electron-removal states probed

by angle-resolved photoemission spectroscopy (ARPES)⁶.

In Fig 5.9 we compare the energy dispersion of the lowest energy band for $n_m = 1$ vs that of $n_m = 2$ approximations. These are extracted from the map plots similar to Fig. 5.8. They show essentially the same features, most notably a deep minimum at $\mathbf{k} = (\frac{\pi}{2}, \frac{\pi}{2})$ which disperses in both $k_x = \pm k_y$ directions, as observed in experiments [28]. For $n_m = 2$ the quasiparticle bandwidth is considerably narrower compared to the $n_m = 1$ case. This is indeed expected since the hole becomes an effectively heavier quasiparticle when it is bound to a bigger cloud of magnons. This also shows that configurations with two magnons have significant contribution to the polaron states as including them changes the energy dispersion quantitatively. The overall shift of $n_m = 2$ energy dispersion to lower energies is a consequence of the bigger variational space for this level of approximation.

In order to gauge the accuracy of our variational approximation, we compare it to available exact-diagonalization results for a cluster of 32 Cu of the same model [3], symbols in Fig. 5.9. It shows that the energy dispersion given by $n_m = 2$ approximation is almost converged to the exact result. This implies that configurations with more than two magnons have negligible contribution to the low-energy polaron states. Furthermore, spin fluctuations seem to have almost no effect on the hole's dispersion since they are frozen out in our approximation, but fully included in the ED calculation. In fact, spin fluctuations can bind to the doping hole to form a spin- $\frac{3}{2}$ polaron. In some parts of the BZ, ED results suggest that this spin- $\frac{3}{2}$ polaron lies energetically below our spin- $\frac{1}{2}$ polaron state [3]. However, such high-spin polaron does not appear in our model which ignores spin fluctuations.

The lack of importance of spin fluctuations in the three-band model can be understood as follows. Since the doping hole resides primarily on O ligands, it can move freely on the O sublattice by T_{pp} without being bound to magnons on the Cu's. The polaron can therefore move easily in the layer while the hole absorbs the magnons and re-creates them at other locations. Spin fluctuations act on longer time scales ($J_{dd} < t_{pp}$) and cannot therefore have a considerable effect on the quasiparticle that already has a fast dynamics controlled by T_{pp} . This has to be contrasted with one-band models where the hole is bound to magnon cloud that it creates by moving through the magnetic lattice [33]. In the absence of spin fluctuations, the only way for the hole to propagate is by executing the so-called Trugman loops [88] where the hole spends most of its time going around closed paths in order to free itself from the magnons. This results in a very heavy quasiparticle with

⁶Note that ARPES energies correspond to $\omega \rightarrow -\omega$, because we use a hole formulation.

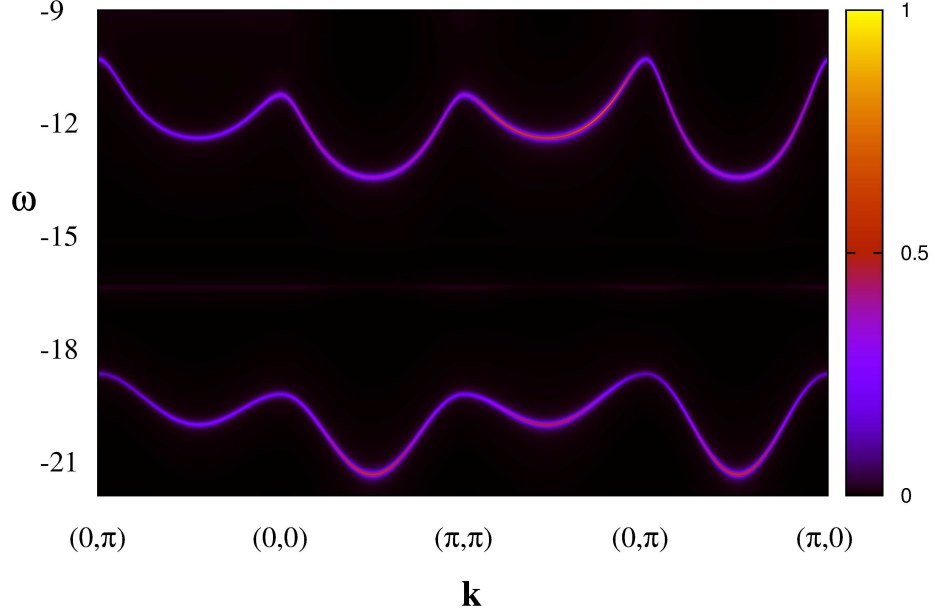


Figure 5.8: The spectral weight at $n_m = 2$ approximation, $A_{p_{x_1}}(\mathbf{k}, \omega)$ in color scale as a function of momentum and energy (in units of $J_{dd} \approx 0.1 - 0.15$ eV), showing several coherent bands. For the rest of this chapter, only the lowest energy band will be studied.

the ground state at $\mathbf{k} = \mathbf{0}$ [2]. Even when the spin fluctuations are included, the dispersion given by the one-band model with only nn hopping disagrees with experiments by being almost flat along $(\pi, 0)$ - $(0, \pi)$. Long range hopping which do not disturb the antiferromagnetic order must be introduced in order to obtain an isotropic quasiparticle dispersion [104, 105]. The existence of such longer range hopping terms in one-band models is justified using cluster calculations [106].

We also tried to mimic spin fluctuations by introducing them locally, which links two-magnon GFs to those with no magnons, $G_{\alpha,\beta}(\mathbf{k}, \omega)$, and vice versa. The effect on the energy dispersions, Fig. 5.9(b), was barely visible in that energy scale.

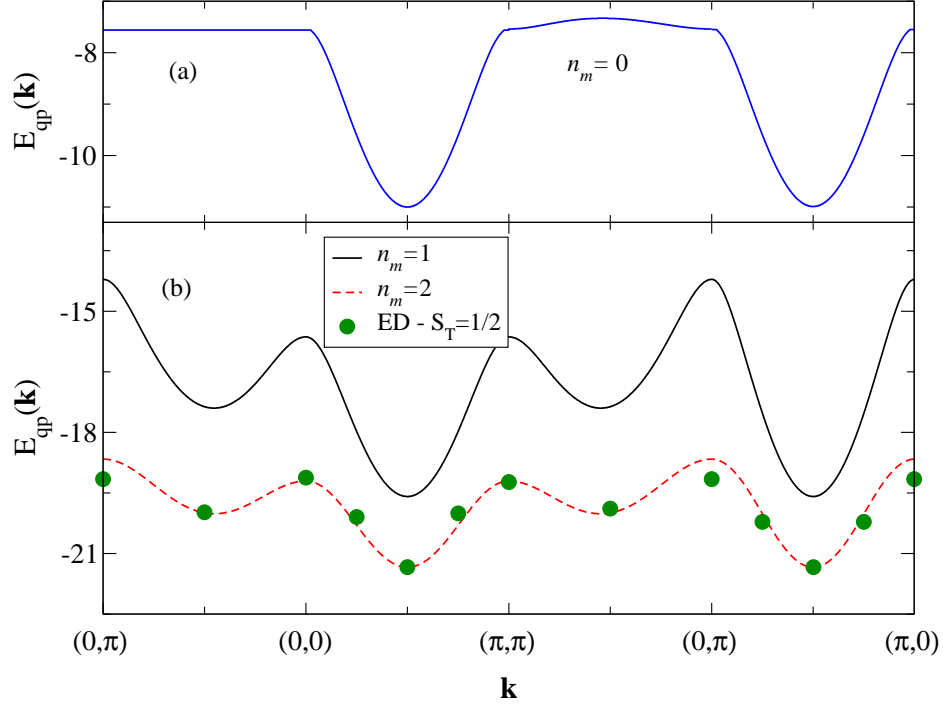


Figure 5.9: (a): Energy dispersion (in units of $J_{dd} \approx 0.1 - 0.15$ eV) of the hole without allowing for the creation of magnons, $n_m = 0$. The ground state is still at $\mathbf{k} = (\frac{\pi}{2}, \frac{\pi}{2})$. (b): Comparison between one- and two-magnon approximation results for the hole’s energy dispersion along various cuts in the full BZ. The dots are relevant exact-diagonalization calculations for a finite size sample of the same model, shifted in energy in order to ease the comparison.

5.4.2 Effect of various terms in the Hamiltonian

Now that we have established the convergence of our approximation, a natural question is whether the essential features of the quasiparticle dispersion $E_{qp}(\mathbf{k})$ are robust or they depend on the specific setting of parameters. To answer this question, we explore the role of various terms in the Hamiltonian (5.3) by removing them one at a time. Fig. 5.10 shows the quasiparticle dispersion with various terms on and off. Setting $J_{pd} = 0$ has essentially no major effect and results in a similar dispersion which is only shifted in energy as some exchange energy is lost. On the other hand, \hat{T}_{swap} is the crucial term and without it ($t_s = 0$) the dispersion changes completely. In

5.4. Results

particular, $\mathbf{k} = (\frac{\pi}{2}, \frac{\pi}{2})$ ceases to be the ground state in this case. Raising t_s from zero to half its actual value, Fig. 5.10(d), restores the proper shape of the dispersion and this suggest that t_{pp} and t_s have to be comparable for the correct shape to appear. Fig. 5.9(a) shows that, including all terms, one actually gets a deep minimum at $\mathbf{k} = (\frac{\pi}{2}, \frac{\pi}{2})$ even without allowing for the creation of any magnons, $n_m = 0$. This is very different from one-band models where the dispersion along $(0,0)$ - (π, π) is mainly controlled by spin fluctuations, in the absence of which the bare dispersion is completely anisotropic [107, 108]. Note that in other studies of three-band model \hat{T}_{pp} is only treated as a small perturbation [109–111], whereas here it has the largest energy scale in the Hamiltonian.

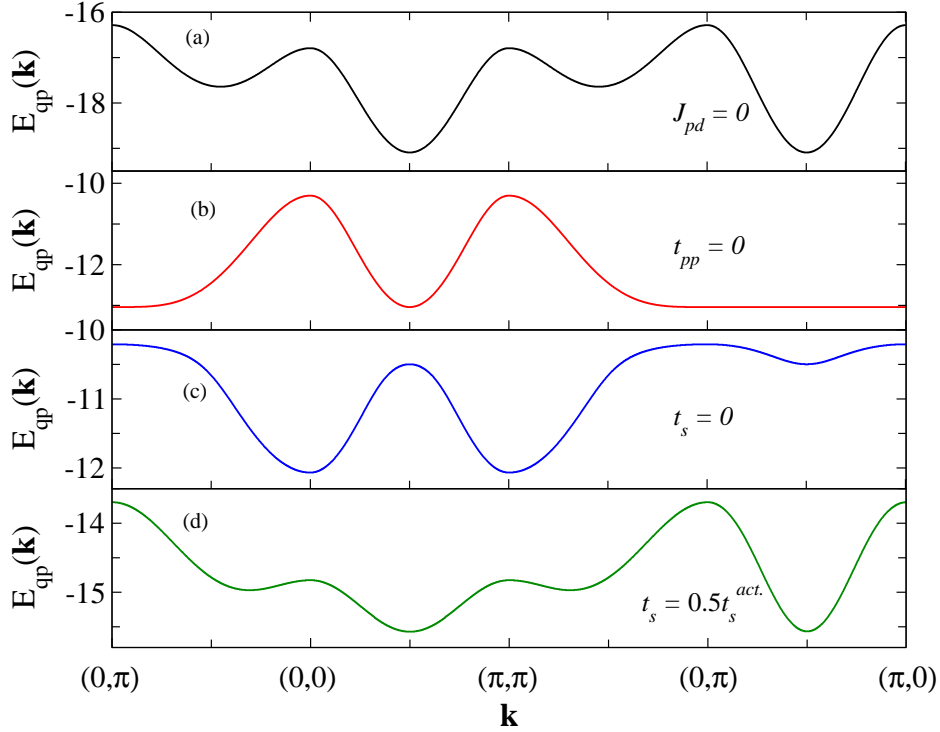


Figure 5.10: The lowest quasiparticle dispersion ($n_m = 2$ and in units of $J_{dd} \approx 0.1 - 0.15$ eV) when various terms in the Hamiltonian (5.3) are on and off. J_{pd} has almost no effect on the dispersion (a), whereas without t_s (c) the model fails to properly predict the expected ground state $\mathbf{k} = (\frac{\pi}{2}, \frac{\pi}{2})$. For comparable values of t_s and t_{pp} , the correct shape of energy dispersion re-appears (d).

5.5 Quasiparticle weight

In this section, we study the polaron's sublattice quasiparticle weights $Z_\alpha(\mathbf{k})$ along various cuts in the full BZ. It corresponds to residues at the poles of the sublattice spectral weight, i.e. $A_\alpha(\mathbf{k}, \omega) = Z_\alpha(\mathbf{k})\delta(\omega - E_{qp}(\mathbf{k}))$. In practice, delta peaks are broadened into Lorentzians due to the finite value used for η . For $\omega \approx E_{qp}(\mathbf{k})$, we can write:

$$\begin{aligned} A_\alpha(\mathbf{k}, \omega) &= -\frac{1}{\pi} \text{Im} G_{\alpha,\alpha}(\mathbf{k}, \omega)|_\eta = \frac{\eta}{\pi} \frac{Z_\alpha(\mathbf{k})}{(\omega - E_{qp}(\mathbf{k}))^2 + \eta^2} \\ &\rightarrow Z_\alpha(\mathbf{k}) = \pi\eta A_\alpha(\mathbf{k}, E_{qp}(\mathbf{k})), \end{aligned} \quad (5.26)$$

where α is any of the four distinct O $2p$ orbitals. Here, the quasi-momentum \mathbf{k} is unique only inside the magnetic BZ. The upper panel of Fig. 5.11 shows the quasiparticle weight $Z_{p_{x_1}}(\mathbf{k})$ at the lowest band for $n_m = 1$ and $n_m = 2$ approximations. As it was the case for the dispersions, the weights are similar in both levels of approximation. They are also symmetric about the ground state along $(0, 0)$ to (π, π) cut. This is a result of invariance under translation by reciprocal lattice vector, $\mathbf{k} \rightarrow \mathbf{k} - (\pi, \pi)$, and time-reversal symmetry, $\mathbf{k} \rightarrow -\mathbf{k}$. For $n_m = 2$, part of the quasiparticle wavefunction describes its two-magnon component and this explains the overall reduction of the quasiparticle weight in this case. Note that the weights follow a trend that is opposite to that of the quasiparticle dispersion, repeated at the lower panel of Fig. 5.11. In particular, both curves show that the quasiparticle weight is enhanced near local energy minima, although the $n_m = 2$ approximation does this slightly better by predicting the largest weight at the ground state $\mathbf{k} = (\frac{\pi}{2}, \frac{\pi}{2})$.

Unlike the dispersion relations, quasiparticle weights depend on the choice of orbitals on which the Green's functions are projected. Fig. 5.12 compares the quasiparticle weights $Z_{p_{x_1}}(\mathbf{k})$ and $Z_{p_{y_2}}(\mathbf{k})$ which correspond to $|\langle \mathbf{k}, p_{x_1}, \uparrow | \psi_{\mathbf{k}} \rangle|^2$ and $|\langle \mathbf{k}, p_{y_2}, \uparrow | \psi_{\mathbf{k}} \rangle|^2$, respectively. Differences in the weights along the first (third) cut suggests that the associated wavefunctions $|\psi_{\mathbf{k}}\rangle$ have more p_y (p_x) character for these momenta.

5.5.1 Comparison with ARPES

It was mentioned at the beginning of this chapter that the problem of a single hole in CuO₂ layer is closely related to angle-resolved photo-emission spectroscopy (ARPES) of cuprates, where the outgoing photo-electron is analyzed in energy and momentum in order to gain information about the dispersion of the hole left behind in the sample during photo-emission. The

5.5. Quasiparticle weight

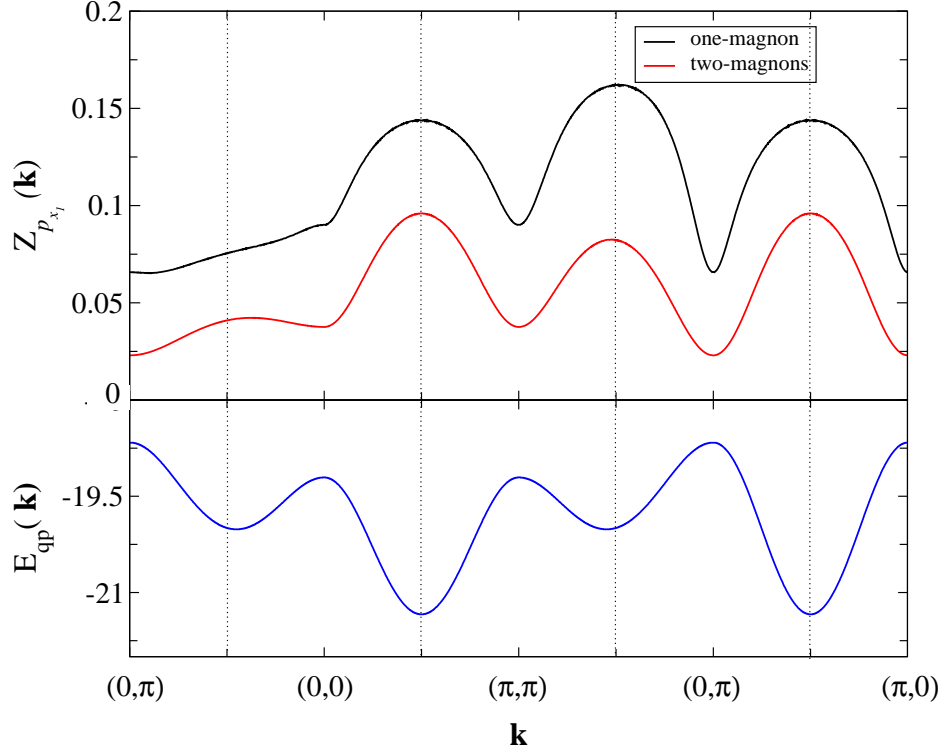


Figure 5.11: top: quasiparticle weights extracted from the sublattice GF $A_{p_{x_1}}(\mathbf{k}, \omega)$ in one- and two-magnon approximation. The corresponding energy dispersion (for the two-magnon approximation, in units of $J_{dd} \approx 0.1 - 0.15$ eV) is presented in the lower panel.

latter is what we extract from our GFs. Therefore, it would be of great interest to compare our calculations to results available from ARPES.

When a photon with an arbitrary polarization arrives in the CuO_2 layer, it does not make a distinction between different O sites and is equally likely to remove an electron from any one of the four $2p$ orbitals in the unit cell. It is shown in Appendix F that, after averaging over the polarization of the incident beam, the intensity of the outgoing photo-electrons in ARPES is given by the following expression

$$\bar{I}(\mathbf{K}, \omega) \propto \bar{A}^{\text{arpes}}(\mathbf{k}, \omega) \sim \sum_{\mathbf{k}, \mathbf{G}} \delta_{\mathbf{K}_{\parallel} + \mathbf{k}, \mathbf{G}} \sum_{\alpha, \beta} e^{i\mathbf{G} \cdot \mathbf{R}_{\alpha\beta}} \eta_{\alpha\beta} A_{\alpha\beta}(\mathbf{k}, \omega), \quad (5.27)$$

where $\mathbf{K} = (\mathbf{K}_{\parallel}, K_z)$ is the momentum of outgoing photo-electron and ω is the energy transferred to it during the photo-emission. $\mathbf{R}_{\alpha\beta} = \mathbf{R}_{\alpha} - \mathbf{R}_{\beta}$ are

5.5. Quasiparticle weight

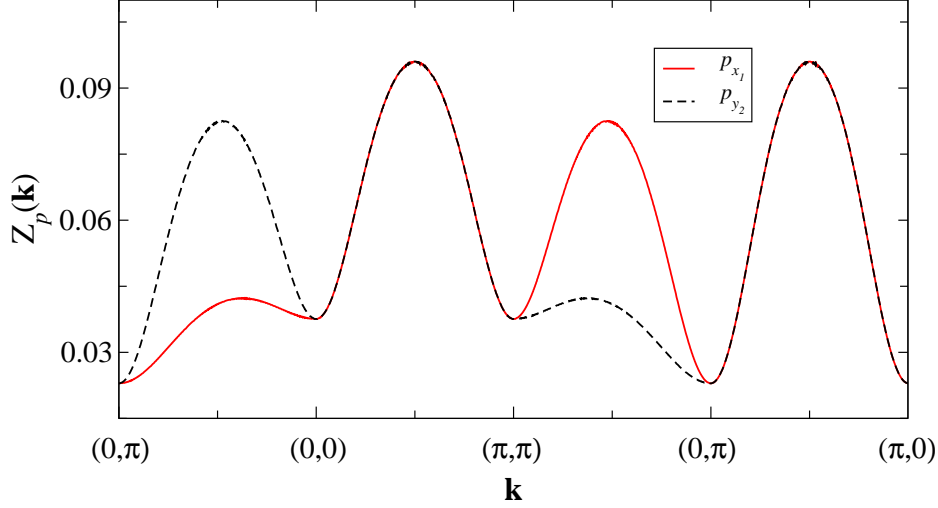


Figure 5.12: The quasiparticle weights in $n_m = 2$ approximation extracted from spectral weights that correspond to projections onto orbitals with different polarizations, $2p_x$ and $2p_y$.

the relative positions of various $2p$ orbitals in the unit cell, \mathbf{k} belong to the MBZ, \mathbf{G} are the corresponding reciprocal lattice vectors and $A_{\alpha\beta}(\mathbf{k}, \omega) = -\frac{1}{\pi} \text{Im} G_{\alpha\beta}(\mathbf{k}, \omega)$. $\eta_{\alpha\beta} = 1$ if α and β are both either $2p_x$ or $2p_y$ orbitals and zero otherwise and it reflects a selection rule resulting from averaging over the polarization of the incoming beam. When the coupling to spins is turned off, the dispersion relation of the remaining \hat{T}_{pp} can be analytically calculated. We checked to confirm that $\hat{A}^{\text{arpes}}(\mathbf{k}, \omega)$ gives the properly unfolded dispersion relation which agrees with the analytic result.

The ARPES quasiparticle weight is given in Fig. 5.13. Note that, unlike the sublattice spectral weights, $Z^{\text{arpes}}(\mathbf{k})$ is not symmetric about the ground state $\mathbf{k} = (\frac{\pi}{2}, \frac{\pi}{2})$ along $(0, 0) - (\pi, \pi)$. Whereas all $A_{\alpha\beta}(\mathbf{k}, \omega)$ show the periodicity of the MBZ as expected, $A^{\text{arpes}}(\mathbf{k}, \omega)$ does not do so because of the phases $e^{i\mathbf{G}\cdot\mathbf{R}_{\alpha\beta}}$: if \mathbf{k} is inside the magnetic BZ, $\mathbf{G} = \mathbf{0}$ and therefore contributions from, for example, $2p_{x_1}$ and $2p_{x_2}$ orbitals add up in Eq. (5.27), $e^{i\mathbf{G}\cdot\mathbf{R}_{x_2x_1}} = 1$. If \mathbf{k} enters the second magnetic BZ, then $\mathbf{G} = (\pm\pi, \pm\pi)$ and those contributions subtract since $\mathbf{R}_{x_2x_1} = \mathbf{y}$, therefore $e^{i\mathbf{G}\cdot\mathbf{R}_{x_2x_1}} = -1$.

Although the sublattice quasiparticle weights are finite, the interference between various spectral weights contributing to $A^{\text{arpes}}(\mathbf{k}, \omega)$ actually results in vanishing ARPES quasiparticle weight at the gamma point. However, its evolution along $(0, 0) - (\pi, \pi)$ disagrees with the ED result [3] and also with

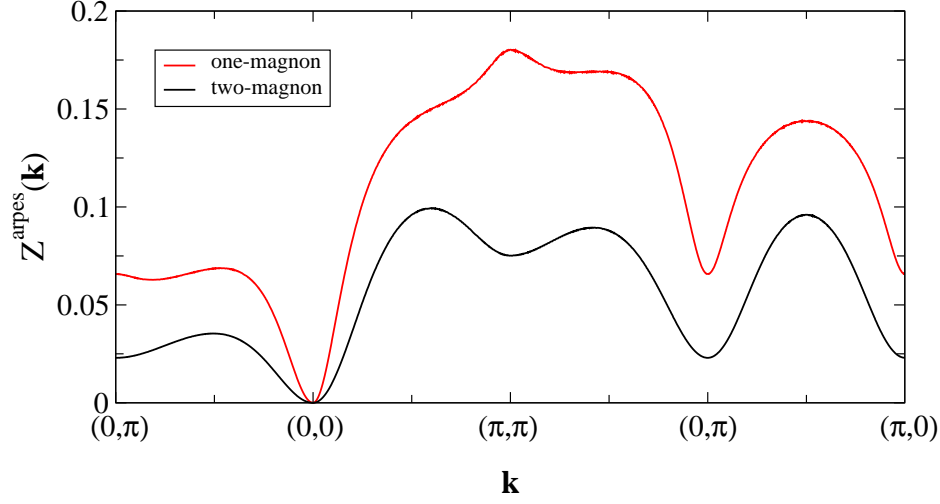


Figure 5.13: Comparison between one- and two-magnon approximation results for ARPES quasiparticle weight. This shows disagreement with experiments for momenta along $(0, 0) - (\pi, \pi)$. See text for further discussions.

experiments, which measure a large weight near $\mathbf{k} = (\frac{\pi}{2}, \frac{\pi}{2})$ which decreases fast in both directions [28]. It also shows that the quasiparticle weight is sensitive to the structure of magnon cloud, despite the fact that the shape of energy dispersion is almost independent of it. We will return to address this issue later in section 5.7.

5.6 Spin polaron vs the Zhang-Rice singlet

The three-band model can be compared with the effective one-band model in terms of their quasiparticle states, that is the spin polaron vs the Zhang-Rice singlet (ZRS). We can do so by calculating their overlap in various parts of the BZ.

The ZRS is a coherent superposition of the singlet states of Cu and the doping hole on four surrounding O's whose choice of phases reflects the $3d_{x^2-y^2}$ symmetry of central Cu,

$$|\mathbf{k}, \text{ZRS}\rangle = \frac{1}{\sqrt{8N}} \sum_{\mathbf{R}} e^{i\mathbf{k}\cdot\mathbf{R}} \sum_{\mathbf{u}} r_{\mathbf{u}} [p_{\mathbf{R}+\mathbf{u}/2, \uparrow}^{\dagger} - p_{\mathbf{R}+\mathbf{u}/2, \downarrow}^{\dagger} S_{\mathbf{R}}^+] |N\rangle, \quad (5.28)$$

where \mathbf{R} is the position of spin-down Cu and $\mathbf{u}/2 = \pm\mathbf{x}/2, \pm\mathbf{y}/2$ connect any spin-down Cu to its neighbouring O, those within the dashed circle in

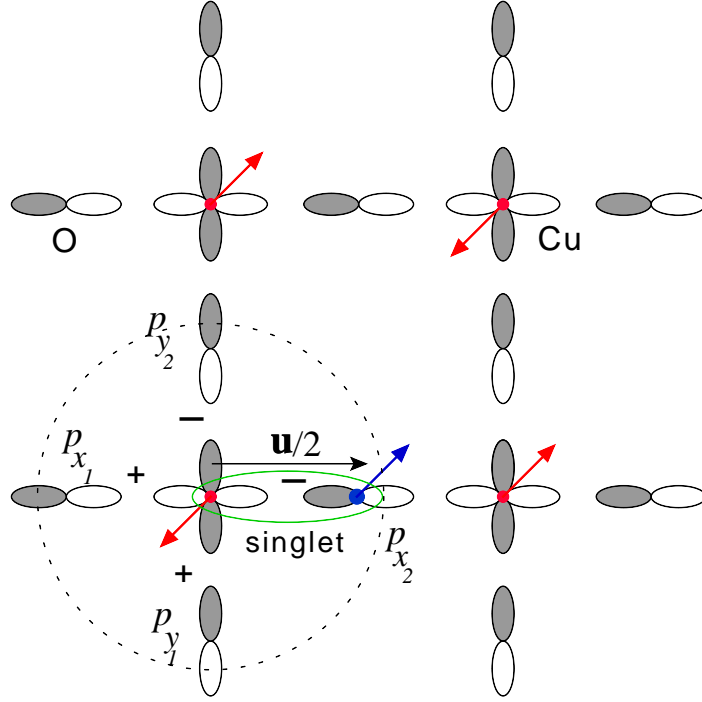


Figure 5.14: Inside the dashed circle are the copper and oxygens involved in Zhang-Rice singlet. Labelling of one-magnon GFs are such that once the copper and hole's spin are flipped, the current configuration becomes V_1^2 . The sign of each singlet contribution to ZRS is given.

Fig. 5.14; $r_{\mathbf{u}} = \pm 1$ imposes the $3d_{x^2-y^2}$ symmetry. If $|\phi\rangle$ is a polaron state with energy E_ϕ , belonging to the complete set of eigenstates $|\psi\rangle$, for $\omega \approx E_\phi$ we have

$$\begin{aligned}
 G_{p_\alpha, \text{ZRS}}(\mathbf{k}, E_\phi) &= \langle \mathbf{k}, p_\alpha, \uparrow | \hat{G}(\omega \approx E_\phi) | \mathbf{k}, \text{ZRS} \rangle = \lim_{\eta \rightarrow 0} \sum_{\psi} \frac{\langle \mathbf{k}, p_\alpha, \uparrow | \psi \rangle \langle \psi | \mathbf{k}, \text{ZRS} \rangle}{E_\phi - E_\psi + i\eta} \\
 &\approx \frac{\langle \mathbf{k}, p_\alpha, \uparrow | \phi \rangle \langle \phi | \mathbf{k}, \text{ZRS} \rangle}{i\eta},
 \end{aligned} \tag{5.29}$$

where $\sum_{\psi} |\psi\rangle \langle \psi| = 1$ is used. Similarly,

$$\begin{aligned}
 G_{p_\alpha, p_\alpha}(\mathbf{k}, E_\phi) &= \langle \mathbf{k}, p_\alpha, \uparrow | \hat{G}(\omega \approx E_\phi) | \mathbf{k}, p_\alpha, \uparrow \rangle \\
 &\approx \langle \mathbf{k}, p_\alpha, \uparrow | \phi \rangle \langle \phi | \mathbf{k}, p_\alpha, \uparrow \rangle / i\eta.
 \end{aligned} \tag{5.30}$$

Eq. (5.29) and (5.30) can be solved together to find the magnitude of overlap

5.6. Spin polaron vs the Zhang-Rice singlet

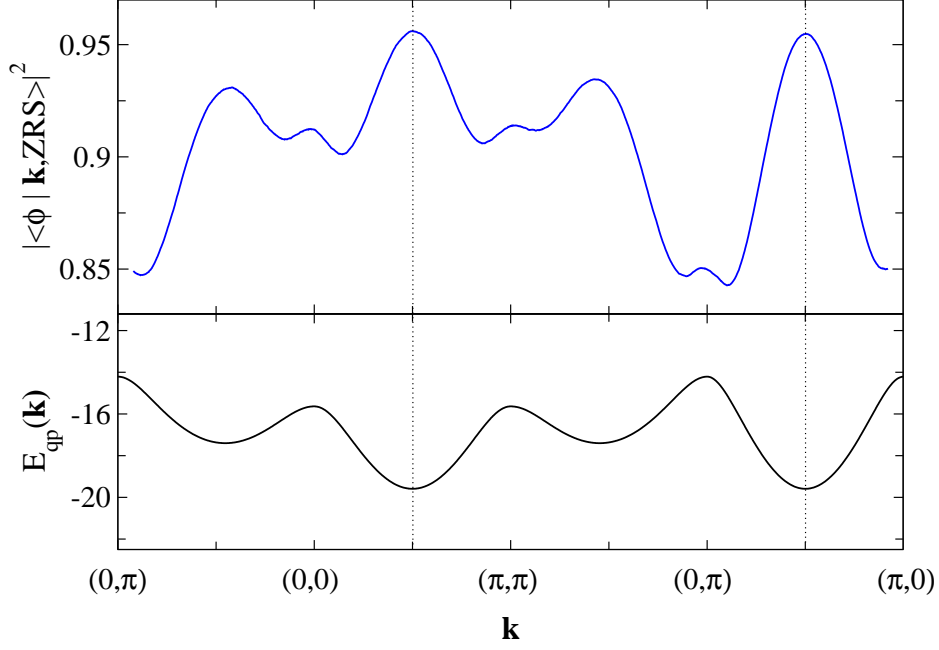


Figure 5.15: top: overlap between the states in the lowest polaron band $|\phi\rangle$ whose energy dispersion (in units of $J_{dd} \approx 0.1 - 0.15$ eV) is shown at the lower panel, and the corresponding Zhang-Rice singlet states.

between the polaron and ZRS states, $|\langle\phi|\mathbf{k}, \text{ZRS}\rangle|^2$:

$$|\langle\phi|\mathbf{k}, \text{ZRS}\rangle|^2 = \left| \frac{\eta G_{p\alpha, \text{ZRS}}(\mathbf{k}, \omega)}{G_{p\alpha, p\alpha}(\mathbf{k}, \omega)} \right|_{\omega \approx E_\phi}. \quad (5.31)$$

One has to note that O's in the ZRS are referenced with respect to the central Cu at \mathbf{R} and this differs with the way we defined our GFs in which the Bloch states are defined as a sum over O $2p$ orbitals, Eq. (5.7). For the one-magnon GFs, V_l , the sum runs over the position of $2p$ orbital on which the hole is initially created (for example, $\mathbf{R}_{p_{x_1}}$ in Eq. (5.12)). These result in additional phases factors $\varphi_{p_i} = \exp(-i\mathbf{k}\cdot\mathbf{u}_i/2)$. $G_{p\alpha, \text{ZRS}}(\mathbf{k}, \omega)$ is a combination of $G_{\alpha\beta}(\mathbf{k}, \omega)$ and some of one-magnon GFs, V_1 :

$$\begin{aligned} \sqrt{8}G_{p\alpha, \text{ZRS}}(\mathbf{k}, \omega) &= \varphi_{p_{x_1}} G_{p\alpha, p_{x_1}}(\mathbf{k}, \omega) + \varphi_{p_{y_1}} G_{p\alpha, p_{y_1}}(\mathbf{k}, \omega) \\ &\quad - \varphi_{p_{x_2}} G_{p\alpha, p_{x_2}}(\mathbf{k}, \omega) - \varphi_{p_{y_2}} G_{p\alpha, p_{y_2}}(\mathbf{k}, \omega) \\ &\quad - \varphi_{p_{x_1}} (V_1^0 + V_1^1 - V_1^2 - V_1^3), \end{aligned} \quad (5.32)$$

5.7. From three-band to five-band model: effect of other in-plane $2p$ orbitals

where V_1^i are those one-magnon GFs arising when the hole starts from p_{x_1} , see Fig. 5.14.

Fig. 5.15 shows the overlap along with the dispersion relation for the one-magnon approximation, $n_m = 1$. The overlap is generally large, suggesting that the spin polaron has considerable ZRS character. However, it is stronger close to the ground state and this implies that the ZRS is a more accurate description at low energies. As one moves away from the GS, the overlap decreases and this signals a deviation from effective one-band model at higher energies.

5.7 From three-band to five-band model: effect of other in-plane $2p$ orbitals

By investigating the effect of various terms in the Hamiltonian (5.3), we showed that the hybridization between O $2p_{x/y}$ and Cu $3d_{x^2-y^2}$ orbitals is essential for recovering the correct quasiparticle dispersion in the CuO₂ layer. Out of two in-plane $2p$ orbitals of each O in the layer, it therefore seems sufficient to only consider the one along Cu-Cu bonds as it directly hybridizes with Cu orbitals. Indeed, this has been the common approach and is also what we have so far considered. However, one can show that there is a considerable hopping amplitude between the other $2p$ orbitals and those directly hybridizing with Cu and occupied by the hole. Therefore the quasiparticle wavefunction actually spreads to all $2p$ orbitals and this affects its quasiparticle properties. In this section, we extend our analysis to take these other orbitals into account. This results in a five-band model.

We start by evaluating the hopping amplitudes involving these new orbitals, shown in blue in Fig. 5.16. The red dots represent Cu ions. The nn hopping between new $2p$ orbitals is same as that between the original ones t_{pp} , but the next nn hopping t'_{pp} is different: whereas t'_{pp} is boosted by the $4s$ orbital of the bridging Cu, there is no such state between new orbitals for the hole to tunnel through and the next nn hopping between new orbitals \tilde{t}'_{pp} is therefore expected to be weaker than t'_{pp} . Furthermore, the nn hopping t_{pp} is given as sum of the hopping for π and σ bonds between $2p$ orbitals: $t_{pp} = t_{pp,\sigma} + t_{pp,\pi} = 5t_{pp,\sigma}/4$ where in the last equality the relation $t_{pp,\pi} = t_{pp,\sigma}/4$ is used [112]. Since $t_{pp,\sigma}$ scales as $1/d^2$ with distance and $d_{nnn} = \sqrt{2}d_{nn}$, it follows that $\tilde{t}'_{pp} = t_{pp,\sigma}/2 = 2t_{pp}/5$. This is indeed weaker than next nn hopping between original orbitals $t'_{pp} = 0.58t_{pp}$. In any case, we observe little dependence on the precise value of \tilde{t}'_{pp} .

Having identified the new hopping amplitudes, equations of motion can

5.7. From three-band to five-band model: effect of other in-plane 2p orbitals

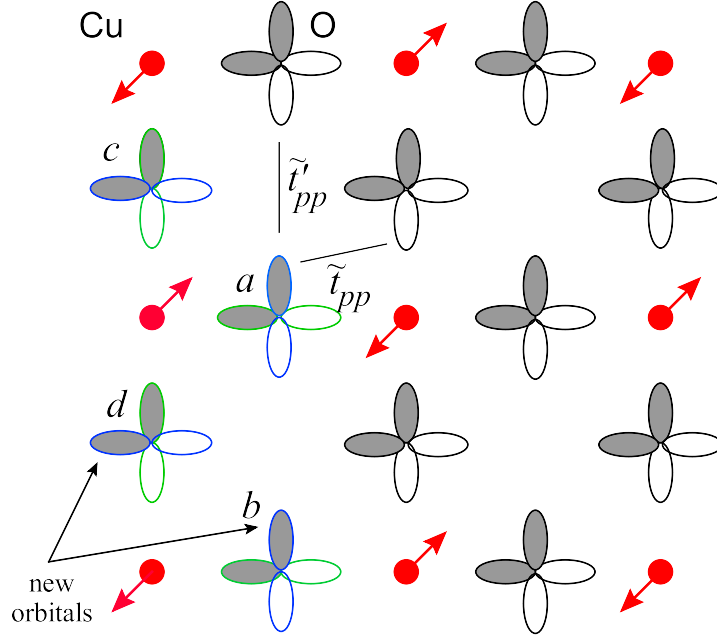


Figure 5.16: The CuO₂ layer with two in-plane 2p orbitals per O. The nn hopping between new (blue) and original (green) orbitals, \tilde{t}_{pp} , and the next nn hopping between the new orbitals, \tilde{t}'_{pp} , are shown.

be modified to include the contribution of new orbitals. Inside the unit cell, O's are labelled by a, b, c and d as indicated in Fig. 5.16 such that $p_{a_x/y}$ refers to $2p_{x/y}$ orbital associated with O_a , and so on. The calculation is similar to the three-band model but with 8×8 sublattice GFs $G_{\alpha,\beta}(\mathbf{k}, \omega)$ instead. The details are given in Appendix G.

In Fig. 5.17, I plot the lowest energy band and the associated ARPES quasiparticle weight of the five-band model for $n_m = 1$ and $n_m = 2$ approximations. The energy dispersion is quite similar to that of the three-band model and including the second set of 2p orbitals does not reveal new features. Indeed, the expectation that this other set of orbitals has little effect on the quasiparticle dynamics is correct. The bandwidths are slightly larger and this reflects the increase of the bare kinetic energy of the hole due to additional degrees of freedom provided by the new orbitals.

On the other hand, introducing these new orbitals has significant effect on the ARPES quasiparticle weight specially along $(0,0)-(\pi, \pi)$. $Z^{\text{arpes}}(\mathbf{K}_{\parallel})$ maintains the asymmetry about $(\frac{\pi}{2}, \frac{\pi}{2})$, but it shows a more consistent be-

5.7. From three-band to five-band model: effect of other in-plane $2p$ orbitals

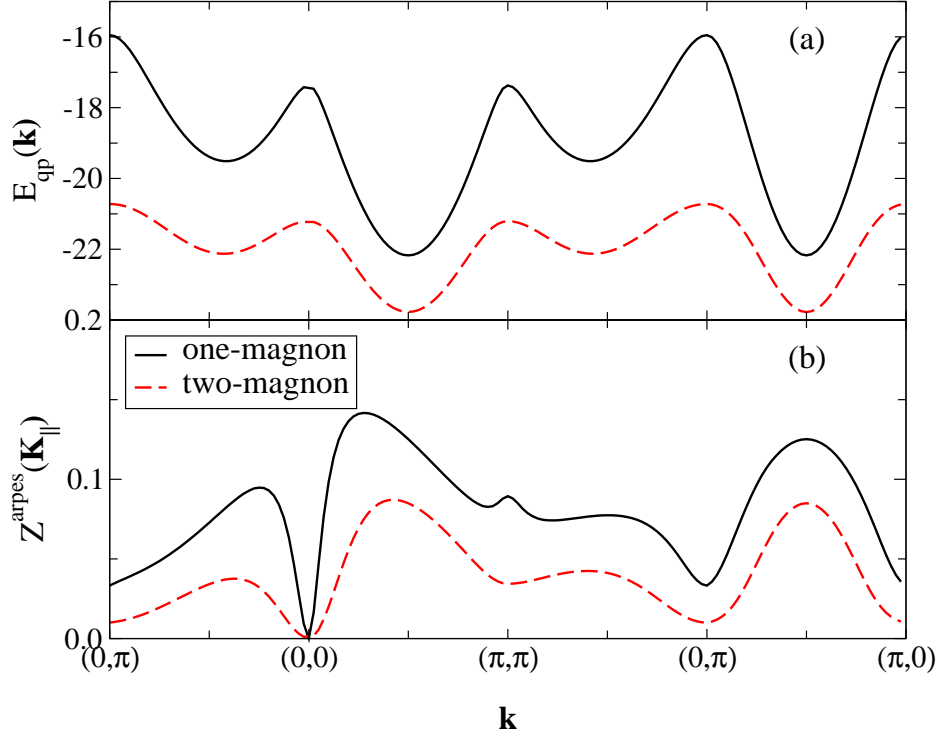


Figure 5.17: Energy dispersion (in units of $J_{dd} \approx 0.1 - 0.15$ eV) and ARPES quasiparticle weight of the five-band model that includes two $2p$ orbitals per O. Whereas the energy dispersions are qualitatively similar to those given by the three-band model, the quasiparticle weight is now less sensitive to the structure of magnon cloud.

behaviour for both one- and two-magnon approximations: quasiparticle weight is large near $(\frac{\pi}{2}, \frac{\pi}{2})$ and drops fast in both directions in agreement with experiments data [28, 105]. This has to be contrasted with the three-band model, Fig. 5.13, where the quasiparticle weight changes behaviour depending on how many magnons are kept in the cloud, in spite of the fact that the quasiparticle dispersions were robust. The ARPES quasiparticle weight is indeed expected to be different in the five band vs the three-band model. Upon introducing the new orbitals, the hole's wavefunction re-distributes itself by partly occupying these orbitals. This adds new terms to, and hence modifies, the ARPES spectral function Eq. (5.27) which is sensitive to the interference between similar $2p$ orbitals.

The other interesting feature is the asymmetry in the quasiparticle weight

5.7. From three-band to five-band model: effect of other in-plane $2p$ orbitals

between the inside and outside of MBZ. In Fig. 5.18, we plot the spectral function in the first quadrant of the FBZ for a constant energy close to ground state (low doping), $A^{\text{arpes}}(\mathbf{k}, \omega \approx E_{GS})$. It shows that the weight is larger inside MBZ along all cuts, a feature that persists for generic values of the parameters. A similar drop of the quasiparticle weight is measured by ARPES to occur outside the MBZ [28].

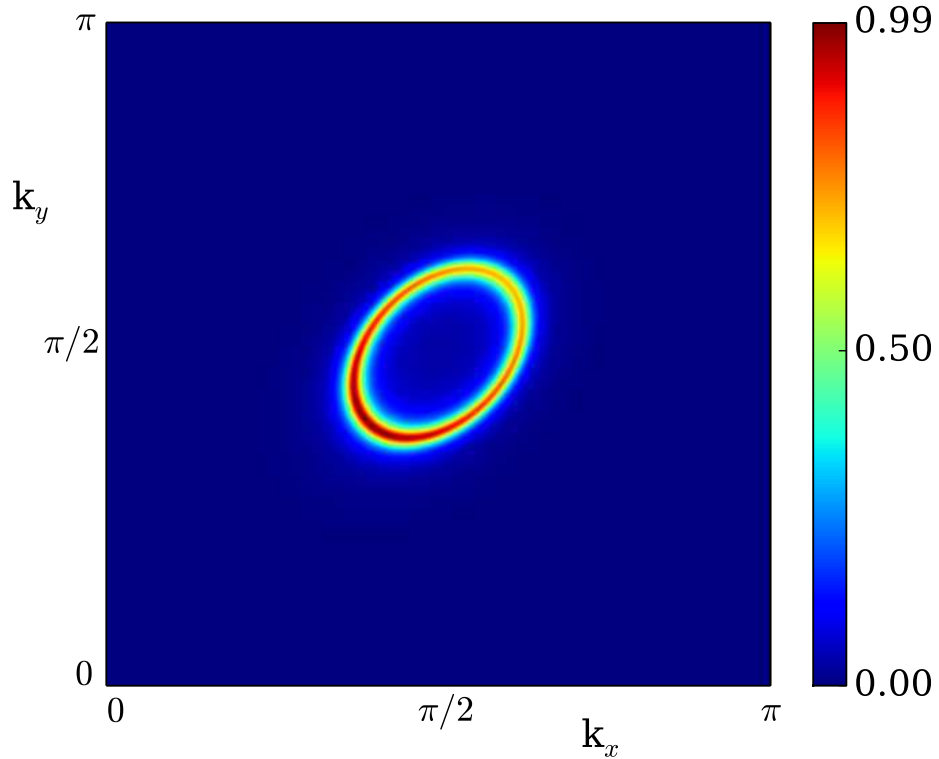


Figure 5.18: Constant-energy map of ARPES spectral weight for the five-band model. It clearly shows the asymmetry of the quasiparticle weight between the inside and outside of the magnetic BZ, which is a robust feature for the generic values of parameters.

The results of this section suggest that a complete understanding of the evolution of the spectral weight at low dopings, currently still missing, may require extending the theoretical models to include these additional orbitals. Since exact numerical approaches become even more challenging

to implement in larger Hilbert spaces, this will only increase the need for accurate approximations like the one we proposed here.

5.8 Conclusion

We developed a simple variational approximation for studying the spectral properties of a hole doped in three- and five-band models of CuO₂ layer. We confirmed the accuracy of our approximation by increasing the size of the variational space and comparing the quasiparticle's dispersion with available exact diagonalization results for a small cluster of the same model. Since the variational solution ignores the spin fluctuations of Cu, while they are fully included in the ED study, the agreement implies that these fluctuations do not play the significant role generally attributed to them in the quasiparticle dynamics. This is a significant finding because a proper description of spin fluctuations is quite a difficult task and it has hindered studying the two-hole case which provides information about the interaction between (and possible bound states of) quasiparticles.

In the three-band model, the hole can freely move on the O sublattice via \hat{T}_{pp} and therefore it is not localized near spin flips in the absence of spin fluctuations. In the one-band model, however, the ZRS moves in the magnetic sublattice and this creates strings of spin flips whose energy increases almost linearly with the length of the strings [88]. The only way for the hole to move then is by executing Trugman loops and this results in a very heavy quasiparticle. Spin fluctuations are hence needed to annihilate pairs of spin flips and release the hole, but the resulting energy dispersion is wrong as being almost flat along $(0, \pi) - (\pi, 0)$. This problem is overcome by introducing second and third nn hopping in the one-band model which allow the ZRS to move away from the spin flips created by the nn hops [106]. In the three-band model, this is accomplished by \hat{T}_{pp} and this justifies the lack of importance of the spin fluctuations.

We also extended our study into a five band model by including those in-plane $2p$ orbitals that do not directly hybridize with Cu. This resulted in a better agreement experiments for the quasiparticle weights. One has to note that doing so with exact numerical methods is computational very costly, whereas the efficiency of our method enabled us to readily implement this with minimum computational effort.

Chapter 6

Summary and development

6.1 Summary of this work

This thesis was an effort toward understanding the spectral properties of polaronic quasiparticles and their interaction with external potentials from impurities or more extended disorder. In particular, the Holstein polaron and spin polaron in antiferromagnetic insulators were considered.

In chapter 2, we extended the Momentum-Average approximation for calculating the Green's function of the Holstein polaron in systems with various types of disorder. MA is unique in that it sums all of the terms in the full diagrammatic expansion, but approximates each by discarding exponentially small contributions. It is exact in both zero coupling and zero bandwidth limit, and is also accurate everywhere in the parameter space. It has a variational interpretation where the number of lattice sites over which the polaron's phonon cloud is extended can be varied in order to improve the accuracy of the approximation.

Dyson's identity was used to calculate the polaron Green's function in real space. The main finding was that coupling to phonons, in addition to modifying the effective mass of the electron, renormalizes the disorder potential seen by the polaron in a non-trivial and retarded fashion. We showed that this renormalization is the result of the binding of the electron to its phonon cloud. It affects the electron's ability to interact with the outside potential in a way that depends on the structure of the cloud.

This formalism was used to investigate the binding of a Holstein polaron to a single impurity in three dimensions. Various kinds of impurities that modify the on-site energy and the strength of electron-phonon coupling, and isotope substitutions that change the coupling and phonon frequency were considered. The phase diagram of polaron trapping was constructed in each case and differences and similarities were discussed.

In chapter 3, we used the same formalism (suitably generalized) to study the lifetime of Holstein polaron due to weak and uncorrelated disorder that is extended over the entire system, also known as the (weak) Anderson disorder. When the strength of the electron-phonon coupling is weak, we found

that the polaron's inverse lifetime in units of its effective mass agrees with Fermi's golden rule prediction. This suggested that the effect of weak coupling to phonons is to enhance the effective mass of the electron. For strong coupling, significant deviation from the prediction of Fermi's golden rule was observed. We argued that this was due to the fact that the renormalization of the disorder potential becomes increasingly important at strong coupling. Therefore, the polaron scatters from a modified disorder potential and this difference is not captured by Fermi's golden rule.

In chapters 4, we switched to magnetically ordered systems where we focused on the spin polaron description of hole-like excitations in two dimensional antiferromagnetic (AFM) insulators. The nearest-neighbour hopping of a hole in an AFM on a square lattice creates a string of spin flips whose energy increases almost linearly with the length of the string. In the absence of the spin fluctuations, the hole may therefore become localized in the vicinity of spin flips. In fact, the hole can still propagate in the lattice by executing the so-called Trugman loop processes during which it goes almost twice around closed loops. The spin flips created during the first round are cleaned during the second round such that, when the last one of them is removed, the hole arrives at a different site of the same sublattice it started on. An analytic solution was obtained for the hole's Green's function by limiting the maximum number of such spin flips. It confirmed that the hole with the accompanying cloud of spin flips moves on one sublattice and the effective on-site energy and hopping amplitudes characterizing its motion were identified.

We then introduced an attractive impurity that changed the hole's on-site energy. Both cases of the impurity and the polaron being on the same vs on different sublattices were considered. Bound states were observed in both cases, and this was in spite of the fact that the polaron in its own sublattice was not subject to a bare impurity potential in the latter case. It was argued that this is a manifestation of the renormalization of impurity potential due to coupling to bosons, the concept that was introduced in the second chapter in the context of Holstein polarons. The hole can be found at varying distances from its boson cloud and this includes the other sublattice where it can interact with the impurity. Whereas a single bound state was found when the polaron and impurity were on the same sublattice, a total of three bound states were identified for the other case and their symmetry and the dependence of binding energies on the bare hole hopping were analyzed.

In the last chapter a more realistic model for the motion of a hole in a CuO_2 layer, in the absence of disorder, was constructed which included the O $2p$ orbitals explicitly. The model involved two types of spin fluctuations:

that of the AFM ordered Cu spins, and those caused by the doping hole. We neglected the first type, and kept the latter. A variational scheme was then constructed where we allowed for the creation of up to a certain maximum number of spin flips as the hole moved in the lattice. The convergence of our approximation was established by comparing the energy dispersion of the lowest polaron band with that given by the exact diagonalization study of the same model, as well as with the experimental results. In this model the hole is able to move freely within the O sublattice and, as a result, spin fluctuations are not essential for releasing the hole as a light polaron (as they are in one-band models with only nn hopping).

Our approach is computationally quite efficient and this allowed us to generalize it to investigate the effect of other in-plane O $2p$ orbitals on the hole's dynamics. Whereas including these other orbitals resulted essentially in similar quasiparticle dispersions, the quasiparticle weights were found to be considerably modified upon including new orbitals and better agreement with the experiments was obtained.

6.2 Outlook and further developments

One of the common themes throughout this work was the use of variational techniques as a way of studying many-body problems. They basically involved choosing a subspace, from the entire Hilbert space of the problem, that includes the energetically most relevant states. This enabled us to perform semi-analytic and non-perturbative calculations. Although the results in principle depend on the choice of variational space, a desired level of accuracy can be reached by varying the size of the space.

This variational scheme has been originally suggested and successfully applied for studying Holstein polarons [50]. We succeed in verifying that these methods are not limited to lattice polarons and can be used for studying polarons in magnetic systems as well. Similar ideas have been applied by others in the context of orbital polarons.

In chapters 2 and 3, we limited our study to either a single impurity or extended but weak disorder. A natural extension is to consider extended disorder of arbitrary strength. A new phenomenon that may occur in this regime is the Anderson localization of Holstein polarons. It is well known that the disorder averaged descriptions, as the one used in chapter 3 for weak disorder, fail to capture localization. Instead, the signature of localization can be traced to the distribution of quantities such as the local density of states, $\mathcal{P}[\{\rho_i(\omega)\}]$, which is suggested to change from normal to log-

normal when the energy state at ω becomes localized [42]. The formalism developed in chapter 2 allows us to calculate the local densities of states for any disorder configuration, but a challenge here is to be able to consider large enough system sizes in order to have enough number of LDOS values for a meaningful statistical analysis.

Given the success of our variational scheme in describing the spectral properties of a single hole in the CuO_2 layer, extending it to study a pair of holes can be rewarding. In particular, one can address the question of whether there are any coherent bound states of two holes, and if so, what their pairing symmetry is. The advantage of our Green's function formalism for this problem is that since the Green's function of the pair gives the relative wave function of the two holes, it will enable one to explicitly map out the pairing symmetry in the real space (provided that bound states exist). This will provide a microscopic picture of the pre-formed pairs in cuprate superconductors and it contrasts with common macroscopic descriptions where the pairing symmetry is studied not in the real space, but it refers to the structure of superconducting energy gap in the momentum space.

The analysis in chapter 4 can be generalized for studying other variants of the $t\text{-}J_z$ model. Within the three-magnon variational space, $t\text{-}J$ model is mimicked by locally including spin fluctuations which relates zero- and one-magnon Green's functions to two- and three-magnon ones, respectively, and vice versa. Further range hoppings can also be treated similarly within the same variational space. This enables studying $t\text{-}t'\text{-}t''\text{-}J$ model as well as the effect of three-site hopping which is among the terms appearing in the strong coupling limit of the Hubbard model [113]. We found that, unlike the three-band model, spin fluctuations are actually essential for recovering the correct quasiparticle dispersion in one-band models. We argued that the different role played by spin fluctuations suggests that quasiparticles described by one- and three-band models are qualitatively different. This casts doubt on whether one-band $t\text{-}J$ like models are suitable for studying cuprate physics. This work [107], which is under review for publication, does not appear in this thesis.

Bibliography

- [1] M. Berciu, A. S. Mishchenko and N. Nagaosa, EPL **89**, 37007 (2010).
- [2] M. Berciu and H. Fehske, Phys. Rev. B **84**, 165104 (2011).
- [3] B. Lau, M. Berciu, and G. A. Sawatzky, Phys. Rev. Lett. **106**, 036401 (2011).
- [4] A. S. Mishchenko, N. Nagaosa, A. Alvermann, H. Fehske, G. De Filippis, V. Cataudella, and O. P. Sushkov, Phys. Rev. B **79**, 180301(R) (2009).
- [5] C. Kittel, *Introduction to Solid State Physics*, 8th edition (John Wiley Sons, Inc., 2005).
- [6] H. J. Schulz, in "Proceedings of Les Houches Summer School LXI", [<http://arxiv.org/abs/cond-mat/9503150>] (1995).
- [7] L. D. Landau, Phys. Zh. Sowjet **3**, 664 (1933).
- [8] H. Bässler and A. Köhler, Top. Curr. Chem. **312**, 1 (2012).
- [9] J. Bardeen, L. N. Cooper, and J. R. Schrieffer, Phys. Rev. **108**, 1175 (1957).
- [10] C. P. J. Adolphs and M. Berciu, EPL **102**, 47003 (2013).
- [11] C. P. J. Adolphs and M. Berciu, Phys. Rev. B **89**, 035122 (2014).
- [12] L. Covaci and M. Berciu, Europhys. Lett. **80**, 67001 (2007).
- [13] T. Holstein, Ann. Phys. (N.Y.) **8**, 325 (1959); **8**, 343 (1959).
- [14] M. Berciu, Phys. Rev. Lett. **97**, 036402 (2006); G. L. Goodvin, M. Berciu, and G. A. Sawatzky, Phys. Rev. B **74**, 245104 (2006).
- [15] I. G. Lang and Y. A. Firsov, Sov. Phys. JETP **16**, 1301 (1963).
- [16] F. Marsiglio, Phys. Lett. A **180**, 280 (1993).

Bibliography

- [17] A. A. V. Kabanov, and D. Ray, Phys. Rev. B **49**, 9915 (1994).
- [18] E. V. L. de Mello, and J. Ranninger, Phys. Rev. B **55**, 14872 (1997).
- [19] P. Kornilovitch, E. Pike, Phys. Rev. B (Rapid) **55**, 8634 (1997).
- [20] P. Kornilovitch, Phys. Rev. Lett. **81**, 5382 (1998).
- [21] P. Kornilovitch, Phys. Rev. B **60**, 3237 (1999).
- [22] H. Fröhlich, H. Pelzer, and S. Zienau, Philos. Mag. **41**, 221 (1950).
- [23] C. Slezak, A. Macridin, G. A. Sawatzky, M. Jarrell, and T. A. Maier, Phys. Rev. B **73**, 205122 (2006).
- [24] B. Lau, M. Berciu, and G. A. Sawatzky, Phys. Rev. B **76**, 174305 (2007).
- [25] A. S. Alexanrov, and J. T. Devreese, Advances in Polaron Physics, Springer Series in Solid-State Science, Vol. **159** (2010).
- [26] W. P. Su, J. R. Schrieffer, and A. J. Heeger, Phys. Rev. Lett. **42**, 1698 (1979).
- [27] A. J. Heeger, S. Kivelson, J. R. Schrieffer, and W. -P. Su, Rev. Mod. Phys. **60**, 781 (1988).
- [28] A. Damascelli, Z. Hussain, and Z. X. Shen, Rev. Mod. Phys. **75**, 473 (2003).
- [29] P. W. Anderson, Phys. Rev. **109**, 1493 (1958).
- [30] B. Kramer, and A. MacKinnon, Rep. Prog. Phys. **56**, 1469 (1993).
- [31] P. A. Lee and D. S. Fisher, Phys. Rev. Lett. **47**, 882 (1981).
- [32] H. Ebrahimnejad and M. Berciu, Phys. Rev. B **85**, 165117 (2012).
- [33] H. Ebrahimnejad and M. Berciu, Phys. Rev. B **88**, 104410 (2013).
- [34] D. Marchand, PhD Thesis, University of British Columbia (2011).
- [35] G. L. Goodvin, PhD Thesis, University of British Columbia (2009).
- [36] F. C. Zhang, and T. M. Rice, Phys. Rev. B **37**, 3759(R) (1988).

- [37] A. Lanzara, P. V. Bogdanov, X. J. Zhou, S. A. Kellar, D. L. Feng, E. D. Lu, T. Yoshida, H. Eisaki, A. Fujimori, K. Kishio, J. -I. Shimoyama, T. Noda *et al.*, Nature **412**, 510 (2001).
- [38] D. N. Basov, B. Dabrowski, and T. Timusk, Phys. Rev. Lett. **81**, 2132 (1998).
- [39] J. Lee, K. Fujita, K. McElroy, J. A. Slezak, M. Wang, Y. Aiura, H. Bando, M. Ishikado, T. Masui, J.-X. Zhu, A. V. Balatsky, H. Eisaki, S. Uchida *et al.*, Nature **442**, 546 (2006).
- [40] S. M. Girvin and M. Jonson, Phys. Rev. B **22**, 3583 (1980).
- [41] O. Gunnarsson, M. Calandra, and J. E. Han, Rev. Mod. Phys. **75**, 1085 (2003).
- [42] F. X. Bronold, and H. Fehske, Phys. Rev. B **66**, 073102 (2002); F. X. Bronold, A. Alvermann, and H. Fehske, Philos. Mag. **84**, 673 (2004). For LDA, see A. Alvermann and H. Fehske: *Local Distribution Approach*, Lecture Notes in Phys. **739**, 505-526 (Springer, 2008).
- [43] S. Ciuchi, F. de Pasquale, S. Fratini, and D. Feinberg, Phys. Rev. B **56**, 4494 (1997).
- [44] H. Sumi, J. Phys. Soc. Jpn. **36**, 770 (1974).
- [45] F. X. Bronold, A. Saxena and A. R. Bishop, Phys. Rev. B **63**, 235109 (2001).
- [46] J. P. Hague, P. E. Kornilovitch, and A. S. Alexandrov, Phys. Rev. B **78**, 092302 (2008).
- [47] L. Covaci and M. Berciu, Phys. Rev. Lett. **102**, 186403 (2009).
- [48] M. Berciu and G. L. Goodvin, Phys. Rev. B **76**, 165109 (2007).
- [49] A. N. Das and S. Sil, Phys. Lett. A **348**, 266 (2006); in a somewhat different context, see also A. N. Das and S. Sil. J. Phys.: Condens. Matter **5**, 8265 (1993) or A. Macridin, G. A. Sawatzky and Mark Jarrell, Phys. Rev. B **69**, 245111 (2004).
- [50] M. Berciu and G. L. Goodvin, Phys. Rev. B **76**, 165109 (2007); M. Berciu, Phys. Rev. Lett. **98**, 209702 (2007).
- [51] O. S. Barisic, Phys. Rev. Lett. **98**, 209701 (2007).

Bibliography

- [52] A. M. Clogston, Phys. Rev. **125**, 439 (1962).
- [53] P. A. Wolff, Phys. Rev. **124**, 1030 (1961).
- [54] M. Berciu and A. M. Cook, Europhys. Lett. **92**, 40003 (2010).
- [55] M. Berciu and H. Fehske, Phys. Rev. B **82**, 085116 (2010); D. J. J. Marchand, G. De Filippis, V. Cataudella, M. Berciu, N. Nagaosa, N. V. Prokof'ev, A. S. Mishchenko, and P. C. E. Stamp, Phys. Rev. Lett. **105**, 266605 (2010).
- [56] J. Bonca, S.A. Trugman, and I. Batistic, Phys. Rev. B **60**, 1633 (1999).
- [57] A. S. Mishchenko and N. Nagaosa, Phys. Rev. B **73**, 092502 (2006).
- [58] C. Bernhard, T. Holden, A. V. Boris, N. N. Kovaleva, A. V. Pimenov, J. Humlicek, C. Ulrich, C. T. Lin, and J. L. Tallon, Phys. Rev. B **69**, 052502 (2004).
- [59] P. W. Anderson, Phys. Rev. **109**, 1492 (1958).
- [60] A. Miller and E. Abrahams, Phys. Rev. **120**, 745 (1960).
- [61] A. A. Abrikosov, L. P. Gorkov and I. Ye. Dzyaloshinski, *Methods of quantum field theory in statistical physics* (Dover, New York, 1975).
- [62] Strictly speaking, the lifetime is defined with an additional factor of 2.
- [63] M. Berciu, Phys. Rev. Lett. **98**, 209702 (2007).
- [64] C. L. Kane, P. A. Lee, and N. Read, Phys. Rev. B **39**, 6880 (1989).
- [65] F. Marsiglio, A. E. Ruckenstein, S. Schmitt-Rink, and C. M. Varma, Phys. Rev. B **43**, 10882 (1991).
- [66] S. Sachdev, Phys. Rev. B **39**, 12232 (1989).
- [67] A. V. Chubukov and D. K. Morr, Phys. Rev. B **57**, 5298 (1998).
- [68] B. I. Shraiman and E. D. Siggia, Phys. Rev. Lett. **60**, 740 (1988).
- [69] P. A. Lee, N. Nagaosa, and X. G. Wen, Rev. Mod. Phys. **78**, 17 (2006).
- [70] P. Phillips, Rev. Mod. Phys. **82**, 1719 (2010).
- [71] E. Manousakis, Rev. Mod. Phys. **63**, 1 (1990).

Bibliography

- [72] E. Dagotto, R. Joynt, A. Moreo, S. Bacci and E. Gagliano, Phys. Rev. B **41**, 9049 (1990); H. Fehske, V. Waas, H. Röder and H. Büttner, *ibid.* **44**, 8473 (1991); E. Dagotto, Rev. Mod. Phys. **66**, 763 (1994).
- [73] H. Alloul, J. Bobroff, M. Gabay, and P. J. Hirschfeld, Rev. Mod. Phys. **81**, 45 (2009).
- [74] D. Heidarian and N. Trivedi, Phys. Rev. Lett. **93**, 126401 (2004); Yun Song, R. Wortis and W. A. Atkinson, R. Wortis and W. A. Atkinson, Phys. Rev. B **77**, 054202 (2008); Phys. Rev. B **82**, 073107 (2010).
- [75] A. Suchaneck, V. Hinkov, D. Haug, L. Schulz, C. Bernhard, A. Ivanov, K. Hradil, C. T. Lin, P. Bourges, B. Keimer, and Y. Sidis, Phys. Rev. Lett. **105**, 037207 (2010).
- [76] S. Wessel, B. Normand, M. Sigrist, and S. Haas, Phys. Rev. Lett. **86**, 1086 (2001).
- [77] D. Poilblanc, D. J. Scalapino, and W. Hanke, Phys. Rev. Lett. **72**, 884 (1994).
- [78] D. Poilblanc, D. J. Scalapino, and W. Hanke, Phys. Rev. B **50**, 13020 (1994).
- [79] W. F. Brinkman, and T. M. Rice, Phys. Rev. B **2**, 1324 (1970).
- [80] D. Poilblanc, H. J. Schulz, and H. T. Ziman, Phys. Rev. B **47**, 3268 (1993).
- [81] D. M. Edwards, Physica B **133**, 378 (2004).
- [82] A. Alvermann, D. M. Edwards, and H. Fehske, Phys. Rev. Lett. **98**, 056602 (2007).
- [83] D. M. Edwards, Phys. Rev. B **82**, 085116 (2010).
- [84] J. Riera and E. Dagotto, Phys. Rev. B **47**, 15346 (1993); E. Lahoud, O. Nganba Meetei, K. B. Chaska, A. Kanigel, and N. Trivedi, arXiv:1303.0649v1.
- [85] Note that Eq. (18) in Ref. [2] has a typo in the denominator, where the prefactor 4 behind $t_3(\omega)$ has to be replaced with 2.
- [86] M. Möller, A. Mukherjee, C. P. J. Adolphs, D. J. J. Marchand, and M. Berciu, J. Phys. A: Math. Theor. **45**, 115206 (2012).

Bibliography

- [87] P. Chudzinski, M. Gabay, and T. Giamarchi, *New J. Phys.* **11**, 055059 (2009).
- [88] S. A. Trugman, *Phys. Rev. B* **37**, 1597 (1988).
- [89] V. J. Emery, *Phys. Rev. Lett.* **58**, 2794 (1987).
- [90] H. Eskes, and G. A. Sawatzky, *Phys. Rev. Lett.* **61**, 1415 (1988).
- [91] T. Giamarchi, and C. Lhuillier, *Phys. Rev. B* **47**, 2775 (1993).
- [92] E. Dagotto, A. Moreo, R. Joynt, S. Bacci, and E. Gagliano, *Phys. Rev. B* **41**, 2585(R) (1990).
- [93] E. Dagotto, R. Joynt, A. Moreo, S. Bacci, and E. Gagliano, *Phys. Rev. B* **41**, 9049 (1990).
- [94] V. Elser, D. A. Huse, B. I. Shraiman, and E. D. Siggia, *Phys. Rev. B* **41**, 6715 (1990).
- [95] M. Boninsegni, and E. Manousakis, *Phys. Rev. B* **43**, 10353 (1991).
- [96] D. Poilblanc, H. J. Schulz, and T. Ziman, *Phys. Rev. B* **46**, 6435 (1992).
- [97] M. M. Sala *et al.*, *New J. Phys.* **13**, 043026 (2011).
- [98] J. Zaanen, G. A. Sawatzky, and J. W. Allen, *Phys. Rev. Lett.* **55**, 418 (1985).
- [99] G. Martinez, and P. Horsch, *Phys. Rev. B* **44**, 317 (1991).
- [100] A. Fujimori, E. Takayama-Muromachi, Y. Uchida, and B. Okai, *Phys. Rev. B* **35**, 8814 (1987); J. M. Tranquada, S. M. Heald, A. R. Moodenbaugh, and M. Suenaga, *ibid.* **35**, 7187 (1987).
- [101] M. Ogata, and H. Fukuyama, *Rep. Prog. Phys.* **71**, 036501 (2008); P. A. Lee, *ibid.* **71**, 012501 (2008).
- [102] B. Lau, PhD Thesis, University of British Columbia (2011).
- [103] H. Ebrahimnejad, G. A. Sawatzky, and M. Berciu, *Nature Physics* **10**, 951-955 (2014).
- [104] P. W. Leung, B. O. Wells, and R. J. Gooding, *Phys. Rev. B* **56**, 6320 (1997).

- [105] B. O. Wells, *et al.*, Phys. Rev. Lett. **74**, 964 (1995).
- [106] J. H. Jefferson, H. Eskes, and L. F. Feiner, Phys. Rev. B **45**, 7959 (1992).
- [107] “The t - J and the Emery model have qualitatively different quasiparticles”, H. Ebrahimnejad and M. Berciu, submitted (2014).
- [108] T. Xiang and J. M. Wheatley, Phys. Rev. B **54**, R12653 (1996).
- [109] V. J. Emery, and G. Reiter, Phys. Rev. B **38**, 4547 (1988).
- [110] D. M. Frenkel, R. J. Gooding, B. I. Shraiman, and E. D. Siggia, Phys. Rev. B **41**, 350 (1990).
- [111] Y. Petrov, T. Egami, Phys. Rev. B **58**, 9485 (1998).
- [112] W. A. Harrison, Elementary Electronic Structure (World Scientific, Singapore, (1999).
- [113] J. Bała, Eur. Phys. J. B **16**, 495500 (2000).
- [114] R. J. Elliot, J. A. Krumhansl and P. L. Leath, Rev. Mod. Phys. **46**, 465 (1974).
- [115] E. N. Economou, *Green’s Functions in Quantum Physics*, 3rd edition (Springer-Verlag, New York, 2006), or A. Gonis, “Green Functions for Ordered and Disordered Systems” (Elsevier, Amsterdam, 1992).

Appendix A

MA⁰ solution for the clean system

Using the notation of chapter 2, the Holstein Hamiltonian for a clean system is

$$\mathcal{H}_H = \mathcal{H}_0 + \hat{V}_{\text{el-ph}}, \quad (\text{A.1})$$

where we use the real-space notation for electron-phonon coupling term:

$$\hat{V}_{\text{el-ph}} = g \sum_i c_i^\dagger c_i (b_i + b_i^\dagger).$$

\mathcal{H}_0 is the sum of kinetic energy of particle and lattice vibrational energy. Our goal is to calculate the retarded single polaron Green's function

$$G_H(\mathbf{k}, \omega) = \langle 0 | c_{\mathbf{k}} \hat{G}_H(\omega) c_{\mathbf{k}}^\dagger | 0 \rangle,$$

using the Dyson's identity $\hat{G}_H(\omega) = \hat{G}_0(\omega) + \hat{G}_H(\omega) \hat{V}_{\text{el-ph}} \hat{G}_0(\omega)$. Projecting this onto single electron Bloch states gives

$$G_H(\mathbf{k}, \omega) = G_0(\mathbf{k}, \omega) \left[1 + g \sum_i \frac{e^{i\mathbf{k} \cdot \mathbf{R}_i}}{\sqrt{N}} F_{\mathbf{k}i}^{(1)}(\omega) \right], \quad (\text{A.2})$$

where $F_{\mathbf{k}i}^{(n)}(\omega) = \langle 0 | c_{\mathbf{k}} \hat{G}_H(\omega) c_i^\dagger b_i^{\dagger n} | 0 \rangle$. Note that $F_{\mathbf{k}i}^{(0)}(\omega) = G_H(\mathbf{k}, \omega) \exp(-i\mathbf{k} \cdot \mathbf{R}_i) / \sqrt{N}$. Using the Dyson identity again, we find that for $n \geq 1$

$$\begin{aligned} F_{\mathbf{k}i}^{(n)}(\omega) &= g \sum_{j \neq i} G_{ji}^0(\omega - n\Omega) \langle 0 | c_{\mathbf{k}} \hat{G}_H(\omega) c_j^\dagger b_j^\dagger b_i^{\dagger n} | 0 \rangle \\ &\quad + g G_{ii}^0(\omega - n\Omega) \left[n F_{\mathbf{k}i}^{(n-1)}(\omega) + F_{\mathbf{k}i}^{(n+1)}(\omega) \right], \end{aligned} \quad (\text{A.3})$$

where

$$G_{ji}^0(\omega) = \sum_{\mathbf{k}} \frac{e^{i\mathbf{k} \cdot (\mathbf{R}_j - \mathbf{R}_i)}}{N} G_0(\mathbf{k}, \omega)$$

is the free particle propagator in real space and the sum is over the momenta inside the first Brillouin zone. This propagator decays exponentially with the distance $|\mathbf{R}_j - \mathbf{R}_i|$ for energies outside the free particle continuum, $|\omega| > 6t$. Since we are interested in energies $\omega - n\Omega \approx E_{P,GS} - n\Omega$, where the polaron GS energy $E_{p,GS} < -6t$, all these propagators become exponentially small for $j \neq i$. It is therefore a reasonable first approximation to ignore $j \neq i$ terms in Eq. (A.3). This is what the MA^0 approximation does (higher flavors include $j \neq i$ terms in a certain progression [48]).

Within MA^0 , then, we have for any $n \geq 1$

$$F_{\mathbf{k}i}^{(n)}(\omega) = gg_0(\omega - n\Omega) \left[nF_{\mathbf{k}i}^{(n-1)}(\omega) + F_{\mathbf{k}i}^{(n+1)}(\omega) \right], \quad (\text{A.4})$$

where $g_0(\omega) = G_{ii}^0(\omega)$; see Eq. (3.15). This recurrence relation is solved in terms of continued fractions [14]:

$$F_{\mathbf{k}i}^{(n)}(\omega) = A_n(\omega)F_{\mathbf{k}i}^{(n-1)}(\omega) \quad (\text{A.5})$$

for any $n \geq 1$, where

$$A_n(\omega) = \frac{ngg_0(\omega - n\Omega)}{1 - gg_0(\omega - n\Omega)A_{n+1}(\omega)}. \quad (\text{A.6})$$

Finally, using $F_{\mathbf{k}i}^{(1)}(\omega) = A_1(\omega)F_{\mathbf{k}i}^{(0)}(\omega)$ in Eq. (A.2) leads to the MA^0 solution:

$$G_{\text{H}}(\mathbf{k}, \omega) = \frac{1}{\omega - \varepsilon(\mathbf{k}) - gA_1(\omega) + i\eta}.$$

$\Sigma_{\text{MA}}(\omega) = gA_1(\omega)$ is therefore identified as the self energy associated with Holstein type electron-phonon coupling.

Appendix B

IMA¹

At the IMA¹ level, one also allows processes in which one phonon is away from the phonon cloud. These are described by the propagators $S_n(i, l, j; \omega) = \langle 0 | c_i G(\omega) c_l^\dagger b_l^{\dagger n-1} b_j^\dagger | 0 \rangle$ with $j \neq l$. In terms of these, Eq. (2.3) can be written as

$$G_{ij}(\omega) = G_{ij}^d(\omega) + \sum_l g_l S_1(i, l, l; \omega) G_{lj}^d(\omega). \quad (\text{B.1})$$

Once again we apply the Dyson identity to S_1

$$\begin{aligned} S_1(i, l, j; \omega) &= g_j G_{jl}^d(\omega - \Omega_j) G_{ij}(\omega) \\ &+ \sum_m g_m G_{ml}^d(\omega - \Omega_j) S_2(i, m, j; \omega). \end{aligned} \quad (\text{B.2})$$

This exact equation relates S_1 to the propagators S_2 . We can similarly find the equation of motion of all higher, $n \geq 2$, $S_n(i, l, j; \omega)$ with $l \neq j$ and $l = j$, separately. For $l \neq j$ we have

$$\begin{aligned} S_n(i, l, j; \omega) &= g_l G_{ll}^d(\omega - (n-1)\Omega_l - \Omega_j) \\ &\times [(n-1)S_{n-1}(i, l, j; \omega) + S_{n+1}(i, l, j; \omega)], \end{aligned} \quad (\text{B.3})$$

where we now ignore contributions from terms with a second phonon away from the polaron cloud, as they are exponentially smaller than those we kept. This admits the solution $S_n(i, l, j; \omega) = B_n(l, j; \omega) S_{n-1}(i, l, j; \omega)$, where

$$\begin{aligned} B_n(l, j; \omega) &= \frac{(n-1)g_l G_{ll}^d(\omega - (n-1)\Omega_l - \Omega_j)}{1 - g_l G_{ll}^d(\omega - (n-1)\Omega_l - \Omega_j) B_{n+1}(l, j; \omega)} \\ &= A_{n-1}(l, \omega - \Omega_j). \end{aligned} \quad (\text{B.4})$$

For $l = j$ and $n \geq 2$, $S_n(i, l, l; \omega) = F_{il}^{(n)}(\omega)$ and we get the same solution as in MA⁰, i.e. $S_n(i, l, l; \omega) = A_n(l, \omega) S_{n-1}(i, l, l; \omega)$. The relations between S_2 and S_1 are used in Eq. (B.2) to turn it into an equation between $S_1(\omega)$ and $G_{ij}(\omega)$ only

$$\begin{aligned} S_1(i, l, j; \omega) &= g_j G_{jl}^d(\omega - \Omega_j) G_{ij}(\omega) + g_j G_{jl}^d(\omega - \Omega_j) A_2(j, \omega) S_1(i, j, j; \omega) \\ &+ \sum_{m \neq j} g_m G_{ml}^d(\omega - \Omega_j) A_1(m, \omega - \Omega_j) S_1(i, m, j; \omega). \end{aligned}$$

Together with Eq. (B.1), this can be solved to find $G_{ij}(\omega)$. However, it is again convenient to explicitly extract the ‘‘average’’ contributions, to make these equations more efficient.

We therefore remove the homogeneous part from Eq. (B.2) and include it into a renormalized energy

$$S_1(i, l, j; \omega) = g_j G_{jl}^d(\bar{\omega}_j) [G_{ij}(\omega) + (A_2(j, \omega) - A_1(j, \omega - \Omega_j)) S_1(i, j, j; \omega)] \\ + \sum_{m \neq j} g_m G_{ml}^d(\bar{\omega}_j) [A_1(m, \omega - \Omega_j) - A_1(\omega - \Omega)] S_1(i, m, j; \omega). \quad (\text{B.5})$$

where $\bar{\omega}_j = \omega - \Omega_j - gA_1(\omega - \Omega)$, and $A_1(\omega - \Omega)$ is given by Eq. (2.11) for the ‘‘average’’ clean system. The sum on the rhs of Eq. (B.5) again converges for a very small cutoff, only sites m very close to j need to be included. Its general solution is of the form:

$$S_1(i, l, j; \omega) = x_{jl}(\omega) [G_{ij}(\omega) + (A_2(j, \omega) - A_1(j, \omega - \Omega_j)) S_1(i, j, j; \omega)], \quad (\text{B.6})$$

where

$$x_{jl}(\omega) = g_j G_{jl}^d(\bar{\omega}_j) + \sum_{m \neq j} g_m G_{ml}^d(\bar{\omega}_j) [A_1(m, \omega - \Omega_j) - A_1(\omega - \Omega)] x_{jm}(\omega).$$

In fact, using $x_{jl}(\omega) = g_j G_{jl}^d(\bar{\omega}_j)$ is already a very good approximation, since the terms in the sum are exponentially small – but one can go beyond this. Once $x_{jj}(\omega)$ is known, from Eq. (B.6) we find $S_1(i, j, j, \omega) = \Lambda_j(\omega) G_{ij}(\omega)$, where

$$\Lambda_j(\omega) = \frac{x_{jj}(\omega)}{1 - x_{jj}(\omega) (A_2(j, \omega) - A_1(j, \omega - \Omega_j))}.$$

This can now be used in Eq. (B.1) to turn it into an equation for $G_{ij}(\omega)$ only:

$$G_{ij}(\omega) = G_{ij}^d(\omega) + \sum_l g_l \Lambda_l(\omega) G_{il}(\omega) G_{lj}^d(\omega). \quad (\text{B.7})$$

As we did in Eq. (2.13) for MA^0 , this can be made efficient to solve by subtracting the MA^1 self-energy and including it into the energy argument

$$G_{ij}(\omega) = G_{ij}^d(\tilde{\omega}) + \sum_l G_{il}(\omega) v_1(l, \omega) G_{lj}^d(\tilde{\omega}), \quad (\text{B.8})$$

in which $\tilde{\omega} = \omega - \Sigma_{MA^1}(\omega)$ and $v_1(l, \omega) = g_l \Lambda_l(\omega) - \Sigma_{MA^1}(\omega)$. Here, $\Sigma_{MA^1}(\omega)$ is the value of $g_l \Lambda_l(\omega)$ in the clean, ‘‘average’’ system:

$$\Sigma_{MA^1}(\omega) = \frac{g^2 g_0(\bar{\omega})}{1 - g g_0(\bar{\omega}) (A_2(\omega) - A_1(\omega - \Omega))}$$

where now $\bar{\omega} = \omega - \Omega - gA_1(\omega - \Omega)$ [48]. This completes the calculation of GF within inhomogeneous MA¹ approximation.

Appendix C

MA⁰ solution for $F_{\mathbf{k},si}^{(n)}(\omega)$ and $W^{nm}(\omega)$

First, let's we evaluate

$$F_{\mathbf{k},si}^{(n)}(\omega) = \langle 0 | c_{\mathbf{k}} \hat{G}_{\mathbf{H}}(\omega) c_i^\dagger b_s^{\dagger n} | 0 \rangle$$

within MA⁰. In this level, this propagator vanishes for all $i \neq s$, because it is proportional to $G_{si}^0(\omega - n\Omega)$. Therefore, all we need to evaluate is $F_{\mathbf{k}i}^{(n)}(\omega) = \langle 0 | c_{\mathbf{k}} \hat{G}_{\mathbf{H}}(\omega) c_i^\dagger b_i^{\dagger n} | 0 \rangle$ which have been already calculated in Appendix A,

$$\begin{aligned} F_{\mathbf{k}i}^{(n)}(\omega) &= A_n(\omega) F_{\mathbf{k}i}^{(n-1)}(\omega) \\ &= \prod_{l=1}^n A_l(\omega) F_{\mathbf{k}i}^{(0)}(\omega) \\ &\equiv \Gamma_n(\omega) F_{\mathbf{k}i}^{(0)}(\omega), \end{aligned} \tag{C.1}$$

where $\Gamma_n(\omega) \equiv \prod_{l=1}^n A_l(\omega)$ and $F_{\mathbf{k}i}^{(0)}(\omega) = \exp(-i\mathbf{k} \cdot \mathbf{R}_i) G_{\mathbf{H}}(\mathbf{k}, \omega) / \sqrt{N}$. $A_l(\omega)$ are the continued fractions introduced in the text.

Let's now calculate the $W^{nm}(\omega) = \langle 0 | b_i^n c_i \hat{G}_{\mathbf{H}}(\omega) c_i^\dagger b_i^{\dagger m} | 0 \rangle$. Because $W^{nm}(\omega) = W^{mn}(\omega)$, we only need to find $W^{nm}(\omega)$ for $m \leq n$. Note that we already know $W^{00}(\omega) = \langle 0 | c_i \hat{G}_{\mathbf{H}}(\omega) c_i^\dagger | 0 \rangle = \frac{1}{N} \sum_{\mathbf{k}} G_{\mathbf{H}}(\mathbf{k}, \omega) = g_0(\omega - \Sigma_{\text{MA}}(\omega))$. Furthermore,

$$\begin{aligned} W^{n0}(\omega) &= \langle 0 | b_i^n c_i \hat{G}_{\mathbf{H}}(\omega) c_i^\dagger | 0 \rangle \\ &= \sum_{\mathbf{k}} \frac{e^{-i\mathbf{k} \cdot \mathbf{R}_i}}{\sqrt{N}} \left[F_{\mathbf{k}i}^{(n)}(\omega) |_{\eta \rightarrow -\eta} \right]^* \\ &= \Gamma_n(\omega) g_0(\omega - \Sigma_{\text{MA}}(\omega)). \end{aligned} \tag{C.2}$$

For any $m \geq 1$, the equations of motion for $W^{nm}(\omega)$ within the MA approximation (i.e., not allowing the electron to change its site when phonons are

present) leads to

$$W^{nm}(\omega) = m!g_0(\omega - m\Omega)\delta_{nm} + gg_0(\omega - m\Omega) \times [mW^{n,m-1}(\omega) + W^{n,m+1}(\omega)]. \quad (\text{C.3})$$

For $m > n$, the delta function vanishes and Eq. (C.3) is identical to Eq. (A.4), hence

$$W^{nm}(\omega) = A_m(\omega)W^{n,m-1}(\omega). \quad (\text{C.4})$$

In particular, this gives $W^{n,n+1}(\omega) = A_{n+1}(\omega)W^{nn}(\omega)$. Using this in Eq. (C.3) with $n = m$ relates $W^{nn}(\omega)$ to $W^{n,n-1}(\omega)$,

$$W^{nn}(\omega) = A_n(\omega)W^{n,n-1}(\omega) + \frac{(n-1)!}{g}A_n(\omega). \quad (\text{C.5})$$

This is taken together with the EOM for $1 \leq m \leq n-1$

$$W^{nm}(\omega) = gg_0(\omega - m\Omega) \times [mW^{n,m-1}(\omega) + W^{n,m+1}(\omega)]$$

to give a system of n equations with n unknowns $W^{nm}(\omega)$, $m = 1, \dots, n$ [$W^{n0}(\omega)$ is known; see above]. This can be solved in many ways, including direct numerical solution. A nicer approach is to use the linearity of this system of equations to split it into two different systems, with $\frac{(n-1)!}{g}A_n(\omega)$ and $gg_0(\omega - \Omega)W^{n0}(\omega)$ as inhomogeneous parts. These can be solved analytically to give

$$W^{nm}(\omega) = \Gamma_m(\omega)W^{n0}(\omega) + \tilde{\Gamma}_m(\omega) \frac{(n-1)!A_n(\omega)}{g[1 - A_n(\omega)B_n(\omega)]},$$

where $\tilde{\Gamma}_m(\omega) = B_{m+1}(\omega)B_{m+2}(\omega) \cdots B_n(\omega)$ for $m < n$ where $\tilde{\Gamma}_n(\omega) = 1$, and

$$B_{m+1}(\omega) = \frac{gg_0(\omega - m\Omega)}{1 - (m-1)gg_0(\omega - m\Omega)B_m(\omega)}$$

are continued fractions ending at $B_2(\omega) = gg_0(\omega - \Omega)$.

Appendix D

Disorder self-energy in Average T-matrix approximation

Average T-matrix approximation (ATA) [114, 115] relates the disorder part of the self-energy of a single particle to the disorder average of its transfer matrix through a single impurity whose on-site energy is ϵ :

$$\Sigma_{\text{ATA}}(\omega) = \frac{\bar{t}}{1 + \bar{t}g_0(\omega)}, \quad (\text{D.1})$$

where $t = \epsilon/(1 - \epsilon g_0(\omega))$ is the sum over all single impurity scattering contributions. $g_0(\omega)$ is the momentum average of the free particle propagator, see Eq. (3.15). For Anderson-type disorder of width 2Δ we find

$$\begin{aligned} \bar{t} &= \frac{1}{2\Delta} \int_{-\Delta}^{\Delta} \frac{\epsilon d\epsilon}{1 - \epsilon g_0(\omega)} \\ &= -\frac{1}{g_0(\omega)} + \frac{1}{2\Delta g_0^2(\omega)} \ln \frac{1 + \Delta g_0(\omega)}{1 - \Delta g_0(\omega)}. \end{aligned}$$

Expanding to lowest order in Δ regains the perturbational result, Eq. (3.14):

$$\Sigma_{\text{ATA}}(\omega) \approx \frac{\Delta^2}{3} g_0(\omega) = \sigma^2 g_0(\omega).$$

Therefore, differences between ATA and FGR show that disorder is so large that multiple scattering processes off the same impurity cannot be ignored anymore.

To extend ATA to the Holstein model, we note that difference between the MA clean polaron's GF and that of the free electron is the appearance of $\Sigma_{\text{MA}}(\omega)$. This simply modifies $g_0(\omega) \rightarrow g_0(\omega - \Sigma_{\text{MA}}(\omega))$ in all the above equations. As discussed above, this approximation implies that there is no crossing between phonon lines and scattering lines, in diagrammatic terms. Our results show that this is a bad approximation for medium to strong electron-phonon coupling.

Appendix E

The equations of motion for $G_{\mathbf{0},\mathbf{R}}(\omega)$

Here we present the details of the calculations that lead to Eq. (4.12), which relates the various $G_{\mathbf{0},\mathbf{R}}(\omega)$ GFs. Eq. (4.11) enables us to eliminate F_3 from Eq. (4.10) to obtain:

$$F_2(\mathbf{R}, \mathbf{u}, \mathbf{v}) - t^2 \bar{g}_2 g_3 F_2(\mathbf{R} + \mathbf{u} + \mathbf{v}, -\mathbf{v}, -\mathbf{u}) = -t \bar{g}_2 F_1(\mathbf{R}, \mathbf{u}), \quad (\text{E.1})$$

and

$$F_2(\mathbf{R} + \mathbf{u} + \mathbf{v}, -\mathbf{v}, -\mathbf{u}) - t^2 \bar{g}_2 g_3 F_2(\mathbf{R}, \mathbf{u}, \mathbf{v}) = -t \bar{g}_2 F_1(\mathbf{R} + \mathbf{u} + \mathbf{v}, -\mathbf{v}), \quad (\text{E.2})$$

where $\bar{g}_2 = 1/(\omega - 14\bar{J} - t^2 g_3 + i\eta)$ and Eq. (E.2) results from Eq. (E.1) after changing the coordinates $\mathbf{R} \rightarrow \mathbf{R} + \mathbf{u} + \mathbf{v}$, $\mathbf{u} \rightarrow -\mathbf{v}$, $\mathbf{v} \rightarrow -\mathbf{u}$. Solving the coupled equations (E.1) and (E.2), we find

$$F_2(\mathbf{R}, \mathbf{u}, \mathbf{v}) = \gamma_1 F_1(\mathbf{R}, \mathbf{u}) + \gamma_2 F_1(\mathbf{R} + \mathbf{u} + \mathbf{v}, -\mathbf{v}), \quad (\text{E.3})$$

in which $\gamma_1 = -t \bar{g}_2 / [1 - (t^2 \bar{g}_2 g_3)^2]$ and $\gamma_2 = t^2 \bar{g}_2 g_3 \gamma_1$. Using this in Eq. (4.9) gives

$$F_1(\mathbf{R}, \mathbf{u}) = -t \bar{g}_1 [G_{\mathbf{0},\mathbf{R}} + \gamma_2 \sum_{\mathbf{v} \perp \mathbf{u}} F_1(\mathbf{R} + \mathbf{u} + \mathbf{v}, -\mathbf{v})], \quad (\text{E.4})$$

where $\bar{g}_1 = 1/(\omega - 10\bar{J} + 2t\gamma_1 + i\eta)$ and the sum includes the two nearest-neighbor vectors, $\pm\mathbf{v}$, along the direction perpendicular to \mathbf{u} . With a proper change of coordinates, each F_1 on the right-hand side of Eq. (E.4) can be expressed in term of a component of G and new F_1 's. For example,

$$F_1(\mathbf{R} + \mathbf{u} + \mathbf{v}, -\mathbf{v}) + t \bar{g}_1 G_{\mathbf{0},\mathbf{R}+\mathbf{u}+\mathbf{v}} = -t \bar{g}_1 \gamma_2 [F_1(\mathbf{R} + \mathbf{2u}, -\mathbf{u}) + F_1(\mathbf{R}, \mathbf{u})], \quad (\text{E.5})$$

and

$$F_1(\mathbf{R} + \mathbf{u} - \mathbf{v}, \mathbf{v}) + t \bar{g}_1 G_{\mathbf{0},\mathbf{R}+\mathbf{u}-\mathbf{v}} = -t \bar{g}_1 \gamma_2 [F_1(\mathbf{R} + \mathbf{2u}, -\mathbf{u}) + F_1(\mathbf{R}, \mathbf{u})], \quad (\text{E.6})$$

which results after applying either of $\mathbf{R} \rightarrow \mathbf{R} + \mathbf{u} \pm \mathbf{v}$, $\mathbf{u} \rightarrow \mp \mathbf{v}$, $\mathbf{v} \rightarrow \mathbf{u}$ to Eq. (E.4), respectively. The additionally introduced F_1 can be written in terms of the existing ones by doing $\mathbf{R} \rightarrow \mathbf{R} + 2\mathbf{u}$, $\mathbf{u} \rightarrow -\mathbf{u}$ on Eq. (E.4)

$$F_1(\mathbf{R} + 2\mathbf{u}, -\mathbf{u}) + t\bar{g}_1 G_{\mathbf{0},\mathbf{R}+2\mathbf{u}} = -t\bar{g}_1 \gamma_2 [F_1(\mathbf{R} + \mathbf{u} + \mathbf{v}, -\mathbf{v}) + F_1(\mathbf{R} + \mathbf{u} - \mathbf{v}, \mathbf{v})]. \quad (\text{E.7})$$

The four equations (E.4) to (E.7) can be simultaneously solved for the four F_1 's in terms of the existing components of G . In particular, we find:

$$F_1(\mathbf{R}, \mathbf{u}) = \zeta_1 G_{\mathbf{0},\mathbf{R}} + \zeta_2 G_{\mathbf{0},\mathbf{R}+2\mathbf{u}} + \zeta_3 [G_{\mathbf{R}+\mathbf{u}+\mathbf{v}} + G_{\mathbf{R}+\mathbf{u}-\mathbf{v}}], \quad (\text{E.8})$$

where $\zeta_1 = -t\bar{g}_1[1 - 2(t\bar{g}_1\gamma_2)^2]/[1 - 4(t\bar{g}_1\gamma_2)^2]$, $\zeta_2 = -2t\bar{g}_1(t\bar{g}_1\gamma_2)^2/[1 - 4(t\bar{g}_1\gamma_2)^2]$ and $\zeta_3 = -t\bar{g}_1\gamma_2(\zeta_1 + \zeta_2)$. Finally, using this in Eq. (4.7) results in the equation of motion for the GF

$$G_{\mathbf{0},\mathbf{R}}(\omega) = \bar{g}_0(\omega)[\delta_{\mathbf{R},\mathbf{0}} - t_1(\omega) \sum_{\delta} G_{\mathbf{0},\mathbf{R}+\delta}(\omega) - t_2(\omega) \sum_{\xi} G_{\mathbf{0},\mathbf{R}+\xi}(\omega)], \quad (\text{E.9})$$

and its various coefficients are given in the text following Eq. (4.12).

These effective hoppings and on-site energies are identical to those derived for the clean system in Ref. [2][85]. In the presence of disorder, the solution proceeds similarly but now various g functions acquire dependence on the location since their argument is shifted by U if $\mathbf{R} = \mathbf{0}$. This leads to dependence on location (and even direction of hopping) for the effective hopping and on-site energies, at sites close enough to the impurity.

Appendix F

Derivation of ARPES intensity

In ARPES, an incoming photon kicks out an electron from the sample and this leaves a hole behind. For an energy transfer of ω , the intensity of outgoing electrons with momentum \mathbf{K} can be written as

$$I(\mathbf{K}, \omega) \sim \sum_{n, \mathbf{k}} |\langle \mathbf{K} | \mathbf{A}(\mathbf{r}) \cdot \mathbf{p} | n, \mathbf{k} \rangle|^2 \delta(\omega - E_n(\mathbf{k})), \quad (\text{F.1})$$

where $\mathbf{A}(\mathbf{r}) = \epsilon A_0 e^{i\mathbf{q} \cdot \mathbf{r}}$ is the electromagnetic potential of the incoming photon that results in scattering of electrons from polaron states $|n, \mathbf{k}\rangle$ inside the CuO_2 layer to free electron state $|\mathbf{K}\rangle$ outside. As the momentum of the photon \mathbf{q} is much smaller than that of the electrons inside the layer ($\lambda_{\text{ph}} \gg$ lattice spacing), the dipole approximation $\mathbf{q} \approx \mathbf{0}$ can be used

$$I(\mathbf{K}, \omega) \sim \sum_{n, \mathbf{k}} |\langle -\mathbf{K}_{\text{hole}} | \epsilon \cdot \mathbf{p} | n, \mathbf{k} \rangle|^2 \delta(\omega - E_n(\mathbf{k})), \quad (\text{F.2})$$

and $\mathbf{K}_{\text{hole}} = \mathbf{q}_{\text{ph}} - \mathbf{K} \approx -\mathbf{K}$. This matrix element $M = \langle -\mathbf{K}_{\text{hole}} | \epsilon \cdot \mathbf{p} | n, \mathbf{k} \rangle$ corresponds to the following integral

$$\begin{aligned} M &= -i\hbar \int d\mathbf{r} e^{i\mathbf{K} \cdot \mathbf{r}} \epsilon \cdot \nabla \sum_p c_p(n, \mathbf{k}) \frac{1}{\sqrt{N}} \sum_{\mathbf{R}_p} e^{i\mathbf{k} \cdot \mathbf{R}_p} \phi_p(\mathbf{r} - \mathbf{R}_p) \\ &= -i\hbar \sum_p c_p(n, \mathbf{k}) \frac{1}{\sqrt{N}} \sum_{\mathbf{R}_p} e^{i\mathbf{k} \cdot \mathbf{R}_p} \int d\mathbf{r} e^{i\mathbf{K} \cdot \mathbf{r}} \epsilon \cdot \nabla \phi_p(\mathbf{r} - \mathbf{R}_p) \end{aligned} \quad (\text{F.3})$$

in which $\phi_p(\mathbf{r} - \mathbf{R}_p)$ is the wavefunction of a $2p$ orbital located at \mathbf{R}_p , and $c_p(n, \mathbf{k})$ relates $|n, \mathbf{k}\rangle$ to the bare-hole eigenstates $|p, \mathbf{k}\rangle$

$$|n, \mathbf{k}\rangle = \sum_p c_p(n, \mathbf{k}) |p, \mathbf{k}\rangle + \dots, \quad (\text{F.4})$$

where ... includes contributions with at least one magnon. In Eq. (F.3), the lowest level of approximation is used where the terms describing the possibility for creation of magnons when the electron is removed are neglected.

The integral is written as

$$e^{i\mathbf{K}\cdot\mathbf{R}_p} \int d\boldsymbol{\rho} e^{i\mathbf{K}\cdot\boldsymbol{\rho}} \boldsymbol{\epsilon}\cdot\nabla\phi_p(\boldsymbol{\rho}) \quad (\text{F.5})$$

where $\boldsymbol{\rho} \equiv \mathbf{r} - \mathbf{R}_p$. Using this in Eq. (F.3) and doing the summation over \mathbf{R}_p we get

$$M = -i\hbar\sqrt{N} \sum_p c_p(n, \mathbf{k}) \sum_{\mathbf{G}} \delta_{\mathbf{k}+\mathbf{K}_{\parallel}, \mathbf{G}} e^{i\mathbf{G}\cdot\boldsymbol{\delta}_p} \int d\boldsymbol{\rho} e^{i\mathbf{K}\cdot\boldsymbol{\rho}} \boldsymbol{\epsilon}\cdot\nabla\phi_p(\boldsymbol{\rho}). \quad (\text{F.6})$$

Here, \mathbf{G} 's are the reciprocal lattice vectors of the magnetic sublattice \mathbf{R} , $e^{i\mathbf{G}\cdot\mathbf{R}} = 1$, and $\boldsymbol{\delta}_p$'s define the location of the four $2p$ orbitals inside the unit cell, $\mathbf{R}_p = \mathbf{R} + \boldsymbol{\delta}_p$. The integral is evaluated using $\phi_p(\boldsymbol{\rho}) \sim x_p e^{-\lambda\rho}$ where $x_p = x(y)$ if p is an $x(y)$ orbital, for example

$$\begin{aligned} m_x &\sim \int d\boldsymbol{\rho} e^{i\mathbf{K}\cdot\boldsymbol{\rho}} \boldsymbol{\epsilon}\cdot\nabla(xe^{-\lambda\rho}) \\ &= \epsilon_x \int d\boldsymbol{\rho} e^{i\mathbf{K}\cdot\boldsymbol{\rho}-\lambda\rho} - \lambda \int d\boldsymbol{\rho} e^{i\mathbf{K}\cdot\boldsymbol{\rho}-\lambda\rho} x\boldsymbol{\epsilon}\cdot\boldsymbol{\rho}/\rho. \end{aligned} \quad (\text{F.7})$$

The relevant limit here is when the wavelength of the outgoing electrons $1/K$ is much greater than the size of $2p$ orbitals, i.e. $\lambda \gg K$. m_x is dominated by the first integral in this limit and it is given as

$$m_x \approx \epsilon_x \int d\boldsymbol{\rho} e^{i\mathbf{K}\cdot\boldsymbol{\rho}-\lambda\rho} = \frac{8\pi\lambda\epsilon_x}{(\lambda^2 + K^2)^2} \simeq \frac{8\pi}{\lambda^3} \epsilon_x. \quad (\text{F.8})$$

ϵ_y and ϵ_z components are also given similarly. Hence,

$$M = -i\hbar\sqrt{N} \sum_p c_p(n, \mathbf{k}) \sum_{\mathbf{G}} \delta_{\mathbf{k}+\mathbf{K}_{\parallel}, \mathbf{G}} e^{i\mathbf{G}\cdot\boldsymbol{\delta}_p} \frac{8\pi}{\lambda^3} \boldsymbol{\epsilon}_p \quad (\text{F.9})$$

and

$$|M|^2 = \frac{64\pi^2\hbar^2 N}{\lambda^6} \sum_{\mathbf{G}} \delta_{\mathbf{k}+\mathbf{K}_{\parallel}, \mathbf{G}} \sum_{p, p'} c_p(n, \mathbf{k}) c_{p'}^*(n, \mathbf{k}) e^{i\mathbf{G}\cdot(\boldsymbol{\delta}_p - \boldsymbol{\delta}_{p'})} \epsilon_p \epsilon_{p'}. \quad (\text{F.10})$$

The intensity $I(\mathbf{K}, \omega)$ is then written as

$$I(\mathbf{K}, \omega) \sim \sum_{\mathbf{G}, \mathbf{k}} \delta_{\mathbf{k}+\mathbf{K}_{\parallel}, \mathbf{G}} \sum_{p, p'} e^{i\mathbf{G}\cdot(\boldsymbol{\delta}_p - \boldsymbol{\delta}_{p'})} \epsilon_p \epsilon_{p'} \frac{-1}{\pi} \text{Im} G_{p, p'}(\mathbf{k}, \omega) \quad (\text{F.11})$$

where we have used the following

$$\delta(\omega - E_n(\mathbf{k})) = -\frac{1}{\pi} \text{Im} \langle n, \mathbf{k} | \hat{G}(\omega) | n, \mathbf{k} \rangle \approx -\frac{1}{\pi} \text{Im} \sum_{p,p'} G_{p,p'}(\mathbf{k}, \omega)$$

in which only the first term of Eq. (F.4) is retained as before. Eq. (5.27) is finally recovered by averaging Eq. (F.11) with respect to the polarization of the incoming photon $\langle \epsilon_p \epsilon_{p'} \rangle = \langle \epsilon_p^2 \rangle \eta_{p,p'}$,

$$\bar{I}(\mathbf{K}, \omega) \sim \sum_{\mathbf{G}, \mathbf{k}} \delta_{\mathbf{k}+\mathbf{K}_{\parallel}, \mathbf{G}} \sum_{p,p'} e^{i\mathbf{G} \cdot (\delta_p - \delta_{p'})} \eta_{p,p'} A_{p,p'}(\mathbf{k}, \omega), \quad (\text{F.12})$$

where $\eta_{p,p'} = 1$ if p and p' are of the same type (both p_x or both p_y) and zero otherwise. The approximation $K \ll \lambda$ is valid for small K , but for larger

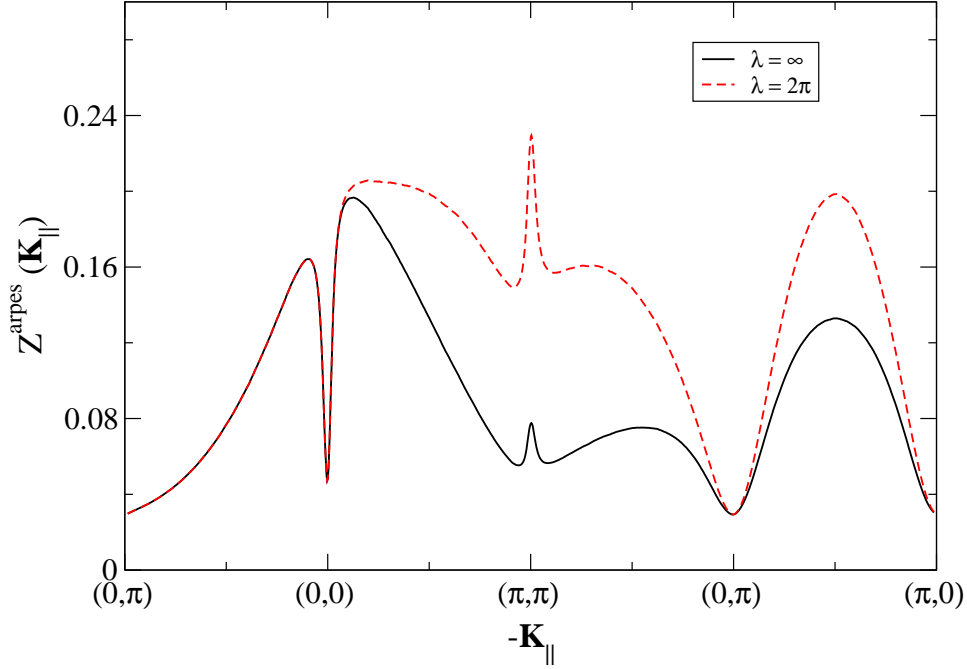


Figure F.1: The effect of finite K/λ (lowest order correction) on the ARPES quasiparticle weight of the five-band model. The difference between the quasiparticle dispersions is invisible on the same energy scale.

momenta one has to keep the second integral in Eq. (F.7). Including the leading order correction to m_α gives

$$m_\alpha \approx \frac{8\pi}{\lambda^3} \epsilon_\alpha + \frac{32\pi K_\alpha}{\lambda^5} (K_\beta \epsilon_\beta + K_\gamma \epsilon_\gamma). \quad (\text{F.13})$$

where β and γ are the other two indices. This modifies the averages as

$$\langle m_p m_{p'} \rangle \sim [\eta_{pp'} + \frac{8K_p K_{p'}}{\lambda^2} (1 - \eta_{pp'})] \langle \epsilon_p^2 \rangle.$$

This results in corrections that involves interference between $2p$ orbitals of different types and modifies the ARPES quasiparticle weight accordingly, Fig. F.

Appendix G

Solving for $G_{\alpha,\beta}(\mathbf{k}, \omega)$ in the five-band model

For $G_{\alpha,p_{a_x}}(\mathbf{k}, \omega)$, the second term in

$$G_{\alpha,p_{a_x}}(\mathbf{k}, \omega) = g_0(\omega)[\delta_{\alpha,p_{a_x}} + \langle \mathbf{k}, \alpha, \uparrow | \hat{G}(\omega) \mathcal{H}_1 | \mathbf{k}, p_{a_x}, \uparrow \rangle],$$

becomes as follows

$$\begin{aligned} \langle \mathbf{k}, \alpha, \uparrow | \hat{G}(\omega) \mathcal{H}_1 | \mathbf{k}, p_{a_x}, \uparrow \rangle &= t_s[-V_1^3 + V_1^1 - V_1^2] + \frac{J_{pd}}{2}V_1^0 + t_s[e^{i(k_x - k_y)/2} \\ &\times G_{\alpha,p_{c_y}}(\mathbf{k}, \omega) - e^{i(k_x + k_y)/2}G_{\alpha,p_{d_y}}(\mathbf{k}, \omega) \\ &- e^{ik_x}G_{\alpha,p_{b_x}}(\mathbf{k}, \omega)] + 2t_{pp}[\cos((k_x + k_y)/2) \\ &\times G_{\alpha,p_{d_y}}(\mathbf{k}, \omega) - \cos((k_x - k_y)/2)G_{\alpha,p_{c_y}}(\mathbf{k}, \omega)] \\ &- 2t'_{pp}\cos(k_x)G_{\alpha,p_{b_x}}(\mathbf{k}, \omega) - 2\tilde{t}_{pp}[\cos((k_x + k_y)/2) \\ &\times G_{\alpha,p_{d_x}}(\mathbf{k}, \omega) + \cos((k_x - k_y)/2)G_{\alpha,p_{c_x}}(\mathbf{k}, \omega)]. \end{aligned} \quad (\text{G.1})$$

Equation of motion for GFs where the hole starts from the rest of original $2p$ orbitals is

$$\begin{aligned} \langle \mathbf{k}, \alpha, \uparrow | \hat{G}(\omega) \mathcal{H}_1 | \mathbf{k}, p_{b_x}, \uparrow \rangle &= \{ \dots \} - 2\tilde{t}_{pp}[\cos((k_x + k_y)/2)G_{\alpha,p_{c_x}}(\mathbf{k}, \omega) \\ &+ \cos((k_x - k_y)/2)G_{\alpha,p_{d_x}}(\mathbf{k}, \omega)], \end{aligned} \quad (\text{G.2})$$

$$\begin{aligned} \langle \mathbf{k}, \alpha, \uparrow | \hat{G}(\omega) \mathcal{H}_1 | \mathbf{k}, p_{c_y}, \uparrow \rangle &= \{ \dots \} - 2\tilde{t}_{pp}[\cos((k_x + k_y)/2)G_{\alpha,p_{b_y}}(\mathbf{k}, \omega) \\ &- \cos((k_x - k_y)/2)G_{\alpha,p_{a_y}}(\mathbf{k}, \omega)], \end{aligned} \quad (\text{G.3})$$

$$\begin{aligned} \langle \mathbf{k}, \alpha, \uparrow | \hat{G}(\omega) \mathcal{H}_1 | \mathbf{k}, p_{d_y}, \uparrow \rangle &= \{ \dots \} - 2\tilde{t}_{pp}[\cos((k_x + k_y)/2)G_{\alpha,p_{a_y}}(\mathbf{k}, \omega) \\ &+ \cos((k_x - k_y)/2)G_{\alpha,p_{b_y}}(\mathbf{k}, \omega)], \end{aligned} \quad (\text{G.4})$$

where $\{ \dots \}$ refers to those terms that existed before introducing the new orbitals, as in Eq. (5.10). V_l^i (implicit within $\{ \dots \}$) are now one-magnon

Appendix G. Solving for $G_{\alpha,\beta}(\mathbf{k}, \omega)$ in the five-band model

GFs where the hole occupies one of the original $2p$ orbitals. In one-magnon approximation, their equation of motion links to various $G_{\alpha\beta}(\mathbf{k}, \omega)$, other one-magnon GFs of the same type V and also to a new class of one-magnon GFs, U , where the hole occupies one of the new orbitals in the presence of a magnon. For example,

$$\begin{aligned}
\frac{V_1^0}{g_1(\omega)} &= t_s[-e^{-i(k_x+k_y)/2}G_{\alpha,p_{dy}}(\mathbf{k}, \omega) + e^{i(k_y-k_x)/2}G_{\alpha,p_{cy}}(\mathbf{k}, \omega) \\
&\quad - e^{-ik_x}G_{\alpha,p_{bx}}(\mathbf{k}, \omega)] + \frac{J_{pd}}{2}[G_{\alpha,p_{ax}}(\mathbf{k}, \omega) - V_1^0] \\
&\quad + t_{pp}[V_3^1 + V_1^3 - V_1^1 - V_3^{11}] - t'_{pp}[V_3^0 + V_1^2] \\
&\quad - \tilde{t}_{pp}[U_3^1 + U_1^3 + U_1^1 + U_3^{11}]. \tag{G.5}
\end{aligned}$$

When the hole start from the new $2p$ orbitals, due to lack of hybridization with Cu, there is no \hat{T}_{swap} and \mathcal{H}_{pd} and the equations of motion are therefore simpler:

$$\begin{aligned}
\frac{G_{\alpha,p_{ay}}(\mathbf{k}, \omega)}{\tilde{g}_0(\omega)} - \delta_{\alpha,p_{ay}} &= 2t_{pp}[\cos((k_x + k_y)/2)G_{\alpha,p_{dx}}(\mathbf{k}, \omega) \\
&\quad - \cos((k_x - k_y)/2)G_{\alpha,p_{cx}}(\mathbf{k}, \omega)] \\
&\quad - 2\tilde{t}_{pp}[\cos((k_x + k_y)/2)G_{\alpha,p_{dy}}(\mathbf{k}, \omega) \\
&\quad + \cos((k_x - k_y)/2)G_{\alpha,p_{cy}}(\mathbf{k}, \omega)] \\
&\quad - 2t'_{pp}\cos(k_y)G_{\alpha,p_{by}}(\mathbf{k}, \omega), \tag{G.6}
\end{aligned}$$

and so on. Note that the doping hole does not inhibit the superexchange coupling between its neighbouring Cu in this case as it does not occupy the $2p$ orbital hybridizing with them, hence $\tilde{g}_0(\omega) = 1/(\omega + i\eta)$. Similarly, we have

$$\begin{aligned}
\frac{G_{\alpha,p_{by}}(\mathbf{k}, \omega)}{\tilde{g}_0(\omega)} - \delta_{\alpha,p_{by}} &= 2t_{pp}[\cos((k_x + k_y)/2)G_{\alpha,p_{cx}}(\mathbf{k}, \omega) \\
&\quad - \cos((k_x - k_y)/2)G_{\alpha,p_{dx}}(\mathbf{k}, \omega)] \\
&\quad - 2\tilde{t}_{pp}[\cos((k_x + k_y)/2)G_{\alpha,p_{cy}}(\mathbf{k}, \omega) \\
&\quad + \cos((k_x - k_y)/2)G_{\alpha,p_{dy}}(\mathbf{k}, \omega)] \\
&\quad - 2t'_{pp}\cos(k_y)G_{\alpha,p_{ay}}(\mathbf{k}, \omega), \tag{G.7}
\end{aligned}$$

Appendix G. Solving for $G_{\alpha,\beta}(\mathbf{k}, \omega)$ in the five-band model

$$\begin{aligned}
\frac{G_{\alpha,p_{c_x}}(\mathbf{k}, \omega)}{\tilde{g}_0(\omega)} - \delta_{\alpha,p_{c_x}} &= 2t_{pp}[\cos((k_x + k_y)/2)G_{\alpha,p_{b_y}}(\mathbf{k}, \omega) \\
&\quad - \cos((k_x - k_y)/2)G_{\alpha,p_{a_y}}(\mathbf{k}, \omega)] \\
&\quad - 2\tilde{t}_{pp}[\cos((k_x + k_y)/2)G_{\alpha,p_{b_x}}(\mathbf{k}, \omega) \\
&\quad + \cos((k_x - k_y)/2)G_{\alpha,p_{a_x}}(\mathbf{k}, \omega)] \\
&\quad - 2\tilde{t}'_{pp} \cos(k_x)G_{\alpha,p_{d_x}}(\mathbf{k}, \omega), \tag{G.8}
\end{aligned}$$

$$\begin{aligned}
\frac{G_{\alpha,p_{d_x}}(\mathbf{k}, \omega)}{\tilde{g}_0(\omega)} - \delta_{\alpha,p_{d_x}} &= 2t_{pp}[\cos((k_x + k_y)/2)G_{\alpha,p_{a_y}}(\mathbf{k}, \omega) \\
&\quad - \cos((k_x - k_y)/2)G_{\alpha,p_{b_y}}(\mathbf{k}, \omega)] \\
&\quad - 2\tilde{t}_{pp}[\cos((k_x + k_y)/2)G_{\alpha,p_{a_x}}(\mathbf{k}, \omega) \\
&\quad + \cos((k_x - k_y)/2)G_{\alpha,p_{b_x}}(\mathbf{k}, \omega)] \\
&\quad - 2\tilde{t}'_{pp} \cos(k_x)G_{\alpha,p_{c_x}}(\mathbf{k}, \omega). \tag{G.9}
\end{aligned}$$

Equations of motion for U_l^i link them to various other one-magnon GFs only,

$$\begin{aligned}
\frac{U_1^0}{\tilde{g}_1(\omega)} &= t_{pp}(U_1^3 + U_3^1 - U_1^1 - U_3^{11}) - \tilde{t}_{pp}(V_1^3 + V_3^1 \\
&\quad + V_1^1 + V_3^{11}) - \tilde{t}'_{pp}(U_3^{10} + U_3^2), \tag{G.10}
\end{aligned}$$

$$\begin{aligned}
\frac{U_1^1}{\tilde{g}_1(\omega)} &= t_{pp}(U_1^2 + U_3^2 - U_1^0 - U_3^4) - \tilde{t}_{pp}(V_1^2 + V_3^2 \\
&\quad + V_1^0 + V_3^4) - \tilde{t}'_{pp}(U_3^1 + U_3^5), \tag{G.11}
\end{aligned}$$

$$\begin{aligned}
\frac{U_1^2}{\tilde{g}_1(\omega)} &= t_{pp}(U_1^1 + U_3^7 - U_1^3 - U_3^5) - \tilde{t}_{pp}(V_1^1 + V_3^7 \\
&\quad + V_1^3 + V_3^5) - \tilde{t}'_{pp}(U_3^4 + U_3^8). \tag{G.12}
\end{aligned}$$

$$\begin{aligned}
\frac{U_1^3}{\tilde{g}_1(\omega)} &= t_{pp}(U_1^0 + U_3^8 - U_1^2 - U_3^{10}) - \tilde{t}_{pp}(V_1^0 + V_3^8 \\
&\quad + V_1^2 + V_3^{10}) - \tilde{t}'_{pp}(U_3^7 + U_3^{11}), \tag{G.13}
\end{aligned}$$

where $\tilde{g}_1(\omega) = 1/(\omega - 2J_{dd} + i\eta)$ since all four AFM bonds are turned ferromagnetic. The equations of motion for one-magnon GFs at $M \geq 3$ are

similar to those in the three-band model, Eq. (5.19), with equations for V and U coupled together:

$$\begin{aligned}\lambda_l \mathbf{V}_l &= \xi_l \mathbf{V}_{l-2} + \zeta_l \mathbf{V}_{l+2} + \xi'_l \mathbf{U}_{l-2} + \zeta'_l \mathbf{U}_{l+2} - \lambda'_l \mathbf{U}_l, \\ \tilde{\lambda}_l \mathbf{U}_l &= \tilde{\xi}_l \mathbf{U}_{l-2} + \tilde{\zeta}_l \mathbf{U}_{l+2} + \xi''_l \mathbf{V}_{l-2} + \zeta''_l \mathbf{V}_{l+2} - \lambda''_l \mathbf{V}_l.\end{aligned}\quad (\text{G.14})$$

This can be expressed as a single-index recursive equation for $\mathbf{Z}_l = \begin{bmatrix} \mathbf{V}_l \\ \mathbf{U}_l \end{bmatrix}$:

$$\Lambda_l \mathbf{Z}_l = \Omega_l \mathbf{Z}_{l-2} + \Gamma_l \mathbf{Z}_{l+2},$$

where $\Lambda_l = \begin{pmatrix} \lambda_l & \lambda'_l \\ \tilde{\lambda}_l & \lambda''_l \end{pmatrix}$ and so on. This results in a continued-fraction solution relating \mathbf{V}_3 and \mathbf{U}_3 to both \mathbf{V}_1 and \mathbf{U}_1 , similar to Eq. (5.20). The rest of the calculation proceeds as in Sec. 5.3.1, solving the remaining linear equations to yield all 64 sublattice Green's function $G_{\alpha\beta}(\mathbf{k},\omega)$.